The Random Material Point Method for assessment of residual dyke resistance
Investigating the influence of soil heterogeneity on slope failure processes

Remmerswaal, G.

DOI
10.4233/uuid:5f32c08d-bc3d-452d-9e38-91d93a3e3499

Publication date
2023

Document Version
Final published version

Citation (APA)
Remmerswaal, G. (2023). *The Random Material Point Method for assessment of residual dyke resistance: Investigating the influence of soil heterogeneity on slope failure processes*. [Dissertation (TU Delft), Delft University of Technology]. https://doi.org/10.4233/uuid:5f32c08d-bc3d-452d-9e38-91d93a3e3499

THE RANDOM MATERIAL POINT METHOD FOR ASSESSMENT OF RESIDUAL DYKE RESISTANCE

Guido Remmerswaal

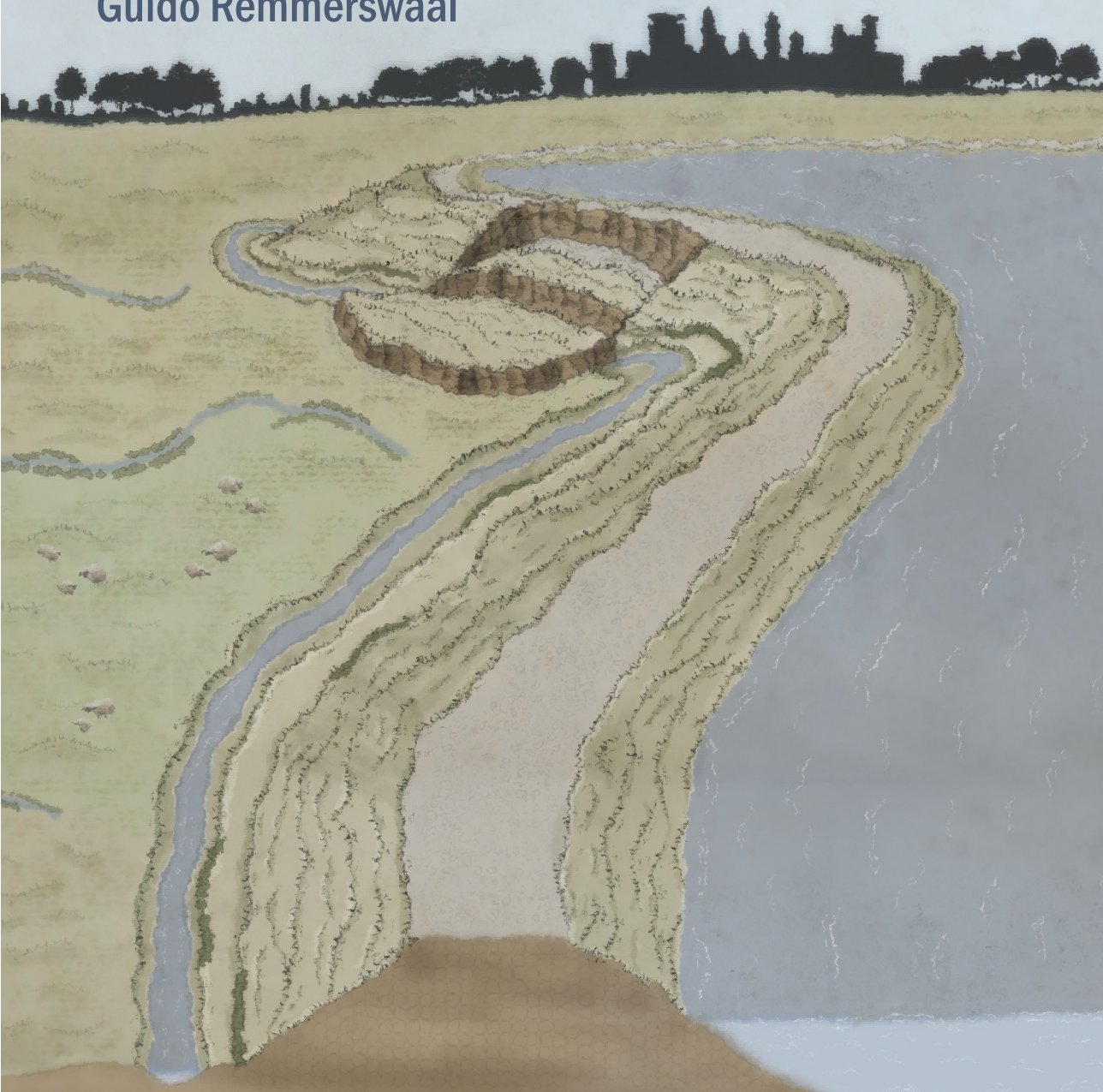

INVESTIGATING THE INFLUENCE OF SOIL HETEROGENEITY ON SLOPE FAILURE PROCESSES

THE RANDOM MATERIAL POINT METHOD FOR ASSESSMENT OF RESIDUAL DYKE RESISTANCE

INVESTIGATING THE INFLUENCE OF SOIL HETEROGENEITY ON SLOPE FAILURE PROCESSES

Proefschrift

ter verkrijging van de graad van doctor
aan de Technische Universiteit Delft,
op gezag van de Rector Magnificus prof. dr. ir. T.H.J.J. van de Hagen,
voorzitter van het College voor Promoties,
in het openbaar te verdedigen op maandag 18 september 2023 om 15:00 uur

door

Guido REMMERSWAAL

Master of Science in Civil Engineering, Technische Universiteit Delft, Nederland
geboren te Pijnacker, Nederland

Dit proefschrift is goedgekeurd door de

promotor: prof. dr. M.A. Hicks
promotor: prof. dr. P.J. Vardon

Samenstelling promotiecommissie:

Rector Magnificus,	voorzitter
Prof. dr. M.A. Hicks,	Technische Universiteit Delft
Prof. dr. P.J. Vardon,	Technische Universiteit Delft
Onafhankelijke leden:	
Prof. dr. ir. C. Vuik,	Technische Universiteit Delft
Prof. dr. G.A. Fenton,	Dalhousie University, Canada
Prof. dr. ir. L.J. Sluys,	Technische Universiteit Delft
Prof. dr. ir. S.N. Jonkman,	Technische Universiteit Delft
Dr. W. Solowski,	Aalto University, Finland

Keywords: Random Material Point Method (MPM), residual dyke resistance, slope failure, soil heterogeneity, random fields, probability of flooding
Printed by: Proefschriftspecialist
Front & Back: G. Remmerswaal

ISBN 978-94-6384-469-7

An electronic version of this dissertation is available at
http://repository.tudelft.nl/.

When humankind puts its mind to it and doesn't let its judgement be clouded by what people want to believe, humans can be pretty good at probability. If we want to . . .

Matt Parker

CONTENTS

SUMMARY

Flood protection infrastructure requires constant investments to cover the increasing flood risk. However, due to over-conservatism in (dyke) safety assessments, poorly targeted investments can be made. Over-conservatism can be avoided by understanding the entire failure process, from the initiation of failure until flooding. Dyke slope instability is one of the main initiation mechanisms evaluated during a safety assessment. Following an initial instability, a slope failure occurs, where large deformations may occur as the failure mass slides along the failure surface. A large initial failure mechanism may immediately trigger flooding, but in most cases secondary mechanisms, such as new slope failures, are required to flood the hinterland. The dyke may have enough resistance to prevent secondary mechanisms and thereby prevent flooding. Therefore, dyke assessments can be optimised by assessing the potential for secondary failures.

The standard methods for dyke slope stability assessment cannot model large deformations. This thesis therefore develops and applies the Material Point Method (MPM), a large deformation variant of the Finite Element Method, to investigate the residual (remaining) resistance of a dyke against flooding after an initial slope instability. The residual dyke resistance has been assessed within a risk-based framework using the Random MPM (RMPM), which accounts for the effects of soil heterogeneity on the failure process by combining random fields with MPM. From the realisations of an RMPM analysis, both the probability of initial failure as well as the probability of flooding may be determined. Moreover, with RMPM, the likelihood of failure processes can be evaluated such that the process between initial failure and flooding can be understood.

To model the external water level in the RMPM analysis, the application of boundary conditions in MPM has first been investigated. The thesis shows that the boundary conditions should systematically match the MPM discretisation. Improvements of MPM, such as the Generalized Interpolation Material Point Method (GIMP), often change the discretisation. Therefore, the accurate application of a boundary condition can therefore depend on the version of MPM being used. Consistent boundary conditions are described in this work for MPM and GIMP. For standard MPM, a consistent boundary condition is proposed for simple 1D problems. However, it is shown that this solution is not generally applicable for dyke slope failures or other higher dimensional problems. For GIMP, two generally applicable algorithms for (almost) consistent boundary conditions are proposed: one algorithm constructs the exact material boundary, while the other merges the support domains of all material points. The algorithms are shown to outperform other boundary condition methods presented in literature.

The residual (dyke) resistance has been investigated by modelling both a 2D dyke failure and 3D slope instability using RMPM. It is shown that secondary failures (required to trigger flooding) often do not occur or may not be large enough to trigger flooding. Therefore, the probability of flooding can be significantly lower than the probability of an initial failure due to residual dyke resistance. In the best case scenario for the prob-

lem analysed, a reduction of the probability of flooding compared to the probability of initial failure of more than 90% has been observed, while in the worst case only a 10% reduction was found. The reduction was high (90%) for a material without layering of the spatial variability of the strength properties and decreased when the spatial variability was more layered. However, note that, to reduce computational costs, the probability of initial failure was unrealistically high in these examples, i.e. the dyke was relatively weak. In stronger slopes, secondary failures are less likely and more residual dyke resistance is therefore expected. Additionally, secondary slope failures are less likely in 3D simulations compared to 2D simulations, generally due to the additional resistance of the sides of the failure surfaces (the so-called 3D-effect). A 2D simulation can therefore be seen as a conservative estimate of the residual dyke resistance. In 3D, the failure process more often spreads sideways rather than backwards. This is also beneficial for dyke slope stability assessments, where backward failures are required to trigger flooding.

The degree of anisotropy of the soil heterogeneity changes the expected failure process. For smaller horizontal scales of fluctuation, i.e. less layering of the soil, secondary failures are less likely to occur, since the initial and secondary failures are mostly uncorrelated. Additionally, in the 3D simulation, smaller horizontal scales of fluctuation triggered small failure blocks, again likely to reduce the risk of flooding. For larger horizontal scales of fluctuation, initial failure in a weaker layer can more easily trigger secondary failures through the same layer, thereby decreasing residual dyke resistance. A depth trend, i.e. a linear increase with depth, in the mean resistance of the material, typical due to compaction processes, also impacts the failure process. For a material without a depth trend, progressive failure occurs along approximately circular failure surfaces, whereas for a material with a depth trend, a steady flow like behaviour along a gentle 'straight' slope occurs. Moreover, retrogressive failure can flow in any direction for a material with a depth trend while avoiding local strong zones.

This thesis highlights that RMPM can provide estimates of the residual dyke resistance, thereby more accurately estimating the probability of flooding due to dyke slope instability in many situations. This leads to more targeted and cost effective dyke reinforcements. RMPM also provides insight into the size and shape of the initial and subsequent failures. RMPM can therefore be used in future research to develop guidelines for practice to approximate the probability of flooding, for example based on the probability and the shape of the initial failure computed with a small deformation model.

SAMENVATTING

Maatregelen tegen overstromingen vereisen constante investeringen om het toenemende overstromingsrisico te beheersen. Door te conservatieve veiligheidsbeoordelingen van dijken worden investeringen soms niet optimaal ingezet. Te conservatieve beoordelingen kunnen vermeden worden wanneer er beter begrip is van het gehele faalproces van een dijk, van de start van het faalproces tot aan de overstroming. Een van de belangrijkste oorzaken voor het falen van een dijk is een dijkafschuiving, welke geëvalueerd wordt tijdens een veiligheidsbeoordeling. Een dijkafschuiving volgt nadat de belasting op de dijk een instabiele situatie veroorzaakt. Na de instabiliteit kunnen er grote deformaties optreden, waarbij de grondmoot over een faalvlak glijdt. Wanneer er een grote dijkafschuiving plaatsvindt, kan dit meteen tot een overstroming leiden. In de meeste gevallen leiden echter pas secundaire faalmechanismen, zoals nieuwe afschuivingen, tot overstroming van het achterland. In sommige gevallen heeft een dijk dus genoeg reststerkte om secundaire faalmechanismen en daarmee overstromingen te voorkomen. Daarom kunnen veiligheidsbeoordelingen van dijken geoptimaliseerd worden door de kans op secundaire faalmechanismen te evalueren.

De meest gebruikte methoden voor beoordelingen van dijkafschuivingen kunnen grote deformaties niet modelleren. In dit proefschrift wordt de Materiaal Punten Methode (MPM), een variant op de Eindige Elementen Methode (EEM) waarmee grote deformaties gemodelleerd kunnen worden, ontwikkeld en toegepast om de reststerkte van een dijk na de primaire dijkafschuiving te bepalen. De reststerkte wordt onderzocht binnen een op risico gebaseerde methodiek door gebruik te maken van Random MPM (RMPM). RMPM is een methode die rekening houdt met het effect van de variabiliteit van de grond, die met random fields beschreven wordt, op het faalproces. Met de realisaties van een RMPM analyse kunnen zowel de kans op een primaire dijkafschuiving als de kans op overstroming te bepaald worden. Bovendien kan het proces tussen de primaire dijkafschuiving en overstroming begrepen worden.

In dit proefschrift is de toepassing van randvoorwaarden in MPM onderzocht om daarmee externe waterniveaus te modelleren. Het proefschrift laat zien dat de randvoorwaarden systematisch overeen moeten komen met de discretisatie die gebruikt wordt in MPM. Om de nauwkeurigheid en stabiliteit van standaard MPM te verbeteren is in verschillende nieuwe versies van MPM, zoals de Gegeneraliseerde Interpolatie Materiaal Punten Methode (GIMP), de discretisatie gewijzigd. Daardoor kan de juiste toepassing van randvoorwaarden afhankelijk zijn van de versie van MPM die gebruikt wordt. Consistente randvoorwaarden worden beschreven in dit proefschrift voor MPM en GIMP. Voor standaard MPM wordt een consistente randvoorwaarde voorgesteld voor eenvoudige ééndimensionale problemen. Echter blijkt deze methode niet generiek toepasbaar te zijn op dijkafschuivingen of andere 2D en 3D problemen. Voor GIMP worden twee breed toepasbare algoritmes voor (bijna) consistente randvoorwaarden voorgesteld: één algoritme bepaalt de exacte rand van het materiaal, terwijl de andere methode de do-

meinen rondom alle materiaalpunten samenvoegt. De algoritmes werken beter voor het toepassen van randvoorwaarden dan de methoden die beschreven zijn in literatuur.

De reststerkte van een dijk is met RMPM onderzocht door het modelleren van zowel een 2D dijkafschuiving en een 3D afschuiving. De modellen laten zien dat een secundair faalmechanisme (nodig om een overstroming te veroorzaken) vaak niet optreedt of wel optreedt, maar niet groot genoeg is om een overstroming te veroorzaken. De kans op een overstroming kan dus significant kleiner zijn dan de kans op een primaire dijkafschuiving door de reststerkte van de dijk. In het beste geval vond een vermindering van meer dan 90% plaats, terwijl in het slechtste geval slechts een reductie van 10% plaats vond. De afname was groot (90%) voor materiaal zonder gelaagdheid van de variabiliteit van de sterkte eigenschappen en neemt af wanneer de variabiliteit meer gelaagd is. Belangrijk hierbij te noemen is dat, om de tijdsduur van de berekening te verkorten, de kans op een primaire dijkafschuiving onrealistisch hoog was in deze voorbeelden. De dijk was hierdoor relatief zwak was. Bij sterkere dijken zijn secundaire faalprocessen minder waarschijnlijk en is daarom een hogere reststerkte te verwachten. Bovendien is het optreden van secundaire faalprocessen minder waarschijnlijk in 3D simulaties vergeleken met 2D simulaties, vanwege de extra sterkte aan de randen van de 3-dimensionale glijvlakken (deze hogere sterkte wordt het “3D-effect” genoemd). Een 2D simulatie kan daarom gezien worden als een conservatieve schatting van de reststerkte van een dijk. In 3D, verspreidt het faalproces zich vaker zijwaarts dan achterwaarts. Dit is ook voordelig voor veiligheidsbeoordelingen van dijken, omdat achterwaartse faalprocessen nodig zijn om een overstroming te veroorzaken.

De mate van anisotropie van de heterogeniteit van de grond veranderd het verwachte faalproces. Voor kleinere horizontale fluctuatie afstanden, dat wil zeggen minder gelaagdheid van de bodem, is het minder waarschijnlijk dat secundaire afschuivingen optreden, aangezien de primaire en secundaire afschuivingen meestal niet gecorreleerd zijn. Bovendien veroorzaken kleinere horizontale fluctuatie afstanden in de 3D-simulatie kleine afschuivingen, wat waarschijnlijk ook het risico op overstroming vermindert. Voor grotere horizontale fluctuatie afstanden kan de primaire afschuiving in een zwakkere bodemlaag gemakkelijker een secundaire afschuiving tot gevolg hebben, waardoor de reststerkte van de dijk afneemt. Een dieptetrend, dat wil zeggen een lineaire toename in de gemiddelde sterkte van het materiaal met de diepte (het gevolg van verdichtingsprocessen), heeft ook invloed op het faalproces. Voor een materiaal zonder dieptetrend treedt het faalproces op langs circulaire faaloppervlakken, terwijl er voor een materiaal met dieptetrend, een continue stroming is langs een matige helling. Bovendien kan retrogressief falen zorgen voor een stroming in elke richting voor een materiaal met een dieptetrend, waarbij plekken met een hoge sterkte worden ontweken.

Dit proefschrift laat zien dat RMPM een schatting kan geven van de reststerkte van een dijk, waardoor de kans op een overstroming door een dijkafschuiving in veel situaties nauwkeuriger kan worden ingeschat. Dit leidt tot meer gerichte en kosteneffectieve dijkverzwaringen. RMPM geeft ook inzicht in de grootte en vorm van de primaire en daarop volgende dijkafschuivingen. RMPM kan daarom in toekomstig onderzoek worden gebruikt om richtlijnen voor de praktijk te ontwikkelen om de overstromingskans te bepalen, bijvoorbeeld op basis van de kans en de vorm van de primaire dijkafschuiving, berekend met een model voor kleine deformaties.

ACKNOWLEDGEMENTS

Only after adding the cover to the digital document, I realized what I achieved over the last 6 years: creating a booklet by digging into dyke failure processes deeper than I could have imagined. I started this research project when the perfect research subject, a combination between my passion for dykes and MPM, presented itself. During the project, I got involved with the numerical details of MPM, the probabilistics behind dyke safety assessment, large scale parallel computing, and a near infinite supply of numerical output data. All experiences which I wouldn't want to have missed. The outcome is the start of a path to understanding (dyke) slope failure processes, and highlights the effectiveness of (R)MPM. I hope that my research will lead to more effective investments into world-wide flood protection systems, and can assist in preparing for the upcoming battles against flood risk. A big portion of the last six years were spend on my own staring at a screen. However, the book in front of you only came to fruition by the contributions of many. Some of these contributions I would like to address with a story describing the last 6 years.

The 6 years could almost be divided into a three act structure. The first two years flew by working together with Phil and Leon on improving implicit MPM, while setting up the first RMPM calculations on the parallel computer. Phil, you guided me when we were digging into the numerical details of MPM, always being able to provide new insight when Leon and I ran into a dead-end. Leon, I will never forget our discussions, our combined frustration with MPM, and the relaxing breaks in between. I am also thankful for everyone I could meet at conferences during this period, the many discussions there helped me shape my project. Being part of the All-Risk programme, which was funded by NWO, allowed me to be in contact with private and public partners, as well as the large research group with whom we visited dykes throughout the country. Matthijs and Bas, thank you both for organizing the programme and keeping the connections alive, while allowing me to pursue my own research goals.

During the third and fourth year, the 3D simulations and boundary conditions did not want to work properly, and discussions were at a low point due to corona. Mike, you helped me to keep pushing on in this period and provided the structure I was missing. You could spot irregularities in simulations in seconds, and you have an insight into soil heterogeneity I have not seen anywhere else. After these years, I am still impressed with the detailed comments you provide. I will never forgot the checkmarks behind each sentence, and started to enjoy seeing more and more of them as time progressed. During these years, I used the Spider data processing system by SurfSara extensively. The system was vital in finishing the PhD, the simulations would have taken years to complete otherwise, and the system worked flawlessly. Natalie and Raymond, thank you for helping me set up the calculations on the Spider system effectively.

In the fifth year starting a new job at Deltares, while trying to finish the PhD, was difficult. However, my colleagues at Deltares and the freedom to visit the office again,

allowed the joyful moments to come back in my working life. I am very thankful for the support of Deltares (and colleagues) for finishing the thesis. Specifically, I would like to thank John, Britt, Dirk, Remco, Kevin, Piet, Marien, Rob, Anderson, Cihan, Ruben and Negar. You let me feel at home in a new company, even when I was a bit grumpy at times. Mario, I wanted to thank you personally for introducing me back into MPM, and making that come back much more enjoyable then I would have expected. I am happy that I will be able to come back to work at Deltares, without having the thought of finishing a PhD at the back of my mind.

Finally, I would like to thank family and friends, which have kept me going during these 6 years. Marlon, Joost, Dennis, Daan en Ricardo, bedankt voor alle afleiding waarvoor jullie hebben gezorgd over de jaren heen. Ik kijk uit naar de volgende vakantie en whiskey avond (waarbij ik niet eerder afhaak omdat er de volgende dag nog gewerkt moet worden). Vera, Joost en Mark, ik heb met veel plezier met jullie samen gewerkt aan verschillende projecten, en jullie hebben er mede voor gezorgd dat ik dit traject heb weten af te ronden.

Lia, Dick en Stefan, ik ben dankbaar dat ik altijd bij jullie langs kon komen. Ik zal het samen werken in Huisje 17 nooit vergeten. Rianne, Victor, Piet en Judith, ik genoot van de momenten met jullie, omdat ik alles dan even achter me kon laten. Ook als doctor blijf ik gewoon jullie broer(tje). Papa, mama, jullie opvoeding helpen me nog steeds om met beide benen op de grond te blijven staan. Jullie stonden aan de basis van dit werk, en waren er voor me wanneer dat nodig was. Lisette, bedankt dat je er altijd voor me was. Als ik geïrriteerd of verdrietig ben weet je me altijd weer op te vrolijken. Ik had met niemand anders op een studentenkamer aan een promotie kunnen werken zonder gek te worden. Ik ben benieuwd wat ons volgende project wordt.

Guido Remmerswaal
Den Hoorn, August 2023

LIST OF SYMBOLS

Abbreviations

1D	1-dimensional
2D	2-dimensional
3D	3-dimensional
BC	Boundary condition
BSMPM	B-Spline Material Point Method
CPDI	Convected Particle Domain Interpolation method
CPDI2	Extended CPDI
cpGIMP	GIMP with normal deformation of support domains
CPT	Cone penetration test
DDMP	Dual Domain Material Point Method
DM	MPM with double mapping technique
DM-G	GIMP with double mapping technique
FE	Finite element
FEM	Finite Element Method
FLIP	FLuid Implicit Particle method
FORM	First Order Reliability Method
FoS	Factor of safety
GIMP	Generalized Interpolation Material Point method
IBM	Implicit Boundary Method
ILH	International Levee Handbook
KMCM	K-means cluster method
LEM	Limit Equilibrium Method
MM	Meshless method
MP	Material point
MPM	Material Point Method
PF	Proximity Field
PFM	Proximity Field Method
PIC	Particle-In-Cell method
RFEM	Random Finite Element Method
RMPM	Random Material Point Method
SBM	Shifted Boundary Method
uGIMP	standard GIMP
ULS	Ultimate limit state

Latin symbols

$\boldsymbol{a}$	Acceleration
A_i^1	Primary failure mechanism
a_j	Horizontal size of kernel function
$\boldsymbol{b}$	Body forces
$\mathbf{B}$	Shape function derivative matrix
b_j	Vertical size of kernel function
c	Undrained shear strength
$\mathrm{C}(F)$	Consequence of failure
c_i	Initial undrained shear strength
C_j	Kernel function constant
COV	Coefficient of variation
c_r	Residual undrained shear strength
$\mathbf{D}$	Stress-strain matrix
D	Geometric uncertainty
E	Young's modulus
E_{F_x}	Horizontal force difference
E_{F_y}	Vertical force difference
ele	FE element
emp	Number of MPs in an element
$\boldsymbol{F}_{\text{body}}$	Nodal body forces
$\boldsymbol{F}^c$	Point loads
$\boldsymbol{F}_{\text{ext}}$	Nodal external forces
$\boldsymbol{F}_{\text{int}}$	Nodal internal forces
$\boldsymbol{F}_{\text{kin}}$	Nodal kinetic forces
$\boldsymbol{F}_{\text{point}}$	Nodal point loads
$\boldsymbol{F}_{\text{traction}}$	Nodal traction forces
$\boldsymbol{F}_p$	Point load of MP p
$\boldsymbol{F}_{\text{MP}}$	Nodal loads method 1
$\boldsymbol{F}_{\text{Nodes}}$	Nodal loads method 2
$\boldsymbol{F}_{\text{Surface}}$	Nodal loads method 3
$\boldsymbol{F}_{\text{Volume}}$	Nodal loads method 4 (MPM)
$\boldsymbol{F}_{\text{GIMP}}$	Nodal loads method 4 (GIMP)
$f(h)$	Probability density function of h
F_i	Failure category
F_j	Flooding after instability S_j
$\boldsymbol{g}$	Gravity vector
H	Dyke height
h	Water level
H_i	Initial dyke height
H_{min}	Minimum gap height
H_r	Residual dyke height
H_s	Softening modulus
H_{total}	Total height of segments
I	Combined invisibility number

I^*	Combined invisibility number without gaps
i	Node
j	Integration point
$\mathbf{J}$	Jacobian matrix
J	Invisibility number for rectangles
j_b	Boundary integration point
$\mathbf{K}$	Stiffness matrix
$\mathbf{K}_{\text{ele}}$	Element stiffness matrix
$\mathbf{K}^*$	Modified stiffness matrix
K	Invisibility number for extensions
k	Depth trend of mean undrained shear strength
k	Point in space
$K_{i,j}$	Kernel function
L	3D Slope length
L	Loads triggering failure
lp	Half of the support domain size
lp_x	Half of the support domain size in x-direction
lp_y	Half of the support domain size in y-direction
$\mathbf{M}$	Mass matrix
$\mathbf{M}_{\text{ele}}$	Element mass matrix
M	Model uncertainty
m	Mass
$\mathbf{N}$	Shape function matrix
N_i	FEM shape function
∇N_i	FEM shape function gradient
N	Total number of realisations
n_c	Number of failure categories
nel	Number of elements
$N_F(t)$	Number of realisations with flooding before t
nip	Number of integration points in an element
$nipb$	Number of boundary integration points in an element
nmp	Number of MPs
N_{MPs}	Total number of material points
nn	Number of nodes
$N_{S_1}(t)$	Number of realisations with initial failure before t
p	Material point
$\mathrm{P}(F)$	Probability of failure
$\mathrm{P}(F\|S_1)$	Metric for residual dyke resistance
$\mathrm{P}(S_1)$	Probability of initial failure
$\mathrm{P_s}$	Maximum allowable probability of flooding
$\mathrm{P}(X\|Y)$	Probability of event X given event Y
$\boldsymbol{q}$	Traction
q	Traction value
Q	Material uncertainty
R	Resistance against failure

Risk(F)	Risk of failure
S_0	Intact dyke
S_1	Primary instability
S_{ip}	GIMP shape function
∇S_{ip}	GIMP shape function gradient
S	Macro-instability
S^c	Critical failure process
S_c	Sensitivity
S_k^c	Critical failure mechanism
$\mathbf{S}_j$	Shape matrix
S_j	Instability j
t	Time
Δt	Timestep size
t_F	Time of flooding
t_{max}	Maximum simulation time
t_{S_1}	Time of initial failure
$\bar{\boldsymbol{u}}$	Virtual displacement
$\Delta \boldsymbol{u}$	Nodal incremental displacements
$\delta \boldsymbol{u}$	Nodal displacements in a iteration step
$\Delta \boldsymbol{u}^*$	Nodal incremental displacements after velocity remapping
$\boldsymbol{u}^d$	Prescribed displacements
$\boldsymbol{u}_{i,j}$	Local distance
$u_{stable,max}$	Displacement threshold to activate KMCM
V	Volume
$\boldsymbol{v}$	Velocity
V_{ele}	Element volume
W	Dyke width at water level
W_c	Dyke crest width
W_i	Initial dyke width at water level
W_j	Gauss integration weight of point j
W_{min}	Minimum gap width
W_r	Residual dyke width at water level
W_{S_1}	Dyke width after initial failure
$\boldsymbol{x}$	global coordinates
x	x-coordinate
Δx	Mesh size in x-direction
x_{offset}	Distance of mesh boundary from surface Γ
y	y-coordinate
Δy	Mesh size in y-direction
z	z-coordinate
Z	Limit state function
Z_i	Limit state function for F_i

Greek symbols

β	Newmark time integration scheme constant
Γ	Surface area
γ	Newmark time integration scheme constant
Γ_d	Fixed surface area
Γ_{ele}	Surface area of element ele
Γ_m	Surface area of active elements
Γ_p	Surface area of MP p
Γ_τ	Loaded surface area
Γ_V	Surface area proportional to volume in m
γ_w	Unit weight
$\bar{\boldsymbol{\epsilon}}$	Virtual strain
$\bar{\epsilon}_p$	Plastic deviatoric shear strain invariant
$\bar{\epsilon}_{pr}$	$\bar{\epsilon}_p$ at onset of residual strength
θ	Surface angle
θ_h	Horizontal scale of fluctuation
θ_v	Vertical scale of fluctuation
μ	Mean
μ_{ci}	Mean initial undrained shear strength
μ_{cr}	Mean residual undrained shear strength
μ_L	Mean of the loads triggering failure
μ_R	Mean of the resistance against failure
ν	Poisson's ratio
ρ	Density
$\boldsymbol{\sigma}$	Cauchy stress
σ	Standard deviation
σ_{ci}	Standard deviation initial undrained shear strength
σ_{cr}	Standard deviation residual undrained shear strength
$\boldsymbol{\tau}$	Surface traction
ω_i	Portion of P_s reserved for $P(F_i)$

1

INTRODUCTION

With standard small deformation methods used in dyke flood risk assessment, it is difficult to assess the entire failure process. These assessment methods focus on the start of failure, and often ignore the resistance in the remainder of the process. Therefore, this thesis further develops the Material Point Method (MPM), a large deformation variant of the Finite Element Method (FEM), to investigate the entire failure process. A risk-based framework for secondary dyke failure mechanisms is presented, which is used to assess the residual resistance of a dyke against flooding after an initial slope failure. The framework includes the effect of soil heterogeneity, which is modelled by combining random fields with MPM. This chapter presents the background to dyke assessments, before introducing the numerical tools used in the thesis and discussing the thesis goals.

1

1.1. BACKGROUND

Floods pose an ever-increasing risk to many coastal or riverine villages and cities. Over 40% of the natural disasters during 1995-2014, see Figure 1.1, can be classified as floods, and these events affected 2.3 billion people in total (CRED and UNISDR, 2015). The number of floods increased in the decades from 1995-2004 and 2005-2014 to an average of 127 and 171 floods per year, respectively. While floods have the largest effect in Asia and Africa, they pose a danger around the world. For example, in a single month in July 2021, floods occurred in almost 400 different locations around the world. Tragically, 920 people across all continents lost their lives during these events and the resulting damage affected many more (Davies, 2021). With a rising sea level and more extreme weather conditions due to climate change, the risk of flooding is likely to increase in future decades. Therefore, flood protection systems which can drastically reduce the risk of flooding are vital for the safety of millions of people. Since effective flood protection technologies exist, better flood control is a so-called "low-hanging fruit" in disaster risk reduction (CRED and UNISDR, 2015). Moreover, flood protection systems are cost effective, i.e. the construction and maintenance costs of flood protection systems are often only a fraction of the repair cost (Tourment et al., 2018).

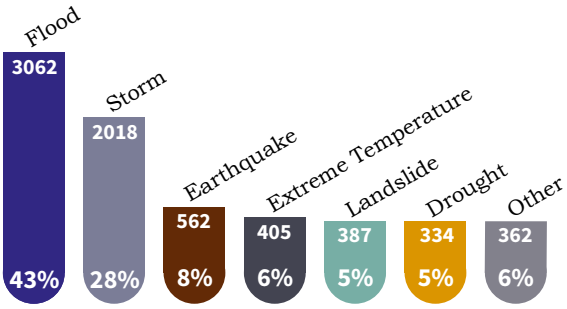

Figure 1.1: Number of occurrences of natural disasters worldwide by disaster type in the period from 1995-2014. Recreated based upon CRED and UNISDR (2015).

Due to the uncertain nature of (1) the loads acting on a flood protection system, and (2) the resistance of the structure, it is practically impossible to build a flood protection system which negates flood risk. The International Levee Handbook (ILH) (van Hemert et al., 2013) therefore promotes a risk-based approach to designing and maintaining dykes. According to this approach, the risk of flooding should be assessed based on the probability of a flood event and the consequence of the flood event to life, property and economic activity. The risk can be compared against the costs of the dyke to ensure a cost-effective solution. The costs of the dyke should also include the environmental and societal impact of the dyke. For example, a dyke construction might negatively influence a nature reserve, which should be reflected in the total cost of the dyke. The risk-based approach can also be used to apportion a financial budget for regional or national flood protection, such that the expected consequence is as low as possible once the budget has been spent. Many western countries now use such an approach, with details often varying between countries (Tourment et al., 2016; Tourment et al., 2018).

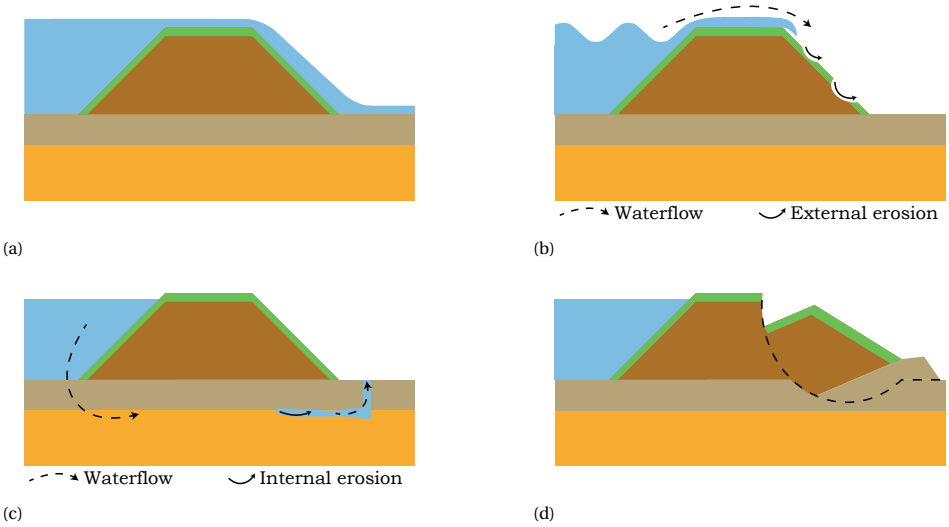

Figure 1.2: Examples of the dyke failure process categories according to the ILH (van Hemert et al., 2013); a) exceeding the hydraulic loads; b) external erosion; c) internal erosion; and d) large instabilities.

1.2. ASSESSMENT OF THE RISK OF FLOODING

To maintain the protection system according to the risk-based approach, continual risk monitoring is required. For example, the USACE monitors flood risks for dyke segments together with local entities in order to improve the levee safety decision making process (USACE, 2018). Unfortunately, continual risk monitoring is complex: flooding may occur due to many failure processes, and the risk of each process has to be monitored. Continuously monitoring the probability of all failure processes and their consequences is (often) impractical (Tourment et al., 2016). The ILH (van Hemert et al., 2013) categorises these failure processes in four groups, as illustrated in Figure 1.2: 1) exceeding the design hydraulic loads, 2) external erosion due to waves or overtopping, 3) internal erosion of soil particles caused by seepage flow, and 4) large instabilities due to a loss of equilibrium when the load exceeds the resistance.

To reduce the complexity of risk monitoring, the consequence of a dyke failure, i.e. flooding, can be evaluated independently of which failure process caused flooding, since the consequences of flooding are similar for all dyke failure processes (USACE, 2019). Separately evaluating the consequence of flooding from the failure process (which caused flooding) is used in, among others, the Czech Republic, Germany, the Netherlands, Switzerland and the United Kingdom (Tourment et al., 2018). More specifically, in the Netherlands the consequences of flooding have been used to define the maximum allowable probability of flooding for all primary dyke segments (Waterwet, 2009). The combined probability of the separate processes is compared against the allowed maximum on a regular basis. In theory, a failure process should therefore be assessed up to a breach (Klein Breteler et al., 2009). However, due to technical or knowledge limitations often only a part of the failure process is evaluated - the so-called primary mechanism.

The later steps in the failure process, which are often ignored, may not occur due to the remaining resistance of the dyke, thereby preventing flooding (Calle, 2002). Ignoring this remaining resistance leads to inefficient dyke designs. Note that allowing the possibility of relatively frequent dyke slope failure is impractical, for example due to the potential failure of the damaged dyke in a new storm event or frequent large repair costs. Including remaining resistance should therefore only be required in extreme events, such that frequent repairs will not be necessary. During a dyke assessment/design, preventing flooding could be considered as an ultimate limit state, while preventing initial failure could be considered as a serviceability limit state, with different probabilities associated with each limit state.

This research project investigates how the remaining resistance can be included in dyke safety assessments, thereby assisting in the implementation of the new risk-based flood protection standards of the Netherlands. The project is part of the All-Risk program (Kok et al., 2022), a program consisting of 14 PhD and 4 postdoc research positions, which aims to support the objectives of the Dutch Flood Protection Program (HWBP) in implementing the new flood safety norms. The program is subdivided into 5 subprojects: A) risk framework; B) dynamics in hydraulic loads; C) subsoil heterogeneity; D) reliability of flood defenses; and E) law, governance and implementation. This work is part of sub-project D, and has connections with sub-project C.

1.3. REMAINING RESISTANCE FOR SLOPE INSTABILITIES

In this thesis, the focus is on modelling the remaining dyke resistance after initial slope instabilities, i.e. a failure process in the large instabilities failure category is considered (van Hemert et al., 2013). After initial slope instabilities, a significant amount of remaining resistance can still be available, especially for wide dykes or dykes which are significantly higher than the expected external water level (Calle, 2002). The assessment of slope (in)stability usually only predicts the moment when a loss of equilibrium occurs (MIM, 2016), i.e. it predicts the development of the first crack of a slide and ignores the remainder of the failure process after slope instabilitity, see Figure 1.3.

The loss of equilibrium is typically estimated using the Limit Equilibrium Method (LEM) or the Finite Element Method (FEM) (MIM, 2016; Salunkhe et al., 2017). In LEM, the shape of the failure surface is, historically, assumed and the factor of safety (FoS) – the ratio of resisting to adverse loads or moments – is computed (Bishop, 1955; Huang, 2014). By evaluating multiple potential failure surfaces, the lowest FoS can be found, which is considered to be the critical FoS of the dyke. In current versions of LEM, prior assumptions regarding the failure surface are no longer required. In contrast to LEM, FEM computes the stress-strain behaviour using a spatial discretisation of the dyke material using a mesh and a material model (Griffiths and Lane, 2001; Smith et al., 2014; Zienkiewicz et al., 2014). FEM automatically locates the failure surface without any prior assumptions regarding its shape, similar to the latest versions of LEM. It does this by systematically reducing the strength of the material until failure occurs, thereby determining the FoS (Matsui and San, 1992). However, at failure large deformations typically occur and, due to the large deformation of the mesh, it may become inappropriate for further computation.

Probabilistic methods, such as Monte-Carlo simulation or the First Order Reliability Method (FORM), are used to compute the probability of initial failure from the full range of combinations of loads and resistances. These probabilistic methods use LEM or FEM to determine the load and resistance combinations which lead to a FoS below one. Alternatively, a semi-probabilistic assessment can be used, where design values of the loads and resistances are determined. The design values are used in a single 'deterministic' computation with LEM or FEM, which indicates if the dyke meets the design criteria. In the Netherlands, for consistency between the probabilistic and semi-probabilistic approaches, an empirical formula is used to compute a probability of initial failure from the FoS of the semi-probabilistic computation. This formula has been calibrated against the probabilistic approach (Kanning et al., 2016).

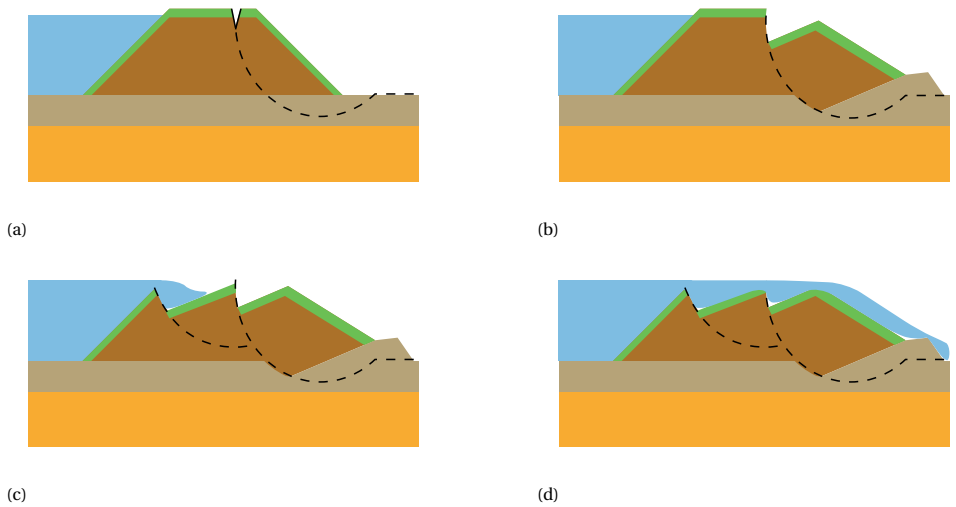

Figure 1.3: Dyke slope failure process from initiation until breach, based on Calle (2002): a) lack of equilibrium causes a first crack, b) which develops into a first slope failure; c) which may be followed by secondary slope failures; and d) complete failure occurs once the dyke drops below the water level causing a breach.

The probability of initial failure is often used as the probability of flooding due to slope instability, i.e. the remaining resistance is ignored. However, a new equilibrium can be reached after only a small failure occurs, and the remaining stable portion of a dyke can still prevent flooding, i.e. a new equilibrium is reached after Figure 1.3b (Calle, 2002; ENW, 2009). Secondary mechanisms, such as secondary instabilities, erosion due to overtopping or internal erosion, could then occur and cause flooding. Unfortunately, while LEM and FEM are accurate methods to calculate the probability of the occurrence of the initial failure, LEM and FEM cannot be used to predict the process after initial failure. LEM does not compute deformations, while FEM stops working as a result of large deformations causing excessive mesh distortions. Therefore, these methods cannot be directly used to predict ongoing process(es) after an initial failure. As an alternative, several guidelines exist to determine the remaining dyke resistance based on the initial failure surface from LEM and/or FEM computations (Blinde et al., 2018; ENW, 2009;

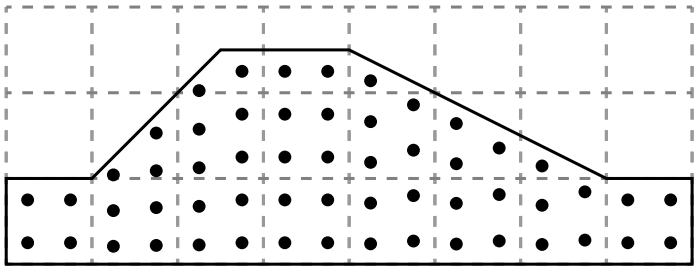

Figure 1.4: A material point discretisation (black dots) of a dyke on top of a background grid (dashed lines).

Knoeff et al., 2021; MIM, 2016). These guidelines construct a remaining dyke profile with assumptions on the deformation and displacement of the initial failure block, and they allow a reduction of the probability of flooding if the remaining dyke profile exceeds a minimum size. However, while several guidelines exist, the assumptions lack an experimental or numerical background and are therefore often over-conservative.

Recently, LEM has been used to compute secondary (slope) failures (van der Krogt et al., 2019). Simple deformation assumptions (similar to the previously mentioned guidelines), such as rotational sliding along the most critical slip plane until a crest settlement of half the dyke height is reached, have been used to manually construct a remaining dyke profile. The probability of a secondary failure can then be computed using LEM with the new geometry. The process is repeated until flooding occurs, and the probability of flooding is computed as the product of the probabilities of failure of each step (van der Krogt et al., 2019). While this method is limited to assumptions on the remaining profile, it can estimate the probabilities of flooding given the formation of the remaining profile. To construct the remaining profile accurately, and verify the assumptions used in the guidelines and by van der Krogt et al. (2019), a method which can assess the probability and behaviour of the entire failure process is required.

1.4. THE MATERIAL POINT METHOD

The Material Point Method (MPM) (Sulsky et al., 1994), a recently developed large deformation variant of FEM, is capable of modelling the entire failure process, and can therefore be used to more accurately compute the deformations of the failure block. MPM uses both (material) point and mesh discretisation schemes. The continuum is represented by a set of material points, while the mesh is only used as a computational grid, see Figure 1.4. Each computation step consists of three substeps, as illustrated in Figure 1.5: 1) the properties of the material points are mapped to the background grid using shape functions; 2) the displacements of the nodes of the background grid are computed using standard FEM schemes; and 3) the nodal displacements are used to update the material point positions and properties. At the end of each step the grid can be reset or a new grid can be created, while the material points remain in their new positions and maintain the properties of the material. Since the mesh can be reset, mesh

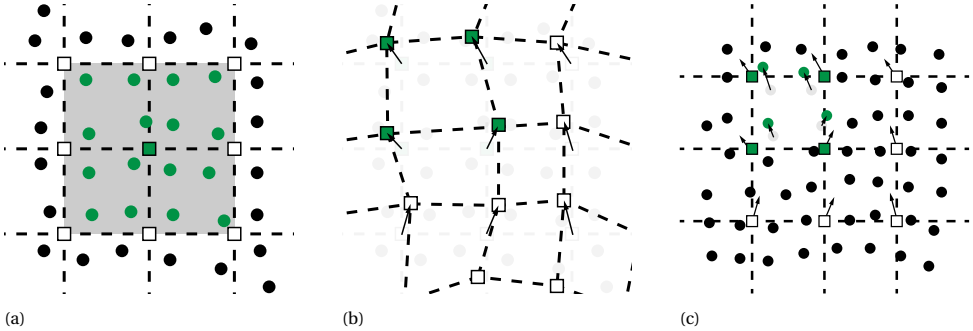

Figure 1.5: The computational substeps of MPM. Note that the the displacements are exaggerated for illustrative purposes. (a) The properties of the material points are mapped to the background grid using shape functions. The green material points are located within the elements connected to the green node, and therefore influence this node. (b) The displacements of the nodes are computed using standard FEM schemes. (c) The nodal displacements are used to update the material point positions and properties. The green material points are updated according to the displacements of the green nodes, i.e. the nodes of the element they were contained within. The grid is then reset for the next step in the computation.

distortion is no longer an issue and large deformations can theoretically be computed. Thus, MPM can be seen as an extension of FEM, where the Gauss integration points have been replaced by moving material points. MPM has been proven to successfully model large deformations for a wide range of geotechnical applications (Andersen and Andersen, 2010; Fern et al., 2019; González Acosta et al., 2021; Phuong et al., 2016; Sołowski and Sloan, 2015; Wang et al., 2016b; Yerro et al., 2016; Zheng et al., 2022), including dyke slope failure modelling (Coelho et al., 2019; Fern et al., 2017; Martinelli et al., 2017; Zabala and Alonso, 2011).

Recent research has focused on reducing stress oscillations occurring when material points move within and across background grid elements (Bardenhagen and Kober, 2004; de Koster et al., 2021; González Acosta et al., 2020; Sadeghirad et al., 2011; Sadeghirad et al., 2013; Tielen et al., 2017; Zhang et al., 2011; Zheng et al., 2021, 2022). The application of boundary conditions (BCs) has received less attention, even though their application is non-trivial in MPM. In FEM, boundary conditions (BCs) can be easily applied at the edges of the finite element mesh, which correspond with the edges of the material. However, as material points move within the mesh in MPM, the boundary of the material will not remain at the edge of the mesh and may not even be initialised at a mesh edge. Moreover, material points are, by definition, not at the boundary of the material, since they are at the centre of the material (mass) they represent. Therefore, applying BCs on either the material points or the background grid directly may not be appropriate and could lead to inaccuracies. In recent studies, the boundary has been represented by composite curves, either B-Splines or Bezier curves, and both traction conditions as well as fixities have been applied successfully when the location of the boundary is known (Bing et al., 2019; Cortis et al., 2018; Remmerswaal, 2017). However, in general the location of the boundary is unknown and must instead be detected based on the location and properties of the material points.

In order to model dyke failure up to the point of flooding, the external loads of the water on the outer slope are important and an accurate boundary condition is therefore required. This boundary may move due to dyke deformations, so that the boundary cannot be easily aligned with the background grid, and development of an accurate moving boundary condition is necessary.

1.5. THE RANDOM MATERIAL POINT METHOD

Dykes consist of a wide variety of material compositions, and are often built upon foundations made of several soil layers. Large variations in the soil properties within these layers exist. In practice, the material composition of the dyke and its foundation is measured with CPTs and boreholes, from which the probability density distribution of the properties can be estimated. These distributions can then be used as the input for the (semi-)probabilistic calculation required to compute the probability of flooding. In most calculations, a soil layer is assumed to be homogeneous, i.e. the soil layer can be defined by a single set of property values, and the probability density function of each property is used as the likelihood that this layer has a specific property value. However, in reality, the properties of the soil layers are spatially variable, i.e. small variations exist within a layer. This spatial variability within a soil layer is here called soil heterogeneity. It can have a large impact on the failure initiation and post-failure process, which is typically ignored in standard (semi)-probabilistic calculations.

The Random Finite Element Method (RFEM) uses random fields as a representation of soil heterogeneity in combination with FEM within a Monte Carlo framework (Griffiths and Fenton, 2004; Hicks and Li, 2018; Hicks and Spencer, 2010; van den Eijnden and Hicks, 2018). Simulations with RFEM have shown that the heterogeneity of the soil strength has a significant impact on the initial failure surface, due to the failure seeking the weakest path through the soil skeleton. RFEM allows the calculation of the probability of dyke failure in a manner similar to a standard probabilistic calculation that does not consider soil heterogeneity. Comparing this method with a standard probabilistic calculation based only on the point statistics, the mean FoS response in RFEM is generally lower due to the impact of weaker zones. In RFEM, the failure mechanism can seek the weakest path (through the weak zones), which is not possible in standard probabilistic calculations using FEM (with a single strength property for each layer). The uncertainty in the response of RFEM is generally lower compared to standard probabilistic FEM, due to the averaging of soil properties. This usually results in a higher overall minimum FoS in RFEM compared to probabilistic FEM with a higher confidence interval. Hence, the calculated probability of failure usually decreases, such that RFEM is less over-conservative.

It is to be expected that this soil heterogeneity has a similar impact on any secondary failure mechanisms, and on the development of large deformations. Therefore, heterogeneity should be accounted for when assessing residual dyke resistance. MPM can be combined with random fields in a manner similar to RFEM, to give the Random Material Point Method (RMPM), to enable the inclusion of heterogeneity in the assessment of large deformations (Ma et al., 2022; Wang et al., 2016a). RMPM has yet to be applied in a dyke assessment setting.

1.6. AIMS AND OBJECTIVES OF THESIS

This thesis applies RMPM for slope stability modelling. The principal aim is to demonstrate a framework for quantifying residual dyke resistance in 2D, and a secondary aim is to perform preliminary investigations into the impact of spatial variability on 3D slope failure processes in general. The main objectives are as follows:

1. Investigate and improve the methods for the application of boundary conditions in MPM, such that traction conditions can be applied on moving geometries with limited errors.

2. Develop a reliability-based framework for quantifying residual dyke resistance after occurence of the primary failure mechanism, and specifically to implement that framework here for residual dyke resistance following slope instability. This naturally leads to the implementation of RMPM.

3. Investigate the effect of spatial variability on the (dyke) slope failure processes in (a) two and (b) three dimensions, and give insights into the effectiveness of the existing guidelines for residual dyke resistance. Although this initial study investigates the potential of 3-dimensional RMPM analyses for the investigation of 3D failures in a sensitive clay, it will additionally indicate potential failure patterns applicable for 3-dimensional dyke failures.

1.7. THESIS OUTLINE

The remainder of this thesis is divided into 6 further chapters:

Chapter 2 further details the background of MPM. Firstly, the formulation of FEM is presented together with the application of boundary conditions in FEM. The required modifications to move from FEM to MPM are then described, after which some of the more recent improvements in MPM, such as reducing stress oscillations and volumetric locking, are discussed.

Chapter 3 proposes an improvement to the traction boundary conditions in MPM (Objective 1). It extends the literature review on MPM, with a focus on the application of boundary conditions, and uses this background to design four boundary condition methods. The methods are evaluated for 1- and 2-dimensional benchmarks to evaluate the inconsistencies associated with the different methods. Since many stress oscillation improvement techniques change the material discretisation, the boundary conditions in the Generalized Interpolation Material Point (GIMP) method, a widely used improvement technique, are also studied. It is demonstrated that there are two viable boundary condition methods, and algorithms are designed to generate the surfaces required for these two methods. The algorithms and the associated boundary conditions are tested by modelling the hydrostatic pressures for a submerged slope failure.

Chapter 4 presents the risk-based framework (Objective 2). This framework first evaluates the probability of a primary mechanism using fragility curves, and then computes the probability of flooding given this primary mechanism. For residual dyke resistance after initial slope failure, this involves computing the likelihood of all potential subsequent slope failures until the dyke height drops below the water level. RMPM automat-

ically models the entire failure process from initial failure through to flooding, thereby implementing the risk framework.

In Chapter 5 the residual dyke resistance of a simplified dyke geometry is studied (Objective 3a). Several degrees of anisotropy, i.e. the degree of layering of the spatial variability, are used to observe the effect of the spatial variability. The size and deformation of the initial failure are measured, and correlated against the probability of flooding and residual dyke resistance. This correlation gives insight into the assumptions used in the existing guidelines for residual dyke resistance.

Three dimensional failure processes are investigated in Chapter 6 (Objective 3b). A small 45 degree slope is brought to failure under its own weight or by applying a foundation load when the slope is stable under its own weight. The differences between 2D and 3D failure processes are described. The effect of changes in the point statistics and degree of anisotropy of the material strength spatial variability are studied. Finally, a depth trend is introduced in the mean material strength to observe its effect on the failure process.

Chapter 7 summarises the main conclusions of this thesis, relates the research to dyke design in the Netherlands and gives recommendation for future research.

REFERENCES

Andersen, S. M., & Andersen, L. V. (2010). Modelling of landslides with the material-point method. *Computational Geosciences*, *14*(1), 137–147. https://doi.org/10.1007/s10596-009-9137-y

Bardenhagen, S. G., & Kober, E. M. (2004). The generalized interpolation material point method. *CMES - Computer Modeling in Engineering and Sciences*, *5*(6), 477–496. https://doi.org/10.3970/cmes.2004.005.477

Bing, Y., Cortis, M., Charlton, T. J., Coombs, W. M., & Augarde, C. E. (2019). B-spline based boundary conditions in the material point method. *Computers and Structures*, *212*, 257–274. https://doi.org/10.1016/j.compstruc.2018.11.003

Bishop, A. W. (1955). The use of the slip circle in the stability analysis of slopes. *Géotechnique*, *5*(1), 7–17. https://doi.org/10.1680/geot.1955.5.1.7

Blinde, J., Bisschop, C., de Visser, M., Jongejan, R., & Tigchelaar, J. (2018). *Afweging ter bepaling glijvlak voor faalmechanisme macrostabiliteit binnenwaarts (translated in English: Consideration for determining failure surface for failure mechanism macro-instability)* (Factsheet). Kennisplatform Risicobenadering.

Calle, E. O. F. (2002). *Dijkdoorbraakprocessen (translated in English: Dijk breach processes)* (tech. rep. CO-720201/39). GeoDelft.

Coelho, B. Z., Rohe, A., Aboufirass, A., Nuttall, J. D., & Bolognin, M. (2019). Assessment of dike safety within the framework of large deformation analysis with the material point method. In A. Cardoso, J. Borges, P. Costa, A. Gomes, J. Marques, & C. Vieira (Eds.), *Numerical Methods in Geotechnical Engineering IX* (1st ed., pp. 657–663). https://doi.org/10.1201/9781351003629

Cortis, M., Coombs, W., Augarde, C., Brown, M., Brennan, A., & Robinson, S. (2018). Imposition of essential boundary conditions in the material point method. *International Journal for Numerical Methods in Engineering*, *113*(1), 130–152. https://doi.org/10.1002/nme.5606

CRED, & UNISDR. (2015). *The human cost of weather related disasters 1995-2015* (tech. rep.). Centre for Research on the Epidemiology of Disasters (CRED) and United Nations Office for Disaster Risk Reduction (UNISDR).

Davies, R. (2021). *Worldwide – Over 920 people killed in floods and landslides in July 2021*. Floodlist. Retrieved August 24, 2021, from https://floodlist.com/asia/world-floods-july-2021

de Koster, P., Tielen, R., Wobbes, E., & Möller, M. (2021). Extension of B-spline material point method for unstructured triangular grids using Powell–Sabin splines. *Computational Particle Mechanics*, *8*(2), 273–288. https://doi.org/10.1007/s40571-020-00328-3

ENW. (2009). *Actuele sterkte van dijken (translated in English: Actual strength of dykes)* (tech. rep.). Expertisenetwerk Water Veiligheid.

Fern, E. J., de Lange, D. A., Zwanenburg, C., Teunissen, J. A. M., Rohe, A., & Soga, K. (2017). Experimental and numerical investigations of dyke failures involving soft materials. *Engineering Geology*, *219*, 130–139. https://doi.org/10.1016/j.enggeo.2016.07.006

Fern, E. J., Rohe, A., Soga, K., & Alonso, E. E. (2019). *The Material Point Method for Geotechnical Engineering* (J. Fern, A. Rohe, K. Soga, & E. Alonso, Eds.). CRC Press. https://doi.org/10.1201/9780429028090

González Acosta, J. L., Vardon, P. J., & Hicks, M. A. (2021). Study of landslides and soil-structure interaction problems using the implicit material point method. *Engineering Geology*, *285*, 106043. https://doi.org/10.1016/j.enggeo.2021.106043

González Acosta, J. L., Vardon, P. J., Remmerswaal, G., & Hicks, M. A. (2020). An investigation of stress inaccuracies and proposed solution in the material point method. *Computational Mechanics*, *65*, 555–581. https://doi.org/10.1007/s00466-019-01783-3

Griffiths, D. V., & Fenton, G. A. (2004). Probabilistic slope stability analysis by finite elements. *Journal of Geotechnical and Geoenvironmental Engineering*, *130*(5), 507–518. https://doi.org/10.1061/(ASCE)1090-0241(2004)130:5(507)

Griffiths, D. V., & Lane, P. A. (2001). Slope stability analysis by finite elements. *Géotechnique*, *51*(7), 653–654. https://doi.org/10.1680/geot.51.7.653.51390

Hicks, M. A., & Li, Y. (2018). Influence of length effect on embankment slope reliability in 3D. *International Journal for Numerical and Analytical Methods in Geomechanics*, *42*(7), 891–915. https://doi.org/10.1002/nag.2766

Hicks, M. A., & Spencer, W. A. (2010). Influence of heterogeneity on the reliability and failure of a long 3D slope. *Computers and Geotechnics*, *37*(7-8), 948–955. https://doi.org/10.1016/j.compgeo.2010.08.001

Huang, Y. H. (2014). *Slope Stability Analysis by the Limit Equilibrium Method*. American Society of Civil Engineers Press. https://doi.org/10.1061/9780784412886

Kanning, W., Teixeira, A., van der Krogt, M. G., & Rippi, K. (2016). *Derivation of the semi-probabilistic safety assessment rule for inner slope stability* (tech. rep. 1230086-009-GEO-0030). Deltares.

Klein Breteler, M., 't Hart, R., Verheij, H., & Knoeff, H. (2009). *Reststerkte van dijken na initiele schade (translated in English: Residual resistance of dykes after initial damage)* (tech. rep. 1200393-002-HYE-0010). Deltares.

Knoeff, H., Bossenbroek, J.-K., Jongejan, R., Bisschop, C., & de Visser, M. (2021). *Werkwijze falen door macrostabiliteit (translated in English: Workflow failure by macro-instability)* (Factsheet). Adviesteam dijkontwerp.

Kok, M., Cortes Arevelo, V. J., & Vos, M. (2022). *Towards Improved Flood Defences - Five Years of All-Risk Research into the New Safety Standards*. TU Delft OPEN Publishing. https://doi.org/10.34641/mg.31

Ma, G., Rezania, M., & Nezhad, M. M. (2022). Stochastic assessment of landslide influence zone by material point method and generalized geotechnical random field theory. *International Journal of Geomechanics*, *22*(4), 04022002. https://doi.org/10.1061/(ASCE)GM.1943-5622.0002308

Martinelli, M., Rohe, A., & Soga, K. (2017). Modeling dike failure using the material point method. *Procedia Engineering*, *175*, 341–348. https://doi.org/10.1016/j.proeng.2017.01.042

Matsui, T., & San, K.-C. (1992). Finite element slope stability analysis by shear strength reduction technique. *Soils and Foundations*, *32*(1), 59–70. https://doi.org/10.3208/sandf1972.32.59

MIM. (2016). *Schematiseringshandleiding macrostabiliteit (translated in English: Guidelines for schematization of macro-instability)* (tech. rep.). Ministerie van Infrastructuur en Milieu.

Phuong, N., van Tol, A., Elkadi, A., & Rohe, A. (2016). Numerical investigation of pile installation effects in sand using material point method. *Computers and Geotechnics*, *73*, 58–71. https://doi.org/10.1016/j.compgeo.2015.11.012

Remmerswaal, G. (2017). *Development and implementation of moving boundary conditions in the material point method* (Master's thesis). Delft University of Technology.

Sadeghirad, A., Brannon, R. M., & Burghardt, J. (2011). A convected particle domain interpolation technique to extend applicability of the material point method for problems involving massive deformations. *International Journal for Numerical Methods in Engineering*, *86*(12), 1435–1456. https://doi.org/10.1002/nme.3110

Sadeghirad, A., Brannon, R., & Guilkey, J. (2013). Second-order convected particle domain interpolation (CPDI2) with enrichment for weak discontinuities at material interfaces. *International Journal for Numerical Methods in Engineering*, *95*(11), 928–952. https://doi.org/10.1002/nme.4526

Salunkhe, D., Chvan, G., Bartakke, R. N., & Kothavale, P. R. (2017). An overview on methods for slope stability analysis. *International Journal of Engineering Research and*, *6*(03), 528–535. https://doi.org/10.17577/IJERTV6IS030496

Smith, I. M., Griffiths, D. V., & Margetts, L. (2014). *Programming the Finite Element Method* (5th ed.). John Wiley & Sons.

Sołowski, W. T., & Sloan, S. W. (2015). Evaluation of material point method for use in geotechnics. *International Journal for Numerical and Analytical Methods in Geomechanics*, *39*(7), 685–701. https://doi.org/10.1002/nag.2321

Sulsky, D., Chen, Z., & Schreyer, H. L. (1994). A particle method for history-dependent materials. *Computer Methods in Applied Mechanics and Engineering*, *118*(1-2), 179–196. https://doi.org/10.1016/0045-7825(94)90112-0

Tielen, R., Wobbes, E., Möller, M., & Beuth, L. (2017). A high order material point method. *Procedia Engineering, 175*, 265–272. https://doi.org/10.1016/j.proeng.2017.01.022

Tourment, R., Beullac, B., de Leeuw, A., Diermanse, F., Gouldby, B., & Wallis, M. (2016). The risk analysis of levee systems: A comparison of international best practices. *E3S Web of Conferences., 7*, 03009. https://doi.org/10.1051/e3sconf/20160703009

Tourment, R., Beullac, B., Peeters, P., Pohl, R., Bottema, M., Van, M., & Rushworth, A. (2018). *European and US levees and flood defences - Characteristics, risks and governance* (Research report). Irstea. https://hal.inrae.fr/hal-02609228

USACE. (2018). *Levee portfolio report - A summary of risks and benefits associated with the USACE levee portfolio* (tech. rep.). US Army Corps of Engineers (USACE).

USACE. (2019). Consequences of flooding. *Best practices in dam and levee safety risk analysis* (p. 54). U.S. Department of the Interior Bureau of Reclamation and U.S. Army Corps of Engineers.

van den Eijnden, A. P., & Hicks, M. A. (2018). Probability-dependent failure modes of slopes and cuts in heterogeneous cohesive soils. *Géotechnique Letters, 8*(3), 214–218. https://doi.org/10.1680/jgele.18.00043

van der Krogt, M. G., Schweckendiek, T., & Kok, M. (2019). Do all dike instabilities cause flooding? *13th International Conference on Applications of Statistics and Probability in Civil Engineering, ICASP 2019*. https://doi.org/10.22725/ICASP13.461

van Hemert, H., Igigabel, M., Pohl, R., Sharp, M., Simm, J., Tourment, R., & Wallis, M. (Eds.). (2013). *The International Levee Handbook*. CIRIA.

Wang, B., Hicks, M. A., & Vardon, P. J. (2016a). Slope failure analysis using the random material point method. *Géotechnique Letters, 6*(2), 113–118. https://doi.org/10.1680/jgele.16.00019

Wang, B., Vardon, P. J., & Hicks, M. A. (2016b). Investigation of retrogressive and progressive slope failure mechanisms using the material point method. *Computers and Geotechnics, 78*, 88–98. https://doi.org/10.1016/j.compgeo.2016.04.016

Waterwet. (2009). Waterlaw: BWBR0025458. http://wetten.overheid.nl/BWBR0025458/2018-01-01#

Yerro, A., Alonso, E. E., & Pinyol, N. M. (2016). Run-out of landslides in brittle soils. *Computers and Geotechnics, 80*, 427–439. https://doi.org/10.1016/j.compgeo.2016.03.001

Zabala, F., & Alonso, E. E. (2011). Progressive failure of aznalcó llar dam using the material point method. *Geotechnique, 61*(9), 795–808. https://doi.org/10.1680/geot.9.P.134

Zhang, D. Z., Ma, X., & Giguere, P. T. (2011). Material point method enhanced by modified gradient of shape function. *Journal of Computational Physics, 230*(16), 6379–6398. https://doi.org/10.1016/j.jcp.2011.04.032

Zheng, X., Pisanò, F., Vardon, P. J., & Hicks, M. A. (2021). An explicit stabilised material point method for coupled hydromechanical problems in two-phase porous media. *Computers and Geotechnics, 135*, 104112. https://doi.org/10.1016/j.compgeo.2021.104112

Zheng, X., Pisanò, F., Vardon, P. J., & Hicks, M. A. (2022). Fully implicit, stabilised mpm simulation of large-deformation problems in two-phase elastoplastic geomaterials. *Computers and Geotechnics*, *147*, 104771. https://doi.org/10.1016/j.compgeo.2022.104771

Zienkiewicz, O., Taylor, R., & Fox, D. (2014). *The Finite Element Method for Solid and Structural Mechanics* (7th ed.). Butterworth-Heinemann. https://doi.org/10.1016/B978-1-85617-634-7.00002-8

2

Background to the Material Point Method

2.1. INTRODUCTION

The Material Point Method (MPM) was originally developed as an extension of the FLuid Implicit Particle (FLIP) method, to handle history-dependent materials. FLIP, and its predecessor the Particle-In-Cell (PIC) method, use Lagrangian particles to model fluids. In PIC, the particles are used to store the mass and position of the material, while the other properties are still stored on element nodes. PIC is therefore only partially a Lagrangian method. FLIP is fully Lagrangian, as the fluid momentum and energy are also stored at the particles. Sulsky et al. (1994) used the particles, also called material points, to store the history dependent variables, thereby forming the method later referred to as MPM. MPM was also set up using the weak form of the Finite Element Method (FEM), and is therefore also often called a large deformation extension of FEM. MPM combines two discretisation schemes: 1) a finite element (FE) mesh discretisation of the computational domain on which the governing equations are solved, and 2) a material discretisation into material points (MPs) which store the material properties. The material properties are mapped (or integrated) from the MPs to the FE mesh. The MPs therefore act like moving FEM integration points: they are used in the integration process to form the nodal equations and their properties are updated due to the deformation of the mesh after solving the nodal equations. In other words, basic MPM can be thought of as FEM with moving rather than fixed (e.g. Gaussian) integration points.

This chapter presents the background to MPM as well as extensions of standard MPM. The chapter highlights this by starting with the basic FEM formulation, followed by a description of how MPM can be derived by extending the FEM formulation. The final section focuses on some of the improvements of the standard formulation, most of which reduce the (stress) oscillations occurring when MPs move.

2.2. FORMULATION OF FEM

Consider the conservation of momentum of a body with volume V and surface area Γ, as shown in Figure 2.1a. Assuming the body is an isolated system, the conservation of momentum is given as

$$\nabla \cdot \boldsymbol{\sigma} - \rho \boldsymbol{a} = \mathbf{0} \tag{2.1}$$

where $\boldsymbol{\sigma}$ is the Cauchy stress tensor, $\boldsymbol{a}$ is the acceleration and ρ is the mass density. External influences on the system may be prescribed displacements $\boldsymbol{u}^d$ on Γ_d, i.e. Dirichlet conditions, and/or three types of external loads: (1) body forces $\boldsymbol{b}$, (2) surface tractions $\boldsymbol{\tau}$, i.e. Neumann conditions, and/or (3) concentrated point loads $\boldsymbol{F}^c$. Note that concentrated point loads are non-physical and can cause numerical issues, such as non-convergence, but they can be useful for comparisons with analytical solutions. When applying the external loads $\boldsymbol{b}$, $\boldsymbol{\tau}$ and $\boldsymbol{F}^c$ on the volume V, surface Γ_τ and points k, respectively, a weak form of Eq. (2.1) can be constructed (Bathe, 2014):

$$\int_V (\bar{\boldsymbol{\epsilon}}\boldsymbol{\sigma} + \bar{\boldsymbol{u}}\rho\boldsymbol{a})\,\mathrm{d}V - \int_V (\bar{\boldsymbol{u}}\boldsymbol{b})\,\mathrm{d}V - \int_{\Gamma_\tau} \bar{\boldsymbol{u}}\boldsymbol{\tau}\,\mathrm{d}\Gamma_\tau - \sum_k \bar{\boldsymbol{u}}\boldsymbol{F}^c_k = 0 \tag{2.2}$$

where $\bar{\boldsymbol{u}}$ is an arbitrary virtual displacement and $\bar{\boldsymbol{\epsilon}}$ is an arbitrary virtual strain in accordance with $\bar{\boldsymbol{u}}$. While the external loads are included within Eq. (2.2), $\bar{\boldsymbol{u}}$ must be constrained to 0 at Γ_d, such that Eq. (2.2) fulfills the prescribed displacement constraints $\boldsymbol{u}^d$

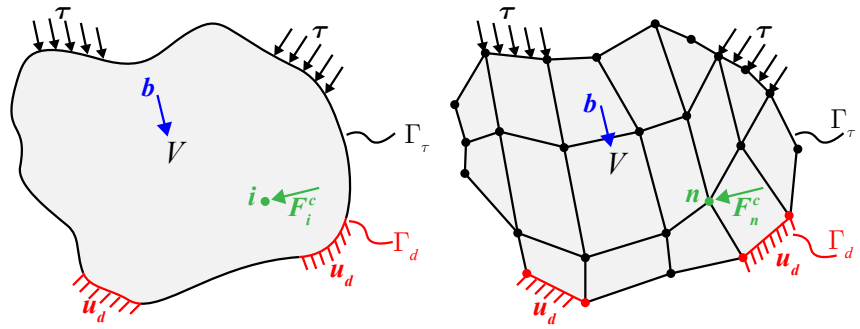

Figure 2.1: Body with volume V and surface Γ, under the influence of prescribed displacements $\boldsymbol{u}^d$, body forces $\boldsymbol{b}$, surface tractions $\boldsymbol{\tau}$ and concentrated point loads $\boldsymbol{F}^c$: (a) general body; (b) FEM discretisation.

on Γ_d (Bathe, 2014). Free surfaces with zero traction and no predefined displacements are included in Γ_τ, such that boundary conditions are specified on the complete surface, i.e. $\Gamma = \Gamma_\tau \cup \Gamma_d$.

The possibility of choosing an arbitrary virtual displacement allows for a general discretisation of Eq. (2.2), where each integral is evaluated element by element using the same set of equations (Bathe, 2014). However, the constraints of $\bar{\boldsymbol{u}}$ prevent choosing an arbitrary virtual displacement. Therefore, the prescribed displacements are often replaced by their 'known' equivalent reactions, i.e. the body is assumed to be a free floating body with surface loads equivalent to the actual surface loads plus the reaction forces. Eq. (2.2) can be changed to

$$\int_V (\bar{\boldsymbol{\varepsilon}}\boldsymbol{\sigma} + \bar{\boldsymbol{u}}\rho\boldsymbol{a})\,\mathrm{d}V - \int_V (\bar{\boldsymbol{u}}\boldsymbol{b})\,\mathrm{d}V - \int_\Gamma \bar{\boldsymbol{u}}\boldsymbol{\tau}\,\mathrm{d}\Gamma - \sum_k \bar{\boldsymbol{u}}\boldsymbol{F}_k^c = 0 \tag{2.3}$$

with $\Gamma_d = 0$ and $\Gamma_\tau = \Gamma$, i.e. all displacement constraints have been changed to reaction forces.

Eq. (2.3) can be discretised using standard FEM discretisation into nodes and elements (see Figure 2.1b) (González Acosta et al., 2020) and expressed in matrix form:

$$\mathbf{M}^t\boldsymbol{a} + \mathbf{K}^t\Delta\boldsymbol{u} = \left(\boldsymbol{F}_{\text{body}} + \boldsymbol{F}_{\text{traction}} + \boldsymbol{F}_{\text{point}} - \boldsymbol{F}_{\text{int}}\right)^{t+\Delta t} \tag{2.4}$$

where $\mathbf{M}$ is the mass matrix, $\boldsymbol{a}$ is the vector of nodal accelerations, $\mathbf{K}$ is the stiffness matrix, $\Delta\boldsymbol{u}$ is the vector of nodal incremental displacements, and $\boldsymbol{F}_{\text{body}}$, $\boldsymbol{F}_{\text{traction}}$, $\boldsymbol{F}_{\text{point}}$ and $\boldsymbol{F}_{\text{int}}$ are the nodal body forces, surface tractions, point loads and internal forces, respectively. $\mathbf{M}$ and $\mathbf{K}$ are formed using an element assembly procedure, after the element mass and stiffness matrices, $\mathbf{M}^t_{\text{ele}}$ and $\mathbf{K}^t_{\text{ele}}$, respectively, have been integrated:

$$\mathbf{M}^t = \mathop{\mathbb{A}}_{ele=1}^{nel} \mathbf{M}^t_{\text{ele}} = \mathop{\mathbb{A}}_{ele=1}^{nel} \int_{V_{ele}} \rho\mathbf{N}^{\mathrm{T}}\mathbf{N}\,dV_{ele} \tag{2.5}$$

and

$$\mathbf{K}^t = \mathop{\mathbb{A}}_{ele=1}^{nel} \mathbf{K}^t_{\text{ele}} = \mathop{\mathbb{A}}_{ele=1}^{nel} \int_{V_{ele}} \mathbf{B}^{\mathrm{T}}\mathbf{D}\mathbf{B}\, dV_{ele} \tag{2.6}$$

where $\mathop{\mathbb{A}}_{ele=1}^{nel}$ indicates the element assembly procedure over nel elements, ρ is the material density, $\mathbf{D}$ is the stress-strain matrix, $\mathbf{N}$ is the shape function matrix, $\mathbf{B}$ is the strain-displacement matrix constructed from shape function derivatives, and V_{ele} is the volume of an element. For details of the matrices involved the reader is referred to Smith et al. (2014). $\mathbf{M}^t_{\text{ele}}$ and $\mathbf{K}^t_{\text{ele}}$ are obtained numerically using Gauss integration:

$$\mathbf{M}^t_{\text{ele}} = \sum_{j=1}^{nip} \rho_j W_j \det|\mathbf{J}|_j \mathbf{N}_j^{\mathrm{T}}\mathbf{N}_j \tag{2.7}$$

and

$$\mathbf{K}^t_{\text{ele}} = \sum_{j=1}^{nip} W_j \det|\mathbf{J}|_j \mathbf{B}_j^{\mathrm{T}}\mathbf{D}_j\mathbf{B}_j \tag{2.8}$$

where W_j is the Gauss integration weight belonging to integration point j, $\mathbf{J}$ is the Jacobian matrix relating the global and local element coordinate systems, and nip is the number of integration points within each element.

Similarly, the body, traction and internal forces are computed per element and assembled into the nodal forces for all equations, such that

$$\boldsymbol{F}_{\text{body}} = \mathop{\mathbb{A}}_{ele=1}^{nel} \int_{V_{ele}} \mathbf{N}^{\mathrm{T}}\boldsymbol{b}\, \mathrm{d}V_{ele} = \mathop{\mathbb{A}}_{ele=1}^{nel} \sum_{j=1}^{nip} \mathbf{N}_j^{\mathrm{T}}\rho_j \boldsymbol{g} W_j \det|\mathbf{J}|_j \tag{2.9}$$

$$\boldsymbol{F}_{\text{traction}} = \mathop{\mathbb{A}}_{ele=1}^{nel} \int_{\Gamma_{ele}} \mathbf{N}^{\mathrm{T}}\boldsymbol{\tau}\, \mathrm{d}\Gamma_{ele} = \mathop{\mathbb{A}}_{ele=1}^{nel} \sum_{j_b=1}^{nipb} W_{j_b} \mathbf{N}_{i_b}^{\mathrm{T}} \boldsymbol{\tau}_{j_b} \tag{2.10}$$

$$\boldsymbol{F}_{\text{int}} = \mathop{\mathbb{A}}_{ele=1}^{nel} \int_{V_{ele}} \mathbf{B}^{\mathrm{T}}\boldsymbol{\sigma}^{t+\Delta t}\, \mathrm{d}V_{ele} = \mathop{\mathbb{A}}_{ele=1}^{nel} \sum_{j=1}^{nip} \mathbf{B}_j^{\mathrm{T}}\boldsymbol{\sigma}_j^{t+\Delta t} W_j \det|\mathbf{J}|_j \tag{2.11}$$

where $\boldsymbol{g}$ is the gravity vector, subscript j_b denotes a integration point along the boundary of an element, and $nipb$ is the total number of boundary integration points per element. Since point loads may only be applied at the nodes of the finite element mesh, element assembly is not needed for $\boldsymbol{F}_{\text{point}}$, which is instead given by

$$\boldsymbol{F}_{\text{point}} = \sum_{i=1}^{nn} \boldsymbol{F}_i^c \tag{2.12}$$

The external forces are usually grouped together:

$$\boldsymbol{F}_{\text{ext}} = \boldsymbol{F}_{\text{body}} + \boldsymbol{F}_{\text{traction}} + \boldsymbol{F}_{\text{point}} \tag{2.13}$$

Eq. (2.4) may then be simplified to

$$\mathbf{M}^t\boldsymbol{a} + \mathbf{K}^t\Delta\boldsymbol{u} = (\boldsymbol{F}_{\text{ext}} - \boldsymbol{F}_{\text{int}})^{t+\Delta t} \tag{2.14}$$

2.3. TIME INTEGRATION SCHEMES

A quasi-static formulation of Eq. (2.14) can be obtained by ignoring the inertia terms, i.e. $\mathbf{M}^t \boldsymbol{a}$ in Eq. (2.14), such that

$$\mathbf{K}^t \Delta \boldsymbol{u} = (\boldsymbol{F}_{\text{ext}} - \boldsymbol{F}_{\text{int}}) \tag{2.15}$$

The quasi-static formulation can be used to model processes undergoing slow movements. In this formulation, equilibrium is reached within each load step using a Newton-Raphson iteration procedure:

$$\mathbf{K}^{t\,k} \delta \boldsymbol{u} = {}^{k-1}(\boldsymbol{F}_{\text{ext}} - \boldsymbol{F}_{\text{int}}) \tag{2.16}$$

where the left superscript k refers to the value at the end of an iteration step, and $\delta \boldsymbol{u}$ is the displacement within the iteration step, such that the deformation within one loadstep ($\Delta \boldsymbol{u}$) is computed as

$${}^{k}\Delta \boldsymbol{u} = {}^{k-1}\Delta \boldsymbol{u} + {}^{k}\delta \boldsymbol{u} \tag{2.17}$$

This process is iterated until no further displacements are computed.

For the cases where the dynamics cannot be ignored, Eq. (2.14) can also be discretised in time using a scheme which relates the acceleration ($\boldsymbol{a}$) and velocity ($\boldsymbol{v}$) in terms of the displacement. Here a Newmark time integration scheme (Newmark, 1959) is used:

$$\boldsymbol{a}^{t+\Delta t} = \frac{\Delta \boldsymbol{u}}{\beta \Delta t^2} - \frac{\boldsymbol{v}^t}{\beta \Delta t} - (\frac{1}{2\beta} - 1)\boldsymbol{a}^t \tag{2.18}$$

and

$$\boldsymbol{v}^{t+\Delta t} = \frac{\gamma \Delta \boldsymbol{u}}{\beta \Delta t} - (\frac{\gamma}{\beta} - 1)\boldsymbol{v}^t - (\frac{\gamma}{2\beta} - 1)\Delta t \boldsymbol{a}^t \tag{2.19}$$

Time stepping paramters $\gamma = 0.5$ and $\beta = 0.25$ have been chosen, such that a constant average acceleration is used in each time step, which simplifies the relationships to

$$\boldsymbol{a}^{t+\Delta t} = \frac{4\Delta \boldsymbol{u}}{\Delta t^2} - \frac{4\boldsymbol{v}^t}{\Delta t} - \boldsymbol{a}^t \tag{2.20}$$

and

$$\boldsymbol{v}^{t+\Delta t} = 2\Delta \boldsymbol{u} - \boldsymbol{v}^t \tag{2.21}$$

Substituting Eq. (2.20) into Eq. (2.14), and again using a Newton-Raphson iteration procedure, leads to

$$\left(\frac{4\,{}^{k}\delta \boldsymbol{u}}{\Delta t^2} + \frac{4\,{}^{k-1}\Delta \boldsymbol{u}}{\Delta t^2} - \frac{4\boldsymbol{v}^t}{\Delta t} - \boldsymbol{a}^t\right)\mathbf{M}^t + \mathbf{K}^{t\,k}\delta \boldsymbol{u} = {}^{k-1}(\boldsymbol{F}_{\text{ext}} - \boldsymbol{F}_{\text{int}}) \tag{2.22}$$

Moving all knowns to the right-hand side and simplifying leads to an equation similar to the quasi-static formulation:

$$\mathbf{K}^{*,t\,k}\delta \boldsymbol{u} = {}^{k-1}(\boldsymbol{F}_{\text{ext}} + \boldsymbol{F}_{\text{kin}} - \boldsymbol{F}_{\text{int}})^{t+\Delta t} \tag{2.23}$$

where

$$\mathbf{K}^{*,t} = \mathbf{K}^t + \frac{4}{\Delta t^2}\mathbf{M}^t \tag{2.24}$$

and

$$\boldsymbol{F}_{\text{kin}} = \frac{4^{k-1}\Delta\boldsymbol{u}}{\Delta t^2} - \frac{4\boldsymbol{v}^t}{\Delta t} - \boldsymbol{a}^t \tag{2.25}$$

$\mathbf{K}^*$ represents a modified stiffness matrix (combining $\mathbf{K}$ and $\mathbf{M}$) and $\boldsymbol{F}_{\text{kin}}$ are the additional kinetic forces which take account of the inertia of the body (see Wang et al. (2016) for further details).

Finally, as an alternative to the implicit dynamic formulation, an explicit dynamic formulation can be used by setting $\beta = 0$. The acceleration can then be used as the primary variable:

$$\mathbf{M}^t\boldsymbol{a} = (\boldsymbol{F}_{\text{ext}} - \boldsymbol{F}_{\text{int}})^{\text{t}} \tag{2.26}$$

where, since the primary variable is solved purely based on quantities known at the start of the step, $\mathbf{K}$ is not required, and the stiffness of the material is accounted for only by $\boldsymbol{F}_{\text{int}}$. Moreover, when a lumped mass matrix is used the nodal equations can be solved separately, i.e. solving a system of equations is not needed. This significantly decreases the computation time of an individual time step. However, the explicit scheme is only conditionally stable, and therefore much smaller time steps are required for the explicit formulation compared to the implicit formulation. The total computation cost of an implicit formulation is, therefore, for many transient problems, lower than that of an explicit formulation (Zienkiewicz et al., 2014).

2.4. DISPLACEMENT BCS

Eqs. (2.16), (2.23) and (2.26) fulfill the external load conditions, but the displacement (Dirichlet) conditions must still be enforced. To enforce the displacement BCs, the reaction forces of the displacement BCs are computed and added to the external loads. However, computing the reaction forces before the system of equations has been solved can be a difficult procedure. Therefore, to enforce zero displacement BCs, the equations related to a node can instead be removed from the system of equations (Bathe, 2014; Smith et al., 2014). The reaction forces do not then have to be computed before the system is solved, but can be computed afterwards when desired. Alternatively, the penalty method can be employed for both non-zero and zero displacement BCs. In this method a penalty term is added to the diagonal of the stiffness matrix and the external force vector, thereby fixing the value of $\boldsymbol{u}$ to $\boldsymbol{u}_d$ at Γ_d. If an explicit time integration scheme is employed together with a lumped mass matrix, in a single step there is no coupling of the primary variable between the boundary and non-boundary nodes, and Dirichlet conditions can therefore be easily enforced on the boundary nodes without influencing the other nodes in the step (Zienkiewicz et al., 2014).

2.5. FORMULATION OF MPM

In MPM, a body is no longer discretised into elements and nodes, since material points are used instead, see Figure 2.2a. Each computation step consists of three parts, see Figure 1.5. At the start of the computation step all the information is stored at the MPs. Therefore, in the first part the state variables must be mapped/integrated to the nodes of the computational grid. The integration of the body force and internal force is similar

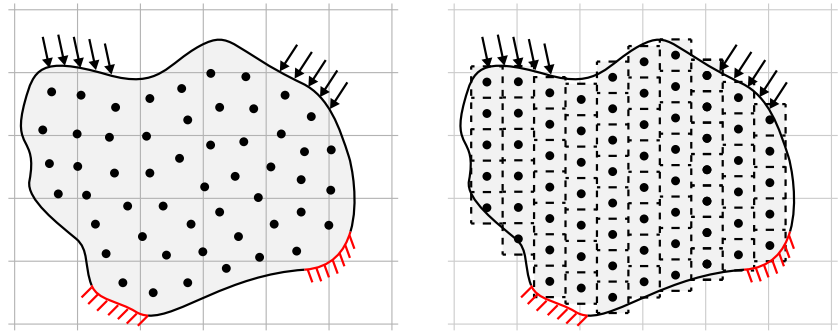

(a) (b)

Figure 2.2: Body of Figure 2.1 discretised using (a) MPM with MPs on a background grid, and (b) GIMP with MPs and support domains on a background grid.

to FEM, but changed from a Gaussian integration per element to a summation over the MPs:

$$\boldsymbol{F}_{\text{body}} = \sum_{p=1}^{nmp} \mathbf{N}_p^{\mathrm{T}} m_p \boldsymbol{g} \tag{2.27}$$

and

$$\boldsymbol{F}_{\text{int}} = \sum_{p=1}^{nmp} \mathbf{B}_p^{\mathrm{T}} \boldsymbol{\sigma}_p^{t+\Delta t} V_p \tag{2.28}$$

where $\mathbf{N}_p$ and $\mathbf{B}_p$ are the shape function and shape function derivative matrices evaluated at MP p, m_p is the mass of p,V_p is the volume of p and nmp is the total number of MPs. The mass matrix and stiffness matrix are still formed using the assembly procedure (Eqs. (2.5) and (2.6)), but the element matrices are modified to

$$\mathbf{M}_{\text{ele}}^t = \sum_{p=1}^{emp} \mathbf{N}_j^{\mathrm{T}} \mathbf{N}_j m_p \tag{2.29}$$

and

$$\mathbf{K}_{\text{ele}}^t = \sum_{p=1}^{emp} \mathbf{B}_p^{\mathrm{T}} \mathbf{D}_p \mathbf{B}_p V_p \tag{2.30}$$

where emp is the number of MPs in a specific element. Besides the integration also required in FEM, additional integration is required to obtain variables which are unknown at the nodes in MPM, for example $\boldsymbol{a}^t$ and $\boldsymbol{v}^t$, since the mesh has been reset compared to the previous step. Therefore, the velocity and acceleration at node i are computed as

$$\boldsymbol{v}_i^t = \frac{\sum_{p=1}^{nmp} \mathbf{N}_p^{\mathrm{T}} m_p \boldsymbol{v}_p^t}{m_i} \tag{2.31}$$

and

$$\boldsymbol{a}_i^t = \frac{\sum_{p=1}^{nmp} \mathbf{N}_p^{\mathrm{T}} m_p \boldsymbol{a}_p^t}{m_i} \tag{2.32}$$

where m_i is the mass of node i (computed by lumping the mass matrix) and $\boldsymbol{v}_p$ and $\boldsymbol{a}_p$ are the MP velocity and acceleration, respectively.

Once all the required variables are mapped to the mesh, in the second step the momentum or equilibrium equation (Eq. (2.16), (2.23) or (2.26)) is solved at the nodes, which results in a new nodal displacement, velocity and acceleration. While in the explicit scheme the equation is solved directly and the MP variables do not have to be updated during the second part of the computation, in the implicit scheme the stress and strain of the MPs must be updated in each iteration of the Newton-Rahpson procedure according to

$$ {}^{k}\boldsymbol{\sigma}_p^{t+\Delta t} = \boldsymbol{\sigma}_p^t + \mathbf{D}_p\mathbf{B}_p\, {}^{k}\Delta\boldsymbol{u} \tag{2.33}$$

For the case in which non-linear stress-strain behaviour, for example plastic behaviour, is being modelled, Eq. (2.33) is used to compute a trial stress, after which a constitutive model is used to correct the stresses and strains. After the MP stress is computed, the internal forces are recalculated using Eq. (2.28) at the start of the new iteration.

In the third part of the time step the MP variables are updated. In the explicit scheme this entails

$$ \boldsymbol{v}_p^{t+\Delta t} = \boldsymbol{v}_p^t + \mathbf{N}_p\boldsymbol{a}\Delta t \tag{2.34}$$

$$ \boldsymbol{x}_p^{t+\Delta t} = \boldsymbol{x}_p^t + \boldsymbol{u}_p = \boldsymbol{x}_p^t + \boldsymbol{v}_p^{t+\Delta t}\Delta t \tag{2.35}$$

$$ \boldsymbol{\sigma}_p^{t+\Delta t} = \boldsymbol{\sigma}_p^t + \mathbf{D}_p\mathbf{B}_p\Delta\boldsymbol{u}^* \tag{2.36}$$

where $\Delta\boldsymbol{u}^*$ is the incremental displacement obtained from a remapping of the updated MP velocities to the nodes, i.e.

$$ \Delta\boldsymbol{u}^* = \frac{\sum_{p=1}^{nmp}\mathbf{N}_p^{\mathrm{T}} m_p \boldsymbol{v}_p^{t+\Delta t}}{m_i}\Delta t \tag{2.37}$$

The remapping of the velocity is used for additional stability.

In the implicit scheme, the nodal displacements are used to update the position instead:

$$ \boldsymbol{x}_p^{t+\Delta t} = \boldsymbol{x}_p^t + \boldsymbol{u}_p = \boldsymbol{x}_p^t + \mathbf{N}_p\Delta\boldsymbol{u} \tag{2.38}$$

and Eq. (2.33) is reused to compute the stresses at the end of the time step. Finally, the kinematics of the MPs are updated as

$$ \boldsymbol{a}_p^{t+\Delta t} = \mathbf{N}_p\boldsymbol{a}^{t+\Delta t} \tag{2.39}$$

and

$$ \boldsymbol{v}_p^{t+\Delta t} = \boldsymbol{v}_p^t + \frac{1}{2}\left(\boldsymbol{a}_p^t + \mathbf{N}_p\boldsymbol{a}^{t+\Delta t}\Delta t\right) \tag{2.40}$$

Once the MP variables are updated, the mesh is reset before the next time step is computed.

2.6. EXTENSIONS OF MPM

While MPM has been shown to be a useful engineering tool, the accuracy of standard MPM simulations has been shown to decrease when deformations increase (Bardenhagen and Kober, 2004; González Acosta et al., 2020). As the MPs move, they no longer occupy the ideal positions for numerical integration. Moreover, the MPs may even move into different elements. Due to the fact that the shape function gradients used to compute the nodal internal forces and MP stresses (Eqs. (2.28) and (2.33), respectively) are discontinuous at element boundaries, stress oscillations, i.e. fluctuation of the MP stress in space, occur when MPs move to a different element. These oscillations may then cause incorrect displacements, especially when more complex constitutive models are employed. As a result, MPM has often been constrained to be used with simple constitutive models.

In order to reduce the stress oscillations several improvements have recently been developed. Most of these improvements focus on creating shape function gradients which are continuous at element boundaries, while maintaining positive definite shape functions (as negative shape functions may lead to negative mass at the nodes). In GIMP, a support domain is assigned to each MP, see Figure 2.2b (Bardenhagen and Kober, 2004).This support domain can spread the influence of an MP over multiple elements. This is achieved by interpolating the standard FEM function over the support domain, which results in continuous shape function gradients even at element boundaries, as shown in Figure 2.3. The support domain has a fixed rectangular (2D) or cuboidal (3D) shape in the standard GIMP implementation, which was later renamed as unchanged/uniform GIMP (uGIMP) (Bardenhagen and Kober, 2004; Wallstedt and Guilkey, 2008). Several extensions of GIMP have been developed, which allow for various deformations of the support domain:

- Contiguous particle GIMP (cpGIMP) was proposed by Bardenhagen and Kober (2004) together with uGIMP. In cpGIMP, support domains can deform into any rectangular (2D) or cuboidal (3D) shape according to the normal deformation of the MP, i.e. the support domains are deformed by the normal strains (Bardenhagen and Kober, 2004; Wallstedt and Guilkey, 2008).

- Convected Particle Domain Interpolation (CPDI) allows the deformation of support domains into parallelograms (2D) or parallelepipeds (3D), i.e. the support domains are deformed by the normal strains, deviatoric strains and rotations (Sadeghirad et al., 2011). The shape functions are constructed as an interpolation of the standard FEM shape functions at the four corners of each particle domain, with the domains being described using the MP position and two vectors (Sadeghirad et al., 2011).

- CPDI2 extends the implementation of CPDI, and allows more flexibility over the shapes of the support domains by using quadrilaterals (Sadeghirad et al., 2013). The quadrilaterals are described by the corners of the support domains (Sadeghirad et al., 2011).

Hence several GIMP-based solutions focus on more accurately representing the MP domains, but for large strains the extreme distortions of the support domains can again

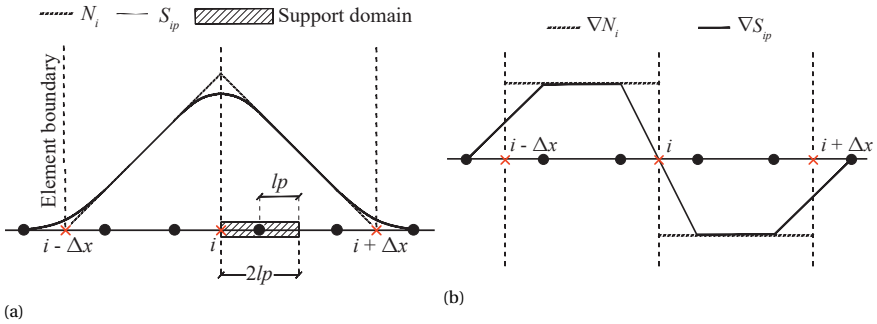

Figure 2.3: (a) GIMP shape function (S_{ip}) and regular FE shape function (N_i) for node i, and (b) GIMP shape function gradient (∇S_{ip}) and regular FE shape function gradient (∇N_i) for node i (Bardenhagen and Kober, 2004; González Acosta et al., 2020).

suffer from difficulties similar to mesh distortion. Standard GIMP can in these cases be more stable, since the support domains will not distort. Alternatively, at large strains a continuum approach, such as MPM, may no longer be appropriate for the entire domain. For example, separation of the material may be needed at large tensile or shear strains. In this thesis, the standard GIMP implementation with constant shape and size of the support domain (uGIMP) has been used. Whenever the acronym GIMP is used in the remainder of the thesis, it indicates uGIMP.

As an alternative, B-spline MPM (BSMPM) (Steffen et al., 2008) replaces the standard FEM shape functions with high-order B-spline functions, which are continuous across element boundaries, without tracking MP shapes. The high-order B-spline functions are positive definite such that negative mass contributions cannot occur, which would be a possibility were higher-order FEM shape functions to be used instead. Similar to B-spline MPM, the Dual Domain Material Point Method (DDMP) (Zhang et al., 2011) replaces the shape functions without requiring the tracking of the MP support domain. In DDMP, the influence domains used for the shape functions and the shape function gradients are separated. The influence domain for the shape function gradients is extended to multiple elements, such that the shape function gradients are continuous at element boundaries, while the influence domain for the shape function is a point, similar to standard MPM. DDMP can also be applied to unstructured meshes, which tends to be difficult with the other techniques. However, additional corrections are required for nodes at the boundary of a material. These nodes can receive a mismatched contribution from the shape function gradient compared to the shape function, which must be corrected. Finally, problems with discontinuous shape function gradients may be solved by mapping the properties which require shape function gradients, usually the stresses, to non-moving integration points using shape functions. After mapping, standard FEM integration can be performed. This strategy has been used by mapping properties to the center of cells (Liang et al., 2019) or the Gauss integration points (Al-Kafaji, 2013).

Besides stress oscillations, the movement of MPs can cause other issues. In implicit MPM, the integration of the stiffness matrix is affected by oscillations when MPs move within an element (González Acosta et al., 2020). These stiffness oscillations can be re-

duced with GIMP, but this complicates the element assembly procedure since multiple elements are connected together in the stiffness matrix due to the extended support domain. Local implicit GIMP shape functions can be used to disconnect the elements (Charlton et al., 2017), but this increases the stiffness oscillations (González Acosta et al., 2020). González Acosta et al. (2020) therefore used a double mapping (DM) technique to map the stiffness of the material to the Gauss integration points. This technique is effective with both standard MPM (called DM) as well as (implicit) GIMP shape functions (called DM-G). Movement of MPs within an element can also reduce the accuracy of the stress update (Eq. (2.33)). The stress update can be improved by using a patch recovery technique, which, similar to B-spline MPM, constructs continuous shape functions in multiple elements (González Acosta et al., 2020). The low order of the shape functions also increases the effect of volumetric locking. The locking can be reduced with FEM-like strategies such as the B-bar or F-bar methods, which have been developed for both MPM and GIMP (Coombs et al., 2018).

In this work, double mapping with standard GIMP shape functions (DM-G) has been used, except during the investigations of standard MPM boundary conditions in Chapter 3. This technique adequately reduces stress and stiffness oscillations, and has been shown to be capable of modelling slope failure with a shear strain softening constitutive model (González Acosta et al., 2020). To improve stability and reduce complexity of the numerical method, updating of the support domains of GIMP has not been used. Most material points experience limited strains during dyke slope failure, i.e. translations may be large, but strains are limited. The effect of the constant support domain size is therefore expected to be small.

2.7. CONCLUSION

The background of MPM has been presented. Even though MPM was not originally developed from FEM, MPM can be seen as a logical extension of FEM for large deformations, as it can be built from the FE formulation. Several integration schemes have been presented. The implicit scheme is used within this work as significantly larger time steps can be used, and the total computation cost is expected to be lower. Standard MPM can be implemented as a straightforward extension of FEM where the Gauss points move. However, to increase the accuracy of MPM extensions are required, of which a summary has been provided. Many of these extensions change the shape functions according to an influence domain of the material point in order to solve stress oscillations associated with the movement of the material points.

REFERENCES

Al-Kafaji, I. K. J. (2013). *Formulation of dynamic MPM for geo problems* (Doctoral dissertation). University of Struttgart, Germany.

Bardenhagen, S. G., & Kober, E. M. (2004). The generalized interpolation material point method. *CMES - Computer Modeling in Engineering and Sciences*, *5*(6), 477–496. https://doi.org/10.3970/cmes.2004.005.477

Bathe, K. J. (2014). *Finite Element Procedures* (2nd ed.). Prentice Hall.

Charlton, T. J., Coombs, W. M., & Augarde, C. E. (2017). Igimp: An implicit generalised interpolation material point method for large deformations. *Computers & Structures, 190*, 108–125. https://doi.org/10.1016/j.compstruc.2017.05.004

Coombs, W. M., Charlton, T. J., Cortis, M., & Augarde, C. E. (2018). Overcoming volumetric locking in material point methods. *Computer Methods in Applied Mechanics and Engineering, 333*, 1–21. https://doi.org/10.1016/j.cma.2018.01.010

González Acosta, J. L., Vardon, P. J., Remmerswaal, G., & Hicks, M. A. (2020). An investigation of stress inaccuracies and proposed solution in the material point method. *Computational Mechanics, 65*, 555–581. https://doi.org/10.1007/s00466-019-01783-3

Liang, Y., Zhang, X., & Liu, Y. (2019). An efficient staggered grid material point method. *Computer Methods in Applied Mechanics and Engineering, 352*, 85–109. https://doi.org/10.1016/j.cma.2019.04.024

Newmark, N. M. (1959). A method of computation for structural dynamics. *Journal of the Engineering Mechanics Division, 85*(3), 67–94. https://doi.org/10.1061/JMCEA3.0000098

Sadeghirad, A., Brannon, R. M., & Burghardt, J. (2011). A convected particle domain interpolation technique to extend applicability of the material point method for problems involving massive deformations. *International Journal for Numerical Methods in Engineering, 86*(12), 1435–1456. https://doi.org/10.1002/nme.3110

Sadeghirad, A., Brannon, R., & Guilkey, J. (2013). Second-order convected particle domain interpolation (CPDI2) with enrichment for weak discontinuities at material interfaces. *International Journal for Numerical Methods in Engineering, 95*(11), 928–952. https://doi.org/10.1002/nme.4526

Smith, I. M., Griffiths, D. V., & Margetts, L. (2014). *Programming the Finite Element Method* (5th ed.). John Wiley & Sons.

Steffen, M., Kirby, R. M., & Berzins, M. (2008). Analysis and reduction of quadrature errors in the material point method (MPM). *International Journal for Numerical Methods in Engineering, 76*(6), 922–948. https://doi.org/10.1002/nme.2360

Sulsky, D., Chen, Z., & Schreyer, H. L. (1994). A particle method for history-dependent materials. *Computer Methods in Applied Mechanics and Engineering, 118*(1-2), 179–196. https://doi.org/10.1016/0045-7825(94)90112-0

Wallstedt, P., & Guilkey, J. (2008). An evaluation of explicit time integration schemes for use with the generalized interpolation material point method. *Journal of Computational Physics, 227*(22), 9628–9642. https://doi.org/10.1016/j.jcp.2008.07.019

Wang, B., Vardon, P. J., Hicks, M. A., & Chen, Z. (2016). Development of an implicit material point method for geotechnical applications. *Computers and Geotechnics, 71*, 159–167. https://doi.org/10.1016/j.compgeo.2015.08.008

Zhang, D. Z., Ma, X., & Giguere, P. T. (2011). Material point method enhanced by modified gradient of shape function. *Journal of Computational Physics, 230*(16), 6379–6398. https://doi.org/10.1016/j.jcp.2011.04.032

Zienkiewicz, O., Taylor, R., & Fox, D. (2014). *The Finite Element Method for Solid and Structural Mechanics* (7th ed.). Butterworth-Heinemann. https://doi.org/10.1016/B978-1-85617-634-7.00002-8

3

NEUMANN BOUNDARY CONDITIONS FOR MPM AND GIMP

As the Material Point Method (MPM) uses both a mesh and a point discretisation scheme, the application of boundary conditions is difficult, limiting the flexibility of the method. While many boundary condition options have been proposed in the literature, the accuracy of Neumann boundary condition options has not yet been studied. Four options have here been evaluated for 1D and 2D benchmarks, although none of the options were found to be both accurate and generally applicable in MPM. However, for the Generalized Interpolation Material Point method (GIMP) the application of surface tractions on support domain boundaries or on a detected surface are accurate options. The two new methods provide accurate surface tractions for a submerged slope example when compared to the application of tractions at surface material points, a method regularly used in literature.

This chapter is based on the following paper (currently under review): Remmerswaal, G., Vardon, P. J., & Hicks, M. A. (2022). Inhomogeneous Neumann boundary conditions for MPM and GIMP (submitted for journal publication).

3.1. INTRODUCTION

Due to decades of development, the Finite Element Method (FEM) has become an accurate and flexible tool. The flexibility of the mesh to discretise arbitrary geometries and refine locations of interest, as well as the large assortment of (accurate) boundary conditions and constitutive models, have made the method applicable for a wide variety of problems (Bathe, 2014). In other words, the method is generally applicable. The Material Point Method (MPM) on the other hand is (yet) far from being generally applicable. This is partly caused by the previously mentioned stress inaccuracies, for which many improvements have been developed in the recent years.

A remaining key challenge for MPM, which is starting to gain attention, is the imposition of boundary conditions (BCs), especially on complex or moving geometries. Dirichlet BCs (fixed primary variable) and Neumann BCs (normal derivative of the primary variable or force in a mechanical governing equation) are most commonly used to solve the governing equations on the background grid. In FEM, the edge of the elements closely resembles the domain edge Γ and the element nodes typically lie on the domain edge, see Figure 2.1b. Therefore, boundary conditions can be easily included. In MPM, since the material, and thus the material boundary, has been decoupled from the grid neither the MPs nor the background grid align directly with the domain boundary, see Figure 2.2a. It is therefore not immediately obvious where surface tractions and point loads should be applied, nor where displacement conditions should be enforced (Cortis et al., 2018). Compared to meshless methods (MMs), defining BCs in MPM can be considered easier due to the presence of a background grid, because techniques designed for FEM may be applied. For example, FEM BCs can be applied directly when a problem is setup such that a boundary coincides (permanently) with an edge of the background grid. However, in order to make MPM generally applicable, non-conforming BCs, i.e. BCs decoupled from the grid, must be developed. Surface tractions on a moving surface provide an additional complication, as the applied loads may need to be updated when the geometry evolves under large deformations.

To further complicate boundary conditions in MPM, several of the techniques used to address the aforementioned stress oscillations alter the point and/or mesh discretisation. For example, in GIMP, an MP is no longer discretised as a single point, but is assigned a rectangular area instead, see Figure 2.2b, with a size defined as $2lp_x \times 2lp_y$. While, in the initial position, the rectangular support domains of the MPs do not overlap, the support domains may overlap after movement of the MPs. The changed discretisation will impact the application of the boundary conditions. Here, BCs in MPM and GIMP are studied, to investigate the effects of different discretisations on the BCs.

While several strategies for non-conforming BCs have been used during the development of MPM, of which a review is presented in Section 3.2, the application of BCs is not yet fully understood. Therefore, the accuracy of four Neumann BC methods for MPM and GIMP, which are further explained in Section 3.3, are tested for one and two dimensional problems in Sections 3.4 and 3.5, respectively. Sections 3.4 and 3.5 highlight the inconsistencies between Neumann BC methods and the computation of the internal force. To use consistent methods in practice, algorithms are developed for general applicability (Section 3.6). The algorithms are then tested on a submerged slope failure case study (Section 3.7).

3.2. BACKGROUND ON BOUNDARY CONDITIONS IN MPM

A straightforward strategy is to apply BCs on 'surface' MPs, i.e. the MPs closest to the material boundary. Dirichlet conditions can be enforced on surface MPs by fixing the primary variables of MPs (Moormann and Hamad, 2015; Wang et al., 2018). Neumann conditions may also be applied as point loads at surface MPs, by integrating the loads to the background grid (Chen et al., 2002; Fern et al., 2019; Hu and Chen, 2003; Martinelli et al., 2017). However, since MPs are, by definition, not at the material boundary, the exact location is not correct and therefore can cause inaccuracies and discretisation dependency of the solution. Moreover, for large distortions (which MPM is designed for), the surface MPs may change over time and must therefore be identified, which is a non-trivial task.

Since the governing equations are solved at the nodes, another solution could be to enforce the BCs directly at 'surface' nodes, i.e. those nodes which separate active from inactive elements. This presented reasonable results for a rainfall boundary condition in explicit MPM (Martinelli et al., 2021), even though the BC did not coincide exactly with the material boundary. The results can be further improved when the boundary is forced to be at the nodes; boundaries with an irregular shape can be applied on the nodes of an irregular grid (Tjung, 2020; Tjung et al., 2020; Wang et al., 2005), while a moving mesh can be employed for BCs with known displacements (Beuth, 2012; Fern et al., 2019; Martinelli and Galavi, 2021; Phuong et al., 2016; Wang et al., 2021). However, while these methods show good results for a subset of problems, the solutions are not generally applicable. Moreover, the techniques are often developed for structured grids, and versions for unstructured grids require new developments (de Koster et al., 2021).

MPM boundary conditions may benefit from developments in MMs, which do not benefit from an FEM mesh. In MMs, FEM techniques, such as Lagrange multipliers, the penalty method and Nitsche's method can still be employed with adjustments (Fernández-Méndez and Huerta, 2004). Moreover, new techniques have been developed, for example boundary FEM grids coupled to meshless points (Huerta and Fernández-Méndez, 2000; Mast et al., 2011), and ghost points to enforce BCs or track the boundary (Colagrossi and Landrini, 2003; Federico et al., 2012; Mao et al., 2016).

Recent studies have looked at applying BCs within FEM elements instead of on element boundaries. Dirichlet BCs can be included into the system of equations of nodes surrounding the material boundary using the Implicit Boundary Method (IBM) (Bing et al., 2019; Cortis et al., 2018; Kumar et al., 2008). In IBM, the constraints ($\boldsymbol{u} = \boldsymbol{u}^d$ and $\boldsymbol{u} = 0$ at Γ_d) are enforced using so-called Dirichlet functions. These functions enforce the constraint over a narrow band along Γ_d, while the constraint only indirectly affects the rest of the FEM mesh via the system of equations. While in IBM the BCs are included in the equations of elements surrounding the boundary, in the Shifted Boundary Method (SBM) the BCs are mapped onto the elements enclosed by the boundary (Liu and Sun, 2019; Main and Scovazzi, 2018). In SBM all elements intersecting or outside the boundary are removed from the mesh, and a surrogate boundary is then created at the boundary of the remaining mesh. A distance function is employed to map from the real to the surrogate boundary, such that the BC can be included using Nitche's method. Similar to IBM and SBM, Neumann BCs can be integrated to surrounding nodes using Gauss integration along the boundary (Bing et al., 2019; Remmerswaal, 2017) or mapped

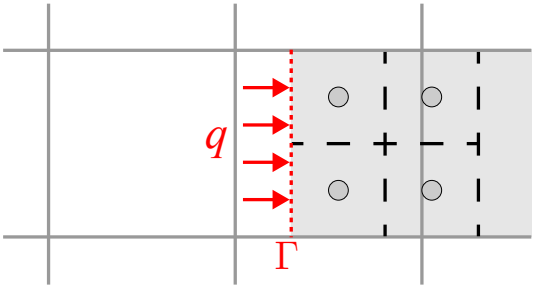

Figure 3.1: Example of surface traction q applied on the surface of a material Γ (red dotted line). The material is discretised into MPs (circles) with their respective support domains (black dashed lines) located within a background mesh (grey solid lines).

to the surrogate boundary (Main and Scovazzi, 2018). These FEM-like methods require the location of the surface, which must be predefined by the user or can be detected based on the MP location and properties (Remmerswaal, 2017).

Besides Dirichlet and Neumann BCs, inflow and outflow BCs, i.e. introduction and removal of material, respectively, can be required within MPM. These flux-based conditions are especially useful to reduce the computational cost in (pore-)fluid mechanics. For example, to model a steady flow through a boundary in space, a velocity (Dirichlet) condition must be enforced at the boundary. However, the MPs would flow away from the boundary, leaving the elements on which the condition is enforced empty, preventing the steady flow through the boundary. Therefore, new material (points) must be introduced through the boundary (Zhao et al., 2019). Additional elements may be used to introduce the new MPs, and the Dirichlet BC should also be enforced on the new MPs to create a steady flow. To prevent a build up of MPs at the end of the computational domain, an outflow condition can be used, i.e. MPs may be removed when they enter specific elements (Zhao et al., 2019). To ensure a specific solution, a Neumann condition can be enforced at the outflow elements.

3.3. NEUMANN BOUNDARY CONDITION METHODS IN MPM

Four possible methods to apply Neumann BCs on an MP discretisation are outlined below and investigated in Sections 3.4 and 3.5. The methods are explored using the example configuration of Figure 3.1. In this example, the MPs (indicated by black circles) are evenly spaced and translated horizontally with respect to the background grid. For simplicity, the MPs and the boundary Γ are aligned with the grid in the vertical direction, but this is not necessary. Γ (as indicated by the red dotted line in Figure 3.1) is neither located at the edge of a grid cell nor at an MP. The traction is indicated by $\boldsymbol{q}$. MP domains are also shown via the black dashed lines, but these are only defined in methods with particle domains such as GIMP.

3.3.1. EQUIVALENT POINT LOADS APPLIED ON SURFACE MPS

To apply loads on surface MPs, as shown in Figure 3.2a, Γ is split into segments Γ_p, indicated by Γ_1 and Γ_2 in Figure 3.2a, associated with the closest surface MP. $\boldsymbol{q}$ is integrated along Γ_p into an equivalent point load which acts at MP p:

$$\boldsymbol{F}_p = \int_{\Gamma_p} \boldsymbol{q} \, \mathrm{d}\Gamma_p \tag{3.1}$$

In Figure 3.2a Γ_1 and Γ_2 are integrated into MP point loads F_1 and F_2, respectively. The point loads are then integrated to the nodes using shape functions (similar to Eq. (2.10)) by summing over all boundary MPs:

$$\boldsymbol{F}_{\mathrm{MP}} \coloneqq \sum_p \mathbf{N}_p^{\mathrm{T}} \boldsymbol{F}_p \tag{3.2}$$

where $\boldsymbol{F}_{\mathrm{MP}}$ are the nodal external loads obtained from the point loads applied at the boundary MPs. This method is convenient for externally applied loads which move with the material, as once defined $\boldsymbol{F}_p$ does not need to be recalculated - this can even be done in a pre-processing stage. It is seen that, in contrast to FEM, all nodes of the element containing the BC have forces associated with the BC, shown as F_i to F_l in Figure 3.2a.

3.3.2. BOUNDARY MOVED TO THE SURFACE NODES

With the second method, the boundary condition is applied on the boundary Γ_m separating the active elements from the inactive elements, see Figure 3.2b. In MPM, an element is active when it contains at least one MP. In GIMP, an element is active when it overlaps with a part of the support domain of at least one MP. Eq. (2.10) is then used to integrate the traction to the surface nodes:

$$\boldsymbol{F}_{\mathrm{Nodes}} \coloneqq \int_{\Gamma_m} \mathbf{N}^{\mathrm{T}} \boldsymbol{q} \, \mathrm{d}\Gamma_m \tag{3.3}$$

where $\boldsymbol{F}_{\mathrm{Nodes}}$ are the external nodal loads computed from the surface nodes. This method is most similar to FEM, but also moves the boundary away from its intended location unless the material boundary aligns with the mesh. It is straightforward to apply if the load is fixed in space and not dependent on the movement of the material in the domain, but it requires a substantial housekeeping algorithm to identify the correct location to apply the boundary condition if it moves with the material.

3.3.3. BOUNDARY CONDITION APPLIED EXACTLY

The third method (see Figure 3.2c) integrates $\boldsymbol{q}$ directly from Γ. Standard FEM integration can be used within elements as well, such that

$$\boldsymbol{F}_{\mathrm{Surface}} \coloneqq \int_{\Gamma} \mathbf{N}^{\mathrm{T}} \boldsymbol{q} \, \mathrm{d}\Gamma \tag{3.4}$$

where $\boldsymbol{F}_{\mathrm{Surface}}$ is the external nodal load integrated directly from Γ. This integration becomes more complicated in realistic scenarios where the shape of Γ may be complex.

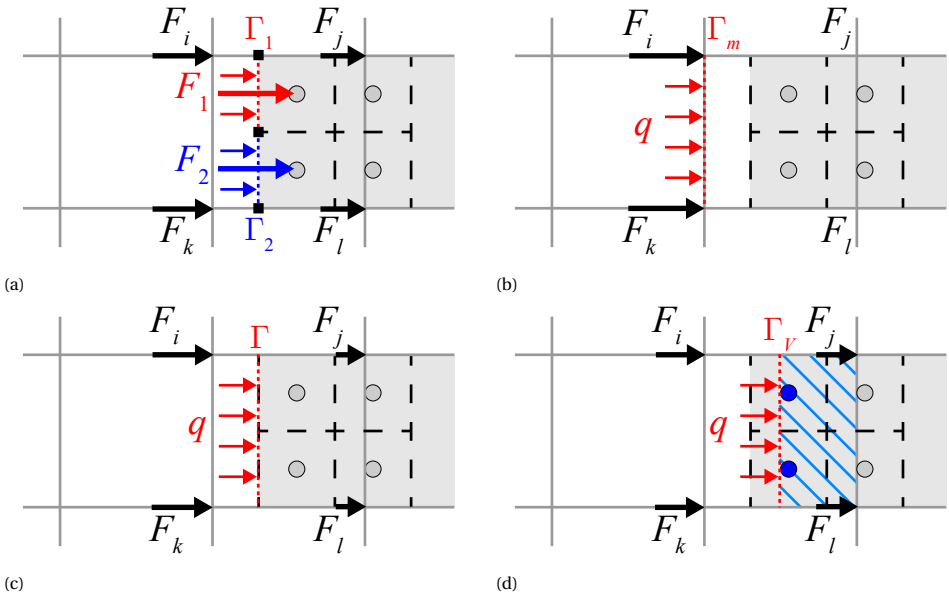

Figure 3.2: Four Neumann boundary condition methods to transfer $\boldsymbol{q}$ to $\boldsymbol{F}_{\text{ext}}$: (a) application on surface MPs as point loads, obtained from integration over two surface segments; (b) application on surface nodes; (c) direct integration from (detected) surface; (d) application on a surface proportional to the volume of the MPs in the boundary element (blue hatched volume is equal to the volume of the blue MPs)

In these cases, B-splines or Composite Bezier Curves may be used to represent Γ, and Gauss integration along Γ can be used to evaluate Eq. (3.4), see Bing et al. (2019) and Remmerswaal (2017) for further details. This method (as in the first method) results in nodal forces on all of the nodes in the element, and requires the identification of the exact boundary location. For the case when Γ is parallel to the GIMP domain orientation, this method is equivalent to applying loads on the GIMP support domain.

3.3.4. BOUNDARY CONDITION MOVED PROPORTIONALLY TO VOLUME OF MPS IN BACKGROUND GRID ELEMENTS

The fourth method (Figure 3.2d) evaluates the volume of the material points within each cell. A boundary surface Γ_V is placed in partially filled cells, such that the volume enclosed by the surface is equal to the volume of MPs in each cell (the implementation is explained for standard MPM and GIMP in the remainder of the paragraph). For example, the surface is placed in the middle of the surface element in Figure 3.2d, since the element has only two MPs within it (50% of the original four). $\boldsymbol{q}$ is then integrated along Γ_V to obtain $\boldsymbol{F}_{\text{Volume}}$, i.e. the external nodal loads computed from Γ_V:

$$\boldsymbol{F}_{\text{Volume}} \coloneqq \int_{\Gamma_V} \mathbf{N}^{\mathrm{T}} \boldsymbol{q} \, \mathrm{d}\Gamma_V \tag{3.5}$$

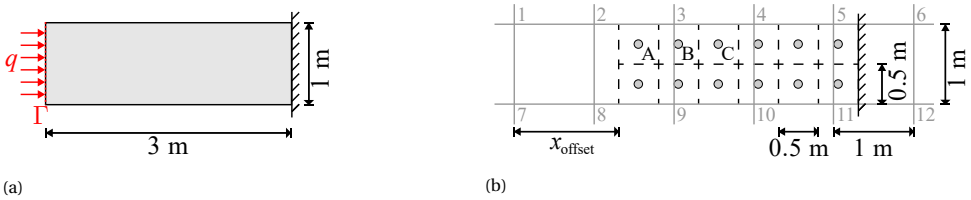

Figure 3.3: (a) A 3 m by 1 m bar fixed at one end and compressed from the other end by a surface traction q; (b) the bar discretised into MPs (dots), representing a square support domain (dashed lines), and the computational domain discretised as a background grid constructed from square 1 m elements (solid grey lines), in which the start of the grid is located at a distance x_{offset} from the surface Γ.

This method is difficult to practically implement for arrangements where the MPs are not well aligned with the background grid. In GIMP, the volume of MPs is distributed according to the support domain of the MPs. Therefore, Γ_V coincides with the boundary of the support domain and, for clarity, the name $\boldsymbol{F}_{\text{Volume}}$ is changed to $\boldsymbol{F}_{\text{GIMP}}$. In other words, $\boldsymbol{F}_{\text{GIMP}}$ is the nodal force when a traction is applied to the boundary of the support domain in GIMP, and is equivalent to $\boldsymbol{F}_{\text{Surface}}$ when Γ is parallel to the GIMP domain orientation.

3.4. APPLICATION IN ONE DIMENSION

A simple benchmark is presented to demonstrate the performance and characteristics of the different BC application methods, and to indicate the inconsistencies of the BC methods with respect to the internal force calculation. A mismatch between $\boldsymbol{F}_{\text{ext}}$ and $\boldsymbol{F}_{\text{int}}$ can cause (additional) stress oscillations which have been characteristic of many MPM implementations. A 1D problem is solved using a 2D plane strain discretisation and background grid. An elastic bar, presented in Figure 3.3, is fixed at one end and loaded with a surface traction $q = 1$ kPa at the other end. The bar has a Poisson's ratio of 0. The MPs are distributed equally within the bar, with a distance of 0.5 m between adjacent points. The start of the background grid is placed at a distance x_{offset} from the surface Γ, and consists of 1 m square elements. The MPs are fixed in place, i.e. no displacements are computed. The initial horizontal stress in all MPs is initialised as q, such that the bar is in equilibrium. Therefore, for a consistent solution, $\boldsymbol{F}_{\text{int}}$ and $\boldsymbol{F}_{\text{ext}}$ should be equal at each node for every position of the bar in the background grid, i.e. for all values of x_{offset}.

Figures 3.4a - 3.4c present $\boldsymbol{F}_{\text{int}}$ and $\boldsymbol{F}_{\text{ext}}$ at the first three nodes, calculated using standard MPM, for various distances x_{offset}. Due to the constant shape function gradients within an element (and the constant stress), $\boldsymbol{F}_{\text{int}}$ remains constant until MPs cross element boundaries, after which a jumps occurs.

All methods show a qualitatively similar behaviour, i.e. as the boundary moves away from a node $\boldsymbol{F}_{\text{ext}}$ decreases, whereas $\boldsymbol{F}_{\text{ext}}$ increases as the boundary moves closer to a node. This behaviour is similar to the behaviour of $\boldsymbol{F}_{\text{int}}$, and therefore explains the qualitative success of boundary conditions in past MPM research.

However, by looking at the results in more detail some differences are observed. $\boldsymbol{F}_{\text{MP}}$ is inconsistent with $\boldsymbol{F}_{\text{int}}$ for most x_{offset}, since too much load is transferred to the inner

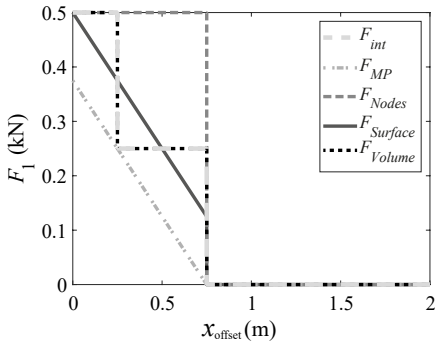

(a) Node 1 - MPM

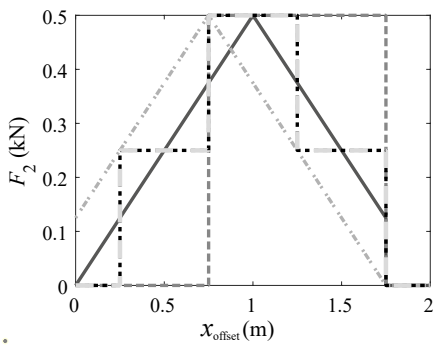

(b) Node 2 - MPM

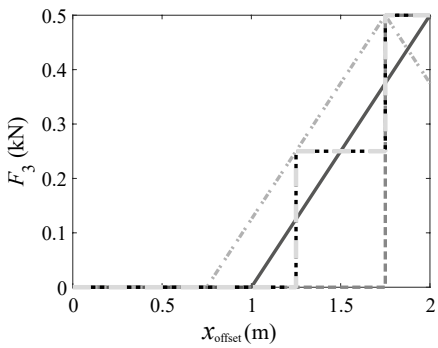

(c) Node 3 - MPM

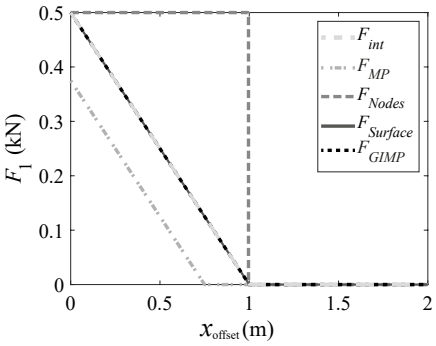

(d) Node 1 - GIMP

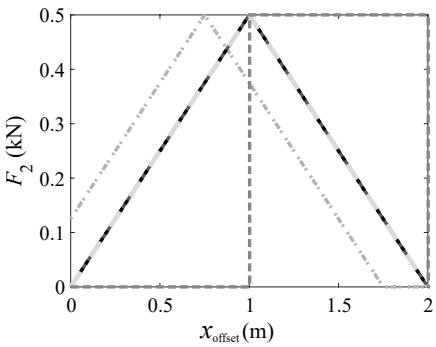

(e) Node 2 - GIMP

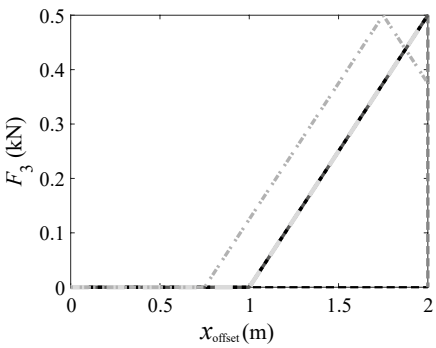

(f) Node 3 - GIMP

Figure 3.4: Internal force for standard MPM (a-c) and GIMP (d-f) compared with external force computed by four methods for (a and d) node 1, (b and e) node 2, and (c and f) node 3 of Figure 3.3. Note the change from F_{Volume} to F_{GIMP} in the legend of d-f. Due to the symmetry of the problem presented in of Figure 3.3, the forces at node 1, node 2 and node 3 are equivalent to node 7, node 8 and node 9, respectively.

nodes. In other words, load is applied inside the material instead of on the material surface. $\boldsymbol{F}_{\text{Nodes}}$ is consistent when the boundary element contains 4 MPs, but overestimates $\boldsymbol{F}_{\text{ext}}$ compared to $\boldsymbol{F}_{\text{int}}$ on the surface nodes after MPs cross element boundaries. $\boldsymbol{F}_{\text{Nodes}}$ may present consistent results for small deformation problems, which are often used during code development. $\boldsymbol{F}_{\text{Surface}}$ matches $\boldsymbol{F}_{int}$ when Γ coincides with the background grid or when Γ lies exactly in the middle of the boundary element. However, $\boldsymbol{F}_{\text{Surface}}$ and $\boldsymbol{F}_{\text{MP}}$ change linearly with x_{offset}, while $\boldsymbol{F}_{\text{int}}$ remains constant due to the shape function gradients. Due to the mismatch in the linear versus step-wise $\boldsymbol{F}_{\text{ext}}$ and $\boldsymbol{F}_{\text{int}}$, the application of the boundary condition in this manner will cause stress oscillations which have been characteristic of many MPM implementations. Finally, $\boldsymbol{F}_{\text{Volume}}$ is consistent with $\boldsymbol{F}_{\text{int}}$. The position of the surface in this method is dependent on the volume/number of MPs in the outermost active element, and jumps to a new position whenever MPs leave this element. The surface corresponds with the end of the material point discretisation, and therefore distributes $\boldsymbol{F}_{\text{ext}}$ in the same manner as the internal load, thereby avoiding stress oscillations.

Note that Neumann boundary conditions are only theoretically correct when applied on the exact material surface (i.e. using $\boldsymbol{F}_{\text{Surface}}$). However, the discretisation of MPM causes an incorrect internal force calculation near the boundary, and $\boldsymbol{F}_{\text{Volume}}$ is therefore a more consistent BC method for MPM. By increasing the number of material points or by increasing the number of background grid elements, the difference between $\boldsymbol{F}_{\text{Volume}}$ and $\boldsymbol{F}_{\text{Surface}}$ will decrease.

Figures 3.4d-3.4f repeat the analysis using GIMP instead of MPM. $\boldsymbol{F}_{\text{int}}$ has changed due to the GIMP shape function gradients (see Figure 2.3), which influence multiple elements and 'distribute' the MP stresses according to their support domains. Similar to $\boldsymbol{F}_{\text{Volume}}$ for MPM, $\boldsymbol{F}_{\text{GIMP}}$ computes an $\boldsymbol{F}_{\text{ext}}$ consistent with $\boldsymbol{F}_{\text{int}}$. Moreover, due to the simple problem geometry, the boundary of the support domain of GIMP coincides with Γ such that $\boldsymbol{F}_{\text{GIMP}} = \boldsymbol{F}_{\text{Surface}}$. $\boldsymbol{F}_{\text{Nodes}}$ is less consistent in GIMP compared to MPM, since the internal force changes linearly with x_{offset}, while $\boldsymbol{F}_{\text{MP}}$ is more consistent due to the linear change. Note that standard MPM shape functions are used to integrate or transfer loads to the nodes. This agrees with the concept of GIMP, since the GIMP shape function for a surface should be created from a 'support domain' with zero width, which returns the standard FEM shape functions.

This analysis indicates the importance of developing a (Neumann) BC method which agrees with the discretisation of the material and the adopted shape functions, i.e. the BC method should be consistent with the internal force calculation. Moreover, it shows another advantage of GIMP compared to MPM, since the material surface coincides with the optimal position for BCs in one dimension. Therefore, GIMP is the focus for the remainder of this chapter.

3.5. APPLICATION IN TWO DIMENSIONS

A bar with an inclined surface (angle θ) is used to analyse the effect of a surface unaligned with the background grid, see Figure 3.5a. A traction $\boldsymbol{q}$ is applied normal to the bar's surfaces, i.e. normal to the inclined, horizontal and vertical surfaces. The bar is discretised using MPs with a 0.5 m square support domain, which are aligned with the background grid in the vertical direction, and placed in the horizontal direction such

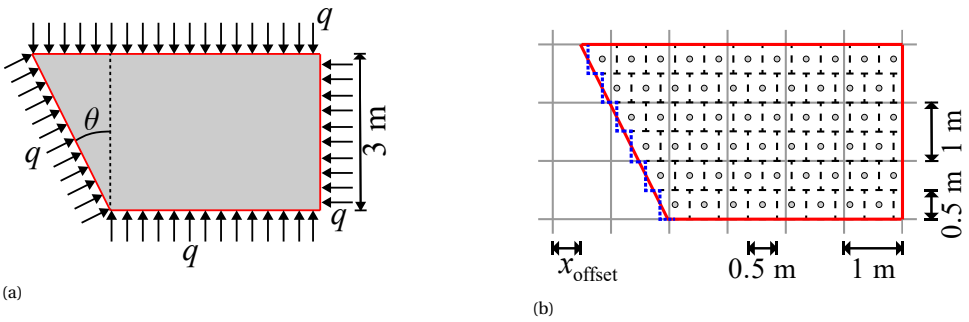

Figure 3.5: (a) A bar with a surface inclined at an angle θ, compressed from all sides by a surface traction q. (b) The bar is discretised into MPs (grey filled circles) with a square support domain (dashed lines), and a background grid (solid lines) constructed from 1 m square elements which is offset by a distance x_{offset} with respect to the tip of the bar. The surfaces used to compute $\boldsymbol{F}_{\text{Surface}}$ and $\boldsymbol{F}_{\text{GIMP}}$ are highlighted by the solid red line and dotted blue line, respectively.

that the support domains align with the sloped surface (see Figure 3.5b). The slope cuts the middle of the left edge of the support domains as shown in Figure 3.5b), for all angles θ. The background grid is offset by a distance x_{offset} from the tip of the bar, and consists of 1 m square elements.

The analytical solution for the internal stress at all positions in the bar is q in both the vertical and horizontal directions, i.e. the bar is in equilibrium with the applied external force. Once again, the initial stresses are set to this equilibrium condition. The calculated internal forces at the boundary nodes are compared with the external forces computed using the methods proposed in the previous sections, and should be equal for a consistent BC method. The normalised differences in the horizontal and vertical forces, E_{F_x} and E_{F_y}, respectively, are defined as:

$$E_{F_x} = \frac{\sum_i |F^{ext}_{x,i} - F^{int}_{x,i}|}{3q} \tag{3.6}$$

$$E_{F_y} = \frac{\sum_i |F^{ext}_{y,i} - F^{int}_{y,i}|}{3q\tan(\theta)} \tag{3.7}$$

where $F^{ext}_{j,i}$ and $F^{int}_{j,i}$ are the external and internal forces of node i in direction j, respectively. E_{F_x} and E_{F_y} express the difference between $\boldsymbol{F}_{\text{ext}}$ and $\boldsymbol{F}_{\text{int}}$ summed over all nodes, decomposed in the horizontal and vertical directions. E_{F_x} and E_{F_y} are normalised with respect to the theoretical external force acting along the sloped surface in the horizontal and vertical directions, respectively. Due to the geometry of the problem, the theoretical horizontal external force is independent of the slope angle, while the theoretical vertical external force depends on the slope angle. The denominators normalise the differences for the slope angle.

The computed differences of the four methods for $\tan(\theta) = 0.5$, i.e. the slope shown in Figure 3.5b, are shown in Figure 3.6. The figure presents the normalised differences

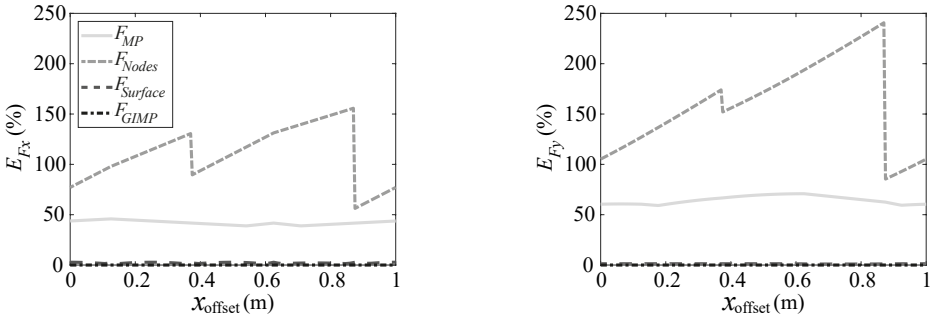

(a) (b)

Figure 3.6: Error in the total force computed for an inclined bar with $\tan(\theta) = 0.5$ with various boundary condition methods, (a) E_{Fx}, (b) E_{Fy}.

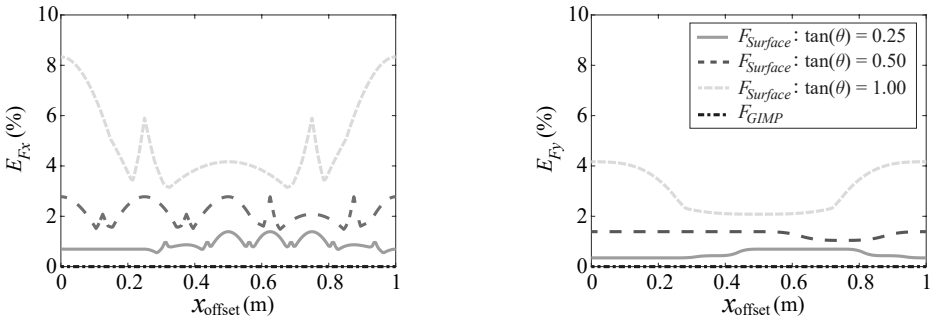

(a) (b)

Figure 3.7: Error in the total force computed for an inclined bar for various slope angles using $\boldsymbol{F}_{\text{Surface}}$ and $\boldsymbol{F}_{\text{GIMP}}$, (a) E_{Fx}, (b) E_{Fy}

E_{F_x} and E_{F_y} for different offsets (x_{offset}) of the grid. To clarify, $\boldsymbol{F}_{\text{Surface}}$ is computed using the sloped surface of the actual bar, while $\boldsymbol{F}_{\text{GIMP}}$ is computed by the boundary of the GIMP domains constructed from vertical and horizontal segments (see Figure 3.5b). For clarity, Figure 3.6 and Figure 3.7 are limited between $0\text{ m} < x_{\text{offset}} < 1\text{ m}$, i.e. one grid cell, since E_{F_x} and E_{F_y} are periodic with respect to the offset of the grid with a period of one grid cell. This period is independent of the slope angle.

Similar to the 1D case, $\boldsymbol{F}_{\text{Nodes}}$ presents the largest inconsistencies (oscillating around a normalised total difference of 100%), due to the fact that loads are applied at large distances from the domain (in some locations) for all values of x_{offset}. Whereas $\boldsymbol{F}_{\text{Nodes}}$ applies loads too far outside of the material, $\boldsymbol{F}_{\text{MP}}$ instead applies loads too far into the material. However, the differences for $\boldsymbol{F}_{\text{MP}}$ are smaller then the differences for $\boldsymbol{F}_{\text{Nodes}}$ and more or less constant: i.e. differences of approximately 50% in the x- and y-directions. The two methods which demonstrated an exact application of the BC in one dimension, $\boldsymbol{F}_{\text{Surface}}$ and $\boldsymbol{F}_{\text{GIMP}}$, also perform well in two dimensions. $\boldsymbol{F}_{\text{Surface}}$ has an average difference of 2.1% and 1.3 % in the x- and y-directions respectively, while $\boldsymbol{F}_{\text{GIMP}}$ is consistent.

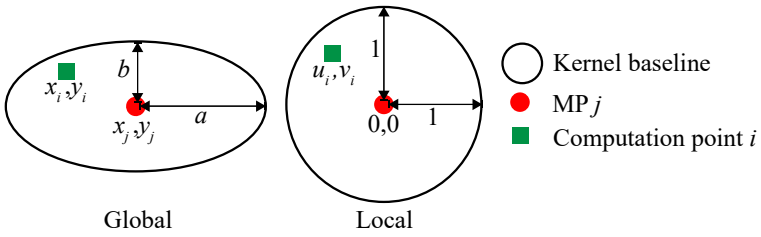

Figure 3.8: Conversion of a global elliptical kernel baseline to a local circular kernel baseline around MP j. A point for the computation of the kernel function is indicatively shown in the global and local coordinate systems.

Figure 3.7 further investigates the difference between $\boldsymbol{F}_{\text{Surface}}$ and $\boldsymbol{F}_{\text{GIMP}}$, for various slope angles θ. $\boldsymbol{F}_{\text{GIMP}}$ is an error free solution for all slope angles, while for $\boldsymbol{F}_{\text{Surface}}$ the error grows with a larger slope angle (it would then decrease with further increase in slope angle above 45°). The larger errors are caused by a growing difference between the actual surface and the discretisation of GIMP. Moreover, as the slope angle is closer to 45°, the surface is more often partially located in inactive elements, reducing the applied total load and increasing the error. Note that, even though the error of $\boldsymbol{F}_{\text{Surface}}$ grows with the slope angle (up to $\theta = 45°$), the error is still significantly smaller than for $\boldsymbol{F}_{\text{MP}}$ and $\boldsymbol{F}_{\text{Nodes}}$.

3.6. BOUNDARY DETECTION

Sections 3.4 and 3.5 show that, in GIMP, $\boldsymbol{F}_{\text{Surface}}$ and $\boldsymbol{F}_{\text{GIMP}}$ are (almost) consistent with the internal force. Sections 3.4 and 3.5 involved a fixed geometry, where the material surface could be pre-defined. However, in an analysis where MPs move with respect to the background grid, and also with respect to each other, the material surface should be detected automatically. Algorithms are therefore required to construct the boundary required for the consistent method. An algorithm for $\boldsymbol{F}_{\text{Volume}}$ in MPM has not (yet) been found. This chapter instead presents two types of boundary detection methods for $\boldsymbol{F}_{\text{Surface}}$ and $\boldsymbol{F}_{\text{GIMP}}$, to be used in GIMP. Remmerswaal (2017) investigated various approaches to construct the material surface for $\boldsymbol{F}_{\text{Surface}}$ in MPM, and showed that the Proximity Field Method (PFM), which constructs linear segments within grid cells based on the level set method, performed well. A brief explanation of PFM is provided. In addition, this chapter expands a contour algorithm for iso-rectangles to construct the surface for $\boldsymbol{F}_{\text{GIMP}}$ (Prusinkiewicz and Raghavan, 1985).

3.6.1. PROXIMITY FIELD METHOD

The Proximity Field Method (PFM) (Remmerswaal, 2017) is based on the level set method, where the boundary location is defined as the (zero) level set of an auxiliary field (Sethian, 1996) and can be used to compute $\boldsymbol{F}_{\text{Surface}}$. Epanechnikov kernel functions are used to compute the proximity, i.e. the distance, to nearby MPs. In other words, the kernel function represents the influence domain of the MP. A local coordinate system

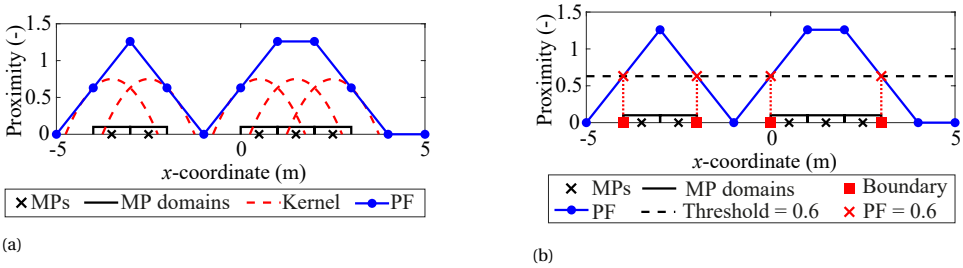

Figure 3.9: (a) 1D example of constructing a PF using kernel functions; (b) 1D example of boundary detection by comparing the PF with a threshold.

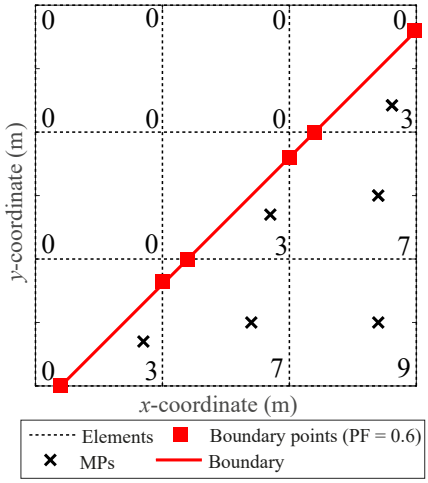

Figure 3.10: Computation of boundary points from a proximity field in two dimensions. Proximity field values displayed at the nodes. Boundary constructed by connecting the boundary points with linear segments.

is used for the kernel function (see Figure 3.8), i.e.

$$K_{i,j} = C_j(1 - \boldsymbol{u}_{i,j}^{\mathrm{T}}\boldsymbol{u}_{i,j}) \tag{3.8}$$

where $K_{i,j}$ is the kernel function of the j th MP evaluated at point i, $\boldsymbol{u}_{i,j}$ is a distance in local coordinates and C_j is a constant used to control the magnitude of the kernel function.

The local distance is computed as

$$\boldsymbol{u}_{i,j} = \mathbf{S}_j^{-1}(\boldsymbol{x}_i - \boldsymbol{x}_j) \tag{3.9}$$

where $\boldsymbol{x}_i$ and $\boldsymbol{x}_j$ are the global coordinates of point i and MP j, and $\mathbf{S}_j$ is the shape matrix given by

$$\mathbf{S}_j = \begin{bmatrix} a_j & 0 \\ 0 & b_j \end{bmatrix} \tag{3.10}$$

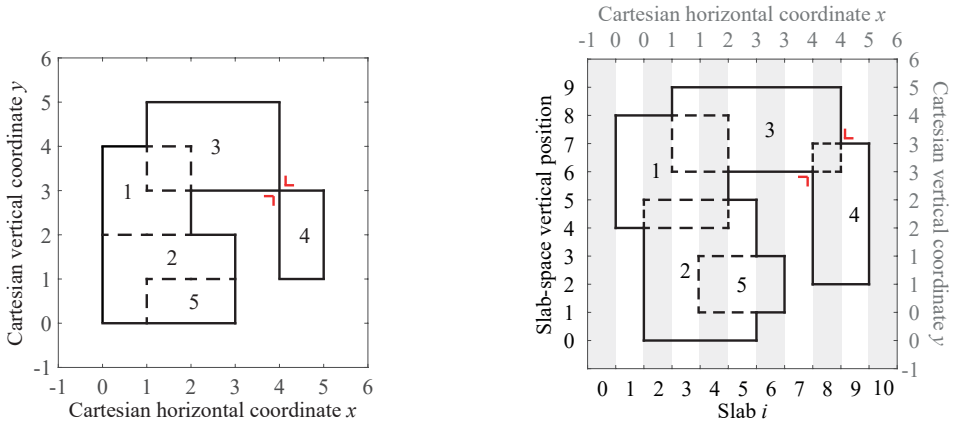

(a) (b)

Figure 3.11: Conversion from real space (a) to slab space (b) for a set of 5 rectangles according to the algorithm designed by Prusinkiewicz and Raghavan (1985). The contour is marked by the solid line and the internal edges are marked by the dashed lines. The slab space solves the ambiguity for the connection of rectangles 3 and 4, and the red right-angle corners mark this connection.

in which a_j and b_j define the size of the kernel function, see Figure 3.8. The constant C_j has here been defined as

$$C_j = \frac{2}{\pi \det(S_j)} \tag{3.11}$$

This ensures that the volume under each kernel function is equal to 1, i.e. each MP distributes the same total influence independent of its size. A C_j correlated with MP mass can be used when large differences in MP mass occur within the domain.

Figure 3.9a shows how the proximity field (PF) is constructed (for a 1D example) by summing up the kernel functions of all MPs. The PF is computed at the nodes and the boundary points are found by comparing the PF with a user specified threshold (see Figure 3.9b). In 1 dimension, the boundary points denote the 2 ends of each 1D domain as illustrated for the 2 1D domains in Figure 3.9b, and connection of the points is therefore not required. In 2 dimensions, the complete boundary is created by connecting the points using Composite Bézier Curves or B-splines as shown in Figure 3.10. Here linear segments are used. The surface is then used to compute $\boldsymbol{F}_{\text{Surface}}$ (see Section 3.3).

3.6.2. CONTOUR ALGORITHM FOR ISO-RECTANGLES

The boundary can also be constructed by merging all the GIMP support domains, such that $\boldsymbol{F}_{\text{GIMP}}$ can be computed. This merging is similar to finding the contour of a set of iso-rectangles (Prusinkiewicz and Raghavan, 1985), i.e. domains aligned in two directions (the vertical and horizontal directions). For example, 5 domains are shown in Figure 3.11a, although, in practice, any number of domains can be merged.

Prusinkiewicz and Raghavan (1985) designed an algorithm to find the contour of a set of iso-rectangles, by converting the rectangles from Cartesian space (Figure 3.11a) to a so-called slab space representing only the topology (Figure 3.11b). In slab space,

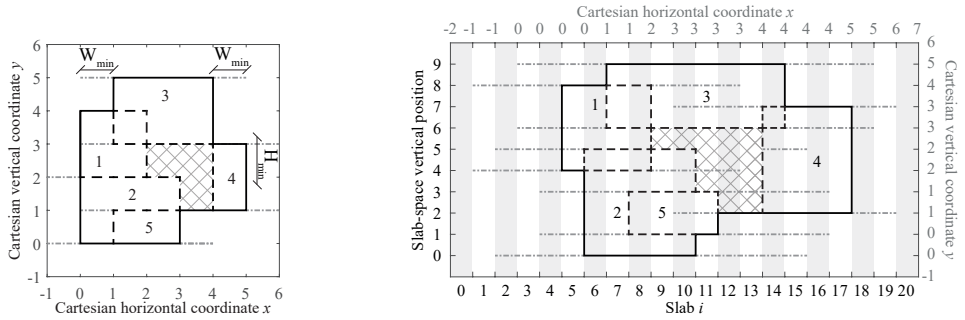

(a) (b)

Figure 3.12: Conversion from real space (a) to slab space (b) for a set of 5 rectangles according to new gap removal algorithm. Grey horizontal dashed-dotted lines mark the extended horizontal edges due to the minimum width (W_{min}). The contour is marked by the solid line, the internal edges are marked by the dashed lines, and the cross hatching highlights the removed gap.

edges with the same horizontal or vertical coordinate are separated. For example, in Figure 3.11 the bottom edge of rectangle 3 and the top edge of rectangle 4 have the same vertical Cartesian coordinate, but they have a different slab-space position. Lines with the same coordinate are separated such that left edges precede right edges and bottom edges precede top edges. Two edges with the same coordinate which are on the same side of their rectangles, for example the bottom edges of rectangles 2 and 5 in Figure 3.11, are separated according to the lowest MP number. Prusinkiewicz and Raghavan (1985) used the slab space to find the horizontal and vertical edges belonging to the contour. These edges in slab space also result in the correct contour in real space, as shown in Figure 3.11.

Due to the movement of MPs, and their support domains, small gaps between domains can appear. As the support domains represent large continuous sections of material, instead of individual material particles, the small gaps between the support domains do not represent the behaviour of the material accurately. If external loads are applied within a small gap, the gap can grow larger causing unrealistic behaviour. It is therefore preferred to fill any gaps in the boundary that are smaller than a minimum gap width, i.e. gaps with a width or height smaller than a specified minimum width (W_{min}) or height (H_{min}), respectively. When a gap is larger than this specified minimum width it is assumed to be a gap occurring in the material.

In order to fill the small gaps, the algorithm presented by Prusinkiewicz and Raghavan (1985) is here extended. Specifically, the horizontal edges of the rectangles are extended to the left and right by W_{min}, see Figure 3.12. Then, for each slab i the horizontal edges belonging to the contour are determined. Each slab i of the slab space is divided into segments (numbered from bottom to top) by the horizontal edges intersecting i. For example, slabs 10 and 11 of Figure 3.12b are divided into eleven segments as shown in Figure 3.13. Prusinkiewicz and Raghavan (1985) counted the number of rectangles overlapping each segment using a so-called invisibility number. Here multiple invisibility numbers are used (see Figure 3.13a). Invisibility number J is an integer which counts

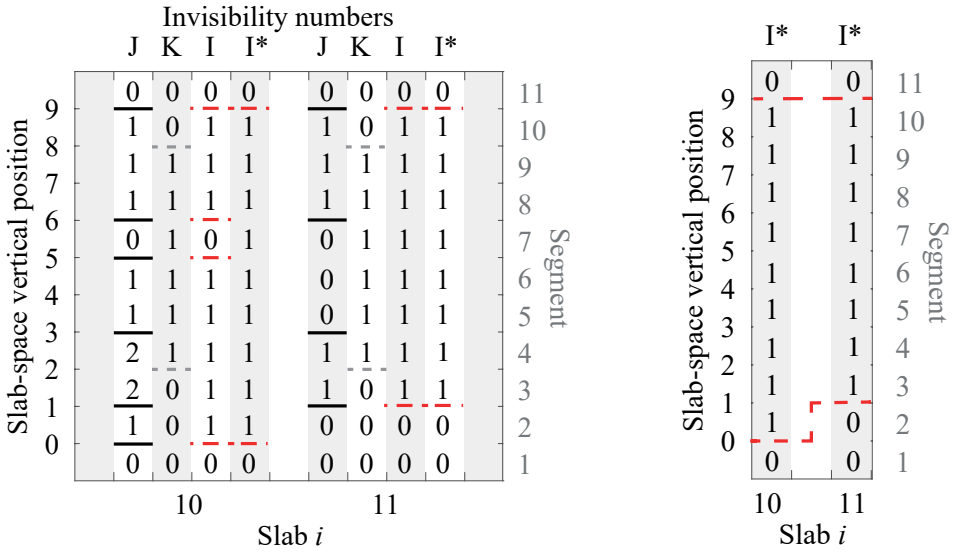

(a) (b)

Figure 3.13: (a) Computation of the 3 invisibility numbers (I, J and K) together with the associated edges for slabs 10 and 11 of Figure 3.12b (I^* indicates the invisibility number after vertical gap removal). (b) The required connection between the contour edges found in slabs 10 and 11.

how many rectangles overlap a specific segment, and can be used to determine if a segment is inside any rectangles ($J > 0$) or outside all rectangles ($J = 0$). J is computed for segment k in slab i, based on the previous segment $k-1$ in slab i and the edge m separating the segments k and $k-1$:

$$J(k) = \begin{cases} 0 & \text{if } k = 0, \\ J(k-1)+1 & \text{if } m \text{ is a real bottom edge,} \\ J(k-1)-1 & \text{if } m \text{ is a real top edge,} \\ J(k-1) & \text{otherwise.} \end{cases} \tag{3.12}$$

Similarly, invisibility number K counts the number of left extensions of rectangles overlapping a segment k, and is computed using a similar procedure as for J:

$$K(k) = \begin{cases} 0 & \text{if } k = 0, \\ K(k-1)+1 & \text{if } m \text{ is a left extension of a bottom edge,} \\ K(k-1)-1 & \text{if } m \text{ is a left extension of a top edge,} \\ K(k-1) & \text{otherwise.} \end{cases} \tag{3.13}$$

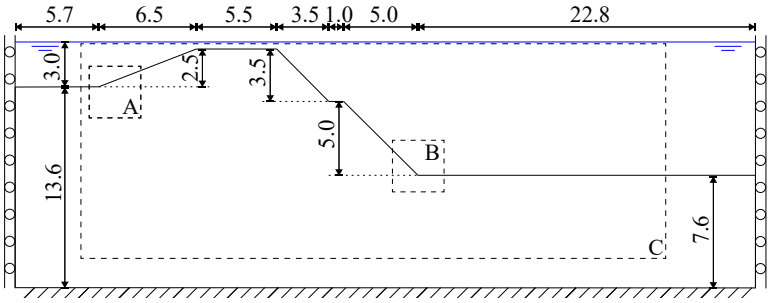

Figure 3.14: Submerged slope example problem (dimensions shown in metres).

J and K are combined to form the invisibility number I:

$$I(k) = \begin{cases} 1 & \text{if } J(K) > 0, \\ 1 & \text{if } K(K) > 0 \text{ and } k \text{ was inside the contour in slab } i-1, \\ 0 & \text{otherwise.} \end{cases} \tag{3.14}$$

A segment k is inside the contour if $I(k) = 1$ and outside when $I(k) = 0$. In other words, by combining J and K, I ensures that all rectangles are included in the final contour and horizontal gaps have been removed. To remove small vertical gaps the total height (H_{total}) of consecutive segments with $I = 0$ is computed. I^* is increased to 1 in the segments where $H_{total} <= H_{min}$.

The horizontal edges belonging to the final contour are those edges which separate segments with $I^* = 0$ from segments with $I^* = 1$. The vertical edges of the contour can be determined by comparing the horizontal edges of the contour from two consecutive slabs (Prusinkiewicz and Raghavan, 1985), see Figure 3.13b. The final contour is output as a sequence of contour edges. The coordinates of the contour polygon can be back-calculated from this sequence and the MP properties. More details on connecting relevant edges, the output and the space/time efficiency of the algorithm can be found in Prusinkiewicz and Raghavan (1985).

3.7. SUBMERGED EMBANKMENT FAILURE EXAMPLE

The applicability of the boundary detection methods for the most consistent Neumann BC techniques are evaluated for a submerged slope failure problem. The problem is analysed using implicit GIMP including stiffness double mapping, i.e. the DM-G technique is used (González Acosta et al., 2020). The problem involves a two dimensional submerged clay slope, shown in Figure 3.14, which is unstable under its own weight. The material has a unit weight of 20 kN/m^3, and the elastic deformation is governed by a Young's modulus of 1000 kPa and a Poisson's ratio of 0.45. The numerical model uses the Von-Mises softening model presented in Wang et al. (2016). The initial undrained shear strength (c_i) is 5.4 kPa at the ground surface and increases linearly with depth by 3.0 kPa every meter (giving a maximum of 54 kPa at the base of the domain immediately under the embankment crest). The residual undrained shear strength (c_r) is equal to 0.5 c_i, and

the softening modulus (H_s) is equal to -10 kPa. The background grid uses 0.5 m square elements, while the slope is discretised using MPs with rectangular support domains of varying sizes. The sizes vary such that (1) roughly 4 MPs are placed within each filled element, and (2) the slope is represented accurately, meaning that the sloping surfaces cut the GIMP support domains in a similar manner to Figure 3.5b. The simulation uses implicit time integration with a timestep size of 0.01 seconds.

The hydrostatic pressures acting on the slope are converted to nodal loads computed using either equivalent point loads at the surface MPs, traction applied on a PFM surface, or traction applied on a GIMP domain surface. In other words, the most consistent methods for GIMP are compared against the application of loads at surface MPs, a technique often used in literature. The point loads are presented as vectors in Figures 3.15 - 3.17, while the PFM surface and GIMP domain surface are plotted as solid lines. The point loads are computed at the start of the simulation based on the initial geometry and are unchanged during the simulation, while the loads from the PFM and GIMP domain surfaces are updated based on the new geometries (i.e. the loads are recomputed based on the orientation and length of the updated boundary).

The initial stresses are computed with a quasi-static load step, in which the MPs are fixed in place. Oscillations in initial stress, caused by the different external load methods, appear only locally at the surface. As these differences are difficult to observe, locations A and B, as shown in Figure 3.14, are investigated in detail. Figure 3.15 shows the vertical external forces computed with the three techniques at location B. The point loads cause higher nodal external forces inside the material (see Figure 3.15a) compared to the other two methods. This results in lower mean stresses, as shown in Figure 3.16, for the surface MPs, and, to compensate, higher stresses for the second layer of MPs compared to the other techniques. Similar stress errors are observed at the surface at location A (see Figure 3.16a). Loading the PFM surface (Figures 3.16b and 3.16e) reduces the mean stress error compared to the point loads, but still causes non-smooth stresses at the sloping faces, as was also observed in Section 3.5. Moreover, oscillations occur at the flat surface in Figure 3.16e as the detected surface is too close to the MPs. Finally, loading the GIMP domain surface gives accurate (and smooth) initial stresses (see Figures 3.16c and 3.16f).

The deviatoric stresses, investigated at the same locations, are less clearly affected by the placement of the loads (Figure 3.17). This might be due to the mean stress nature of a hydrostatic pressure condition. Small deviations can only be observed along the gentle slope (Figures 3.17a and 3.17b), while deviatoric stress errors appear negligible for the 45 degree slope (Figures 3.17d and 3.17e). Similar to the mean stress, loading the GIMP support domains leads to no observable deviatoric stress errors (Figures 3.17c - 3.17f).

In Figure 3.18 the failure process is shown, as computed by the three methods. Softening can be observed along the failure surface for all three methods. The failure develops much faster when point loads are used compared to the other two approaches, i.e. the different BC methods can lead to differences in the failure process. Moreover, the surface MPs at which the point loads are applied can be pushed downwards (Figure 3.18b) and, since the loads applied at the surface MPs are constant and the list of surface MPs is not updated, the point loads can be pushed into the material. A gap in the soil appears, as seen at 4.5 seconds (Figure 3.18c), and leads to a simulation crash.

The other two techniques present similar results, both during (Figures 3.18d, 3.18e,

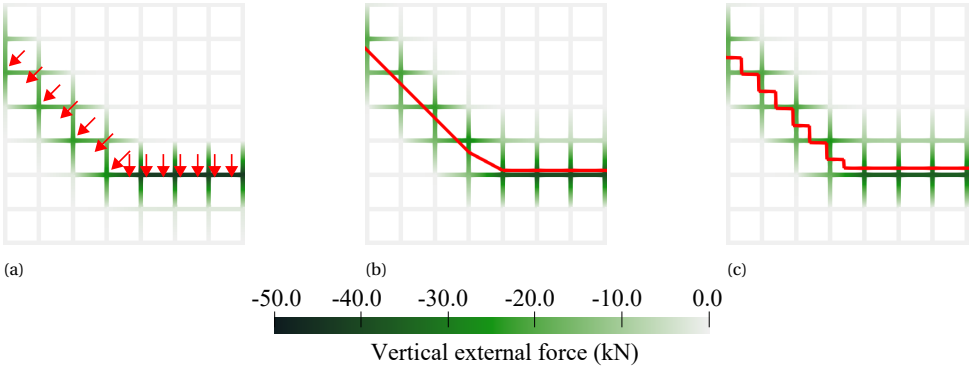

Figure 3.15: Vertical external nodal loads (kN) coloured on the background grid at location B, computed using (a) point loads applied at MPs, (b) loads applied on a PFM surface, and (c) loads applied on a surface constructed from GIMP domains. Point loads, PFM surface and GIMP support domain surface are indicatively shown in red.

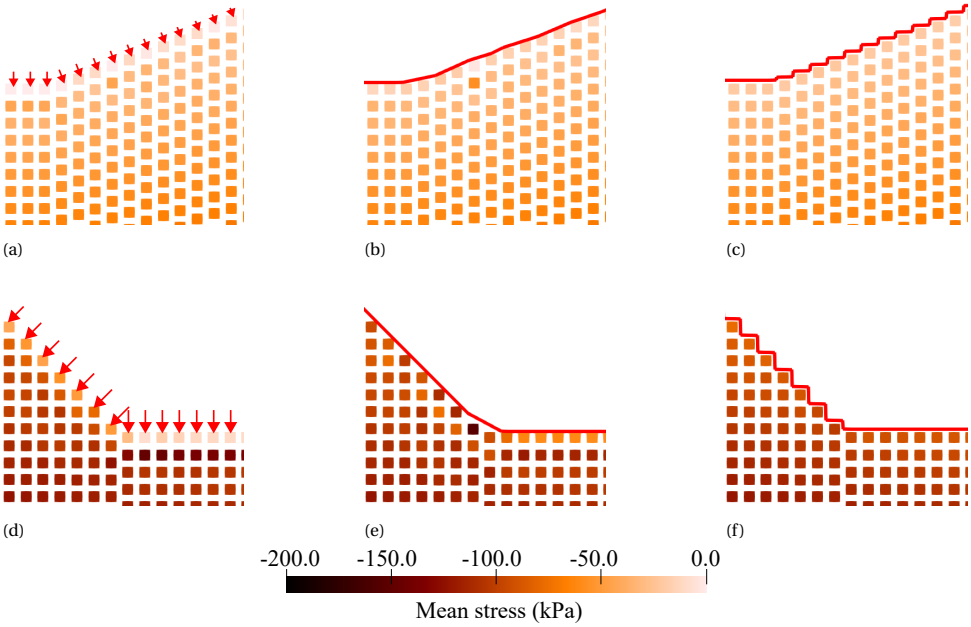

Figure 3.16: Mean total stresses at the MPs (kPa) at location A (a-c) and location B (d-f), computed using (a,d) point loads applied at MPs, (b,e) loads applied on a PFM surface, and (c,f) loads applied on a surface constructed from GIMP domains. Point loads, PFM surface and GIMP domain surface are indicatively shown.

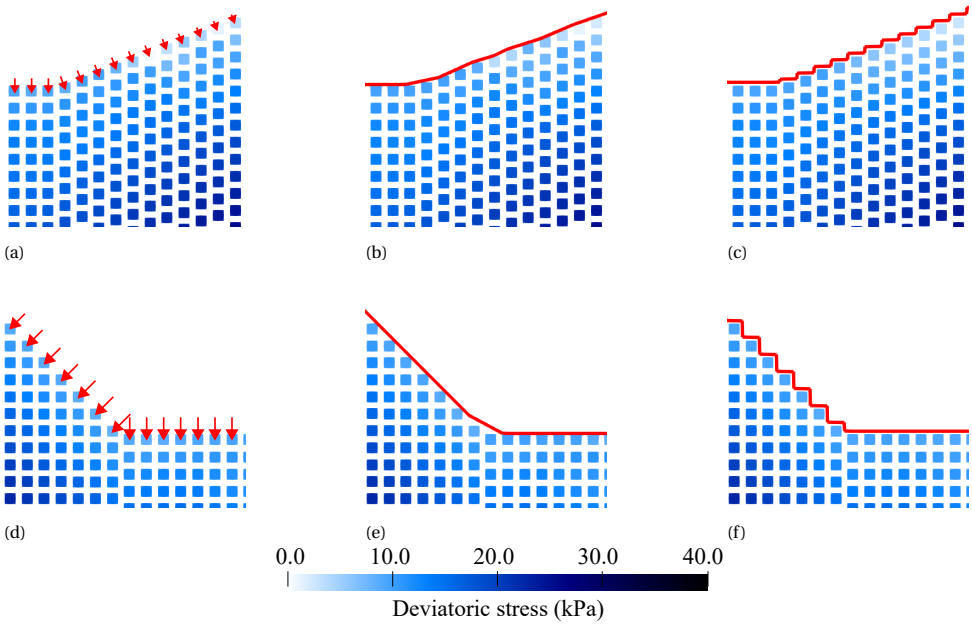

Figure 3.17: Deviatoric stresses (kPa) at the MPs at location A (a-c) and location B (d-f), computed using (a,d) point loads applied at MPs, (b,e) loads applied on a PFM surface, and (c,f) loads applied on a surface constructed from GIMP domains. Point loads, PFM surface and GIMP domain surface are indicatively shown.

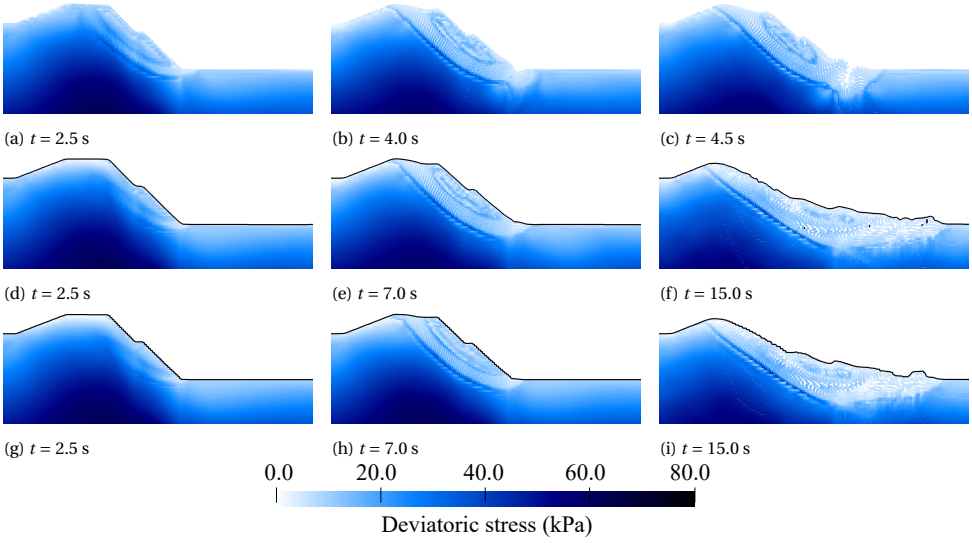

Figure 3.18: Displacement of MPs with external loads computed using: (a-c) point loads at MPs, (d-f) loads applied on the PFM surface, and (g-i) loads applied on the surface constructed from GIMP domains. MPs coloured according to the deviatoric stress (kPa). PFM and GIMP domain surfaces plotted in black.

3.18g and 3.18h) and at the end of the simulation (Figures 3.18f and 3.18i). The results are similar because the constitutive model is based on deviatoric stress, and the differences in deviatoric stress are small (as shown in Figure 3.17). Moreover, in both techniques the loads are updated based on the deformed geometry, and since the difference between the locations of the boundary with the two techniques is small the overall result is similar. However, minor differences can be observed. For example, the failure after 7.0 seconds is developed slightly further when the PFM surface is used compared to when the GIMP domains are used. Moreover, if mean stress dependent constitutive models would be used, larger differences are expected. Note that the results described here are mainly dependent on the location of the boundary condition and not on the method used to determine its location. In other words, should other methods than those presented in Section 3.6 be used to construct the boundary or the contour of GIMP support domains, similar results would be expected given that the change in boundary location is small.

3.8. CONCLUSION

It has been shown that the application of traction (Neumann, or external load) boundary conditions should show consistency between the calculation of internal and external forces. In theory, Neumann boundary conditions should be applied on the exact material surface. However, in practice due to the MPM discretisation, the internal force may not be consistent with a Neumann boundary condition on the exact material surface. These inconsistencies can lead to an incorrect surface stress distribution and change the outcome of simulations. In MPM, the volume of material considered to be within a grid cell directly relates to the number of MPs within that grid cell, and, as such, the internal force jumps in value when MPs leave the element. Therefore, the BC application should also have this feature, although it is difficult to practically implement for arrangements where the material points are not well aligned with the background grid.

Improving the discretisation, for example by using more material points or a different integration scheme such as GIMP, will reduce the difference between the consistent and exact boundary conditions. In GIMP, due to the MPs having their own domain, the material gradually leaves the grid cell as the MPs move, and the BC application should follow this behaviour. Therefore, a consistent method involves applying loads on the material point support domain. The difference between this consistent method and applying loads on the exact material surface is small in GIMP. Future research can investigate the effect of other discretisation improvements, such as material point refinement.

Two Neumann BC methods have been developed for GIMP, together with the required boundary detection methods. These techniques significantly improve the calculated stresses of material points close to the surface and have been shown to improve the failure process of a submerged slope. It is shown to be important to correctly update the location and value of the boundary condition, as loads may otherwise be applied within the material. The presented simulation with constant loads applied at fixed surface material points caused a simulation crash due to the loads being applied at incorrect locations. From the two new Neumann BC methods proposed here, applying loads at the GIMP support domain surface performed slightly better than applying loads on the actual surface, since the boundary condition is in agreement with the discretisation. However, the differences between the two methods are small, because the distance be-

tween the two boundaries is small. Using either of the two methods removes one cause of stress oscillations regularly observed in MPM-type methods.

REFERENCES

Bathe, K. J. (2014). *Finite Element Procedures* (2nd ed.). Prentice Hall.

Beuth, L. (2012). *Formulation and application of a quasi-static material point method.* (Doctoral dissertation). University of Struttgart, Germany.

Bing, Y., Cortis, M., Charlton, T. J., Coombs, W. M., & Augarde, C. E. (2019). B-spline based boundary conditions in the material point method. *Computers and Structures*, *212*, 257–274. https://doi.org/10.1016/j.compstruc.2018.11.003

Chen, Z., Hu, W., Shen, L., Xin, X., & Brannon, R. (2002). An evaluation of the MPM for simulating dynamic failure with damage diffusion. *Engineering Fracture Mechanics*, *69*(17), 1873–1890. https://doi.org/10.1016/S0013-7944(02)00066-8

Colagrossi, A., & Landrini, M. (2003). Numerical simulation of interfacial flows by smoothed particle hydrodynamics. *Journal of Computational Physics*, *191*(2), 448–475. https://doi.org/10.1016/S0021-9991(03)00324-3

Cortis, M., Coombs, W., Augarde, C., Brown, M., Brennan, A., & Robinson, S. (2018). Imposition of essential boundary conditions in the material point method. *International Journal for Numerical Methods in Engineering*, *113*(1), 130–152. https://doi.org/10.1002/nme.5606

de Koster, P., Tielen, R., Wobbes, E., & Möller, M. (2021). Extension of B-spline material point method for unstructured triangular grids using Powell–Sabin splines. *Computational Particle Mechanics*, *8*(2), 273–288. https://doi.org/10.1007/s40571-020-00328-3

Federico, I., Marrone, S., Colagrossi, A., Aristodemo, F., & Antuono, M. (2012). Simulating 2D open-channel flows through an SPH model. *European Journal of Mechanics - B/Fluids*, *34*, 35–46. https://doi.org/10.1016/j.euromechflu.2012.02.002

Fern, E. J., Rohe, A., Soga, K., & Alonso, E. E. (2019). *The Material Point Method for Geotechnical Engineering* (J. Fern, A. Rohe, K. Soga, & E. Alonso, Eds.). CRC Press. https://doi.org/10.1201/9780429028090

Fernández-Méndez, S., & Huerta, A. (2004). Imposing essential boundary conditions in mesh-free methods. *Computer Methods in Applied Mechanics and Engineering*, *193*(12-14), 1257–1275. https://doi.org/10.1016/j.cma.2003.12.019

González Acosta, J. L., Vardon, P. J., Remmerswaal, G., & Hicks, M. A. (2020). An investigation of stress inaccuracies and proposed solution in the material point method. *Computational Mechanics*, *65*, 555–581. https://doi.org/10.1007/s00466-019-01783-3

Hu, W., & Chen, Z. (2003). A multi-mesh MPM for simulating the meshing process of spur gears. *Computers and Structures*, *81*(20), 1991–2002. https://doi.org/10.1016/S0045-7949(03)00260-8

Huerta, A., & Fernández-Méndez, S. (2000). Enrichment and coupling of the finite element and meshless methods. *International Journal for Numerical Methods in Engineering*, *48*(11), 1615–1636. https://doi.org/10.1002/1097-0207(20000820)48:11\textless1615::AID-NME883\textgreater3.0.CO;2-S

Kumar, A. V., Padmanabhan, S., & Burla, R. (2008). Implicit boundary method for finite element analysis using non-conforming mesh or grid. *International Journal for Numerical Methods in Engineering, 74*, 1421–1447. https://doi.org/10.1002/nme.2216

Liu, C., & Sun, W. (2019). Shift boundary material point method: an image-to-simulation workflow for solids of complex geometries undergoing large deformation. *Computational Particle Mechanics, 7*, 291–308. https://doi.org/10.1007/s40571-019-00239-y

Main, A., & Scovazzi, G. (2018). The shifted boundary method for embedded domain computations. Part I: Poisson and Stokes problems. *Journal of Computational Physics, 372*, 972–995. https://doi.org/10.1016/j.jcp.2017.10.026

Mao, S., Chen, Q., Li, D., & Feng, Z. (2016). Modeling of free surface flows using improved material point method and dynamic adaptive mesh refinement. *Journal of Engineering Mechanics, 142*(2), 04015069. https://doi.org/10.1061/(ASCE)EM.1943-7889.0000981

Martinelli, M., Al-Kafaji, I., Ceccato, F., Rohe, A., Yerro-Colom, A., & Chmelnizkij, A. (2017). *MPM software – Anura3D*. Anura3D MPM Research Community.

Martinelli, M., & Galavi, V. (2021). Investigation of the material point method in the simulation of cone penetration tests in dry sand. *Computers and Geotechnics, 130*, 103923. https://doi.org/10.1016/j.compgeo.2020.103923

Martinelli, M., Lee, W.-L., Shieh, C.-L., & Cuomo, S. (2021). Rainfall boundary condition in a multiphase material point method. In B. Tiwari, K. Sassa, P. Bobrowsky, & K. Takara (Eds.), *Understanding and Reducing Landslide Disaster Risk. WLF 2020. ICL Contribution to Landslide Disaster Risk Reduction* (pp. 303–309). Springer, Cham. https://doi.org/10.1007/978-3-030-60706-7_29

Mast, C. M., Mackenzie-Helnwein, P., Arduino, P., & Miller, G. R. (2011). Landslide and debris flow-induced static and dynamic loads on protective structures. In R. I. Borja (Ed.), *Multiscale and Multiphysics Processes in Geomechanics* (pp. 169–172). Springer-Verlag Berlin Heidelberg. https://doi.org/10.1007/978-3-642-19630-0_43

Moormann, C., & Hamad, F. (2015). MPM dynamic simulation of a seismically induced sliding mass. *IOP Conference Series: Earth and Environmental Science, 26*(1), 012024. https://doi.org/10.1088/1755-1315/26/1/012024

Phuong, N., van Tol, A., Elkadi, A., & Rohe, A. (2016). Numerical investigation of pile installation effects in sand using material point method. *Computers and Geotechnics, 73*, 58–71. https://doi.org/10.1016/j.compgeo.2015.11.012

Prusinkiewicz, P., & Raghavan, V. V. (1985). A simple space-optimal contour algorithm for a set of iso-rectangles. *Congressus Numerantium, 46*, 249–270.

Remmerswaal, G. (2017). *Development and implementation of moving boundary conditions in the material point method* (Master's thesis). Delft University of Technology.

Sethian, J. A. (1996). Theory, algorithms, and applications of level set methods for propagating interfaces. *Acta Numerica, 5*, 309–395. https://doi.org/10.1017/S0962492900002671

Tjung, E. Y. S. (2020). *Material point method for large deformation modeling in geomechanics using isoparametric elements* (Doctoral dissertation). University of California, Berkeley.

Tjung, E. Y. S., Kularathna, S., Kumar, K., & Soga, K. (2020). Modeling irregular boundaries using isoparametric elements in material point method. *Geo-Congress 2020*, 39–48. https://doi.org/10.1061/9780784482803.005

Wang, B., Karuppiah, V., Lu, H., Komanduri, R., & Roy, S. (2005). Two-dimensional mixed mode crack simulation using the material point method. *Mechanics of Advanced Materials and Structures*, *12*(6), 471–484. https://doi.org/10.1080/15376490500259293

Wang, B., Vardon, P. J., & Hicks, M. A. (2018). Rainfall-induced slope collapse with coupled material point method. *Engineering Geology*, *239*, 1–12. https://doi.org/10.1016/j.enggeo.2018.02.007

Wang, B., Vardon, P. J., & Hicks, M. A. (2016). Investigation of retrogressive and progressive slope failure mechanisms using the material point method. *Computers and Geotechnics*, *78*, 88–98. https://doi.org/10.1016/j.compgeo.2016.04.016

Wang, L., Coombs, W. M., Augarde, C. E., Cortis, M., Brown, M. J., Brennan, A. J., Knappett, J. A., Davidson, C., Richards, D., White, D. J., & Blake, A. P. (2021). An efficient and locking-free material point method for three-dimensional analysis with simplex elements. *International Journal for Numerical Methods in Engineering*, *122*(15), 3876–3899. https://doi.org/10.1002/nme.6685

Zhao, X., Bolognin, M., Liang, D., Rohe, A., & Vardon, P. J. (2019). Development of in/outflow boundary conditions for MPM simulation of uniform and non-uniform open channel flows. *Computers & Fluids*, *179*, 27–33. https://doi.org/10.1016/j.compfluid.2018.10.007

4

RISK FRAMEWORK FOR RESIDUAL DYKE RESISTANCE

A risk-based approach for dyke safety can determine an optimal balance between flood risk costs and the costs of interventions. The new Dutch safety standards adopt risk-based decision making and probabilities of flooding are therefore required. To compute probabilities of flooding, a framework which assesses failure processes from their initiation until flooding is needed. Therefore, a risk framework for dyke failure including secondary failure mechanisms is presented in this chapter. The framework extends the standard risk framework for dykes and accounts for the inherent uncertainty in the hydraulic loads using fragility curves. Secondary failure processes are split into separate mechanisms to determine the likelihood of the failure process. The framework for macro-instability is presented and can be used as the basis of dyke assessments using the Random Material Point Method (RMPM).

This chapter is based on the risk framework presented in the following paper: Remmerswaal, G., Vardon, P. J., & Hicks, M. A. (2021). Evaluating residual dyke resistance using the Random Material Point Method. *Computers and Geotechnics, 133*, 104034. https://doi.org/10.1016/j.compgeo.2021.104034.

4.1. INTRODUCTION

Historically, levees were built, or strengthened after flooding occurred, to withstand a water level higher than the highest recorded water level. More recently, levee design has been based on a return period of flooding, by extrapolating a design water level from the particular return period. The chosen return period can be converted to a yearly probability of flooding, when the dyke integrity can be ensured up to the chosen design water level. However, ensuring this integrity is practically impossible at higher design water levels, since a (small) probability of failure of the dyke, before the design water level is reached, is always present. The international levee handbook (van Hemert et al., 2013) therefore promotes the adoption of a risk-based approach, where the focus is moved away from withstanding a particular design water level with absolute certainty to evaluating the flood risk at a range of operational conditions. The goal is to determine an optimal balance between flood risk costs and costs of interventions, in order to provide the most value to users and stakeholders of a levee (Jonkman et al., 2018).

In 2017, new dyke safety standards were introduced in the Netherlands (Waterwet, 2009). According to these standards, dyke flood risk should be assessed based on all relevant uncertainties. Three types of risk indicators are used to derive the new safety standards (van Alphen, 2016): individual risk, group risk, and a cost-benefit analysis. Risk-based decision making based on these three criteria ensure that dykes are economically efficient (Kind, 2014), while limiting the risk to individuals and large groups.

For adequate risk-based decision making, all (known) uncertainties should be quantified and taken into account (Klerk, 2022). The uncertainties are sometimes split into two types of uncertainty: epistemic (knowledge) and aleatory (inherent) uncertainty. Knowledge uncertainties are assumed to be reducible, i.e. gaining a better understanding of the problem reduces the uncertainty, while inherent uncertainties are not (van Gelder, 2022). In reality, most uncertainties are not purely epistemic or aleatory, and the categories should rather better be seen as the limit along an axis which highlights the effectiveness of information in reducing a specific uncertainty. Additionally, epistemic uncertainty is only reducible within the constraints of a model (Klerk, 2022). In other words, an adequate framework is required to capture and reduce the uncertainty. In regards to residual dyke resistance after slope instability, a framework (and model) to capture the uncertainties related to primary and secondary failure mechanisms is needed.

To assess the damage due to the primary failure mechanisms, several (Dutch) guidelines have been proposed over the last decades (Blinde et al., 2018; ENW, 2009; Knoeff et al., 2021; MIM, 2016). These simple models approximate the damaged dyke profile based on the failure surface from LEM and assumptions on the amount of deformation. Actual displacements during real dyke slope failures or large scale dyke failure tests do not confirm these assumptions (van Duinen, 2010; van Duinen et al., 2022). Rozing et al. (2013) extended the simple guidelines to a method which computed the displacement of a failure block. The method computes the stability of a rotated failure surface using LEM with the assumption of a reduced strength along the failure surface. By iteratively increasing the rotation, the rotation (and thereby deformation) at which a new equilibrium is obtained could be determined. However, due to the new standards focusing on a probabilistic approach for macro-instability, this 'new' deterministic approach has not been used in practice.

Probabilistic frameworks have been designed for residual dyke resistance using event trees, where the primary slope instability may be followed by several secondary failure mechanisms (Calle, 2002; van der Krogt et al., 2019; van der Meer, 2021). The probability of flooding can be approximated by following the event tree of the most critical failure process, i.e. the sequence of most likely slope failures (van der Krogt et al., 2019). Event trees were used by van der Meer (2021) to assess secondary slope failure, and in addition wave overtopping after macro-instability. While promising, these event trees are unable to capture the wide range of failure processes, as paths within the event trees are often predefined and limited. This chapter therefore presents a risk framework which determines the risk of flooding according to a wide range of failure processes.

Section 4.2 summarises the basis of the Dutch risk framework. Section 4.3 explains how multiple primary failure mechanisms caused by inherently uncertain hydraulic loads may be assessed within this framework. Each of these mechanisms may be followed by a wide range of secondary failure processes. These secondary failure processes can be captured by the framework, as shown for macro-instability in Section 4.4.

4.2. RISK FRAMEWORK

To design or assess dykes in a risk based framework, both the probability of failure $P(F)$ of a dyke and the consequence of failure $C(F)$ are required, since the risk of failure is defined as

$$\text{Risk}(F) = P(F) \cdot C(F) \tag{4.1}$$

Since flooding can be considered as the dominant limit state for dykes, the probability of flooding and the consequence of flooding should be considered. The consequence of flooding is (almost) independent of the failure process before flooding, i.e. it is independent of how a dyke failed. This work focuses on the computation of the probability of flooding, since the consequence of flooding is often included separately in safety standards. For example, in the Netherlands the maximum allowable probability of flooding (P_s), based upon a minimisation of the combined cost of dyke reinforcement and the consequence of flooding, is defined:

$$P(F) \leq P_s \tag{4.2}$$

A limit state function Z can also be defined, by considering the resistance against failure R and the loads triggering failure L (Schneider, 2006). Hence, for failure to occur,

$$Z = R - L < 0 \tag{4.3}$$

so that the probability of flooding becomes

$$P(F) = P[R < L] = P[Z < 0] \tag{4.4}$$

R and L are modelled and/or measured and both may contain model uncertainty (M), material (or 'quantity') uncertainty (Q) and geometric uncertainty (D), i.e. the random variables describing R and L are functions containing the uncertainties as an input (among others):

$$R = R(\mu_R, M_R, Q_R, D_R) \text{ and } L = L(\mu_L, M_L, Q_L, D_L) \tag{4.5}$$

where μ is the mean of the subscript distribution. The material uncertainty can be further split into measurement uncertainty and transformation uncertainty where indirect measurements are taken. In addition, the resistance and loads may be functions or models that are dependent on other variables, each of which may have uncertainties. Combining Eq. (4.3) and Eq. (4.5), the random variable describing Z becomes a function of all the uncertainties (and other input parameters):

$$Z = Z(\mu_Z, M_R, Q_R, D_R, M_L, Q_L, D_L) \tag{4.6}$$

Geometric uncertainties D_r and D_s tend to be limited, due to the relatively high measurement accuracy, and are, from here on, considered to be negligible (see Varkey et al. (2022) for an investigation of the relative importance of geometric uncertainties). Moreover, model uncertainties are ignored, since they have not yet been established for MPM. It is here assumed that the model uncertainties are small compared to the other sources of uncertainties. Hence, this work focuses on uncertainties relating the spatial variability of material properties and uncertainties relating to the external loading (due to the external water level). Since some of the uncertainties are ignored, the probability estimates provided in the thesis are lower bounds.

4.3. COMBINATION OF FAILURE CATEGORIES

The major failure categories of a dyke are considered to be overtopping, piping, macro-instability of the inner slope, damage to the cover of the outer slope and failure of structures which are part of the dyke (MIM, 2017a). Assuming, conservatively, that all failure categories are mutually exclusive, a separate limit state function Z_i can be defined for each failure category F_i. The probability of flooding $\mathrm{P}(F) = \mathrm{P}[Z < 0]$ is considered to be the union of Z_i, which can be expressed as

$$\mathrm{P}(F) = \mathrm{P}(Z_1 < 0 \cup Z_2 < 0 \cup \cdots Z_{n_c} < 0) = \mathrm{P}(F_1 \cup F_2 \cup \cdots F_{n_c}) = \sum_{i=1}^{n_c} \mathrm{P}(F_i) \tag{4.7}$$

where $\mathrm{P}(F_i) = \mathrm{P}(Z_i < 0)$ and n_c is the total number of failure categories. To account for categories that have not been considered/calculated (semi-)probabilistically, e.g. internal erosion or damage to cables and ducts, etc., two separate approaches are used in the Dutch guidelines (MIM, 2017b): 1) $\mathrm{P}(F_i)$ can be computed for each major failure category, while 30% of $\mathrm{P_s}$ is reserved for categories for which $\mathrm{P}(F_i)$ cannot be computed, i.e.

$$\mathrm{P}(F) = \sum_{i=1}^{n_c} \mathrm{P}(F_i) \leq 0.7\mathrm{P_s} \tag{4.8}$$

or 2) $\mathrm{P_s}$ is subdivided into a standard portion for each major failure category, such that

$$\mathrm{P}(F_i) \leq \omega_i \mathrm{P_s} \tag{4.9}$$

where ω_i is the portion of $\mathrm{P_s}$ reserved for $\mathrm{P}(F_i)$. Standard values can be provided for ω_i; for example, $\omega_i = 0.04$ for macro-instability in MIM (2017b). In this framework, the first approach is followed, but the framework can easily be converted to approach 2. For most

failure categories F_i, only the initiation (or primary) mechanism A_i^1 is assessed, i.e.

$$\mathrm{P}(F) = \sum_{i=1}^{n_c} \mathrm{P}(F_i|A_i^1)\mathrm{P}(A_i^1) \leq 0.7\mathrm{P_s} \tag{4.10}$$

where $\mathrm{P}(A_i^1)$ is the probability of A_i^1 and $\mathrm{P}(F_i|A_i^1)$ is the probability of flooding given A_i^1. $\mathrm{P}(A_i^1)$ can be calculated using semi-probabilistic methods, or more robust (but computationally more intensive) probabilistic methods. However, $\mathrm{P}(F_i|A_i^1)$, typically cannot be calculated with conventional methods, and therefore $\mathrm{P}(A_i^1)$ is often assumed to always lead to flooding, i.e.

$$\mathrm{P}(F_i|A_i^1) = 1 \text{ for all } i \tag{4.11}$$

This conservative approximation simplifies Eq. (4.10), by removing the need to calculate $\mathrm{P}(F_i|A_i^1)$:

$$\mathrm{P}(F) = \sum_{i=1}^{n_c} \mathrm{P}(A_i^1) \leq 0.7\mathrm{P_s} \tag{4.12}$$

However, where significant remaining dyke resistance is available, computing $\mathrm{P}(F_i|A_i^1)$ leads to a significant reduction in the probability of flooding and it is then beneficial to use Eq. (4.10) instead of Eq. (4.12).

Considering an uncertain water level h, Eq. (4.10) may be expressed in terms of h using fragility curves, i.e. probabilities of flooding given a specific water level $\mathrm{P}(F|h)$ (Simm et al., 2009), such that

$$\mathrm{P}(F) = \int \mathrm{P}(F|h)f(h)dh = \int \sum_{i=1}^{n_c} \mathrm{P}(F_i|A_i^1,h)\mathrm{P}(A_i^1|h)f(h)dh \tag{4.13}$$

where $f(h)$ is the probability density function of h given the hydraulic conditions imposed on the dyke, i.e. all conditions influencing the external water level, such as wind, upstream conditions, tidal currents, and so on. In addition, $\mathrm{P}(F_i|A_i^1,h)$ is the probability of flooding given the occurrence of a specific primary mechanism at a water level h, and $\mathrm{P}(A_i^1|h)$ is the probability of occurrence of the primary failure mechanism given h. The integral can be numerically approximated from the calculation of discrete values and interpolation. Fragility curves can reduce the probability of flooding compared to an assessment based on a design water level. The reduction is the largest when $\mathrm{P}(F|h)$ is small for the most likely water levels h.

4.4. MACRO-INSTABILITY

To demonstrate the framework, macro-instability, i.e. dyke slope instability, is considered here, although the concepts can be extended to other failure categories. To reduce the number of subscripts, the symbol S (slope instability) is used for the occurrence of macro-instability instead of A_i.

A series of events leading to flooding over a dyke usually ends with a breach event, i.e. erosion of the dyke by flowing water (Calle, 2002). This occurs once the maximum height of the dyke drops below the external water level. Therefore, the limit state function Z of flooding itself can be defined as

$$Z = H - h \tag{4.14}$$

where the dyke height H can be seen as the resistance against flooding and the water level h as the load. The dyke height H may change due to instabilities or other mechanisms, i.e. H is a dynamic property during the failure process. The probability of flooding is therefore given by

$$P(F_i) = P(Z < 0) = P(H - h < 0) \tag{4.15}$$

After a primary macro-instability failure, flooding may occur directly (see for example Figure 5.2a) or by way of secondary mechanisms; e.g. retrogressive failure (see for example Figure 5.2c), internal erosion (i.e. micro-instability), or wave-overtopping. For simplicity, in this work the occurrence of wave-overtopping or internal erosion after macro-instability are not considered, and only retrogressive failure, the secondary mechanism most closely related to the primary mechanism, is considered.

When fragility curves are used in combination with Eq. (4.15), the probability of flooding can be computed separately for specific water levels as

$$P(F_i|h) = P(Z < 0|h) = P(H - h < 0|h) \tag{4.16}$$

After evaluating all possible macro instabilities, this leads to

$$P(F_i|h) = \int P(H - h < 0|S, h)P(S|h)dS \tag{4.17}$$

where S is one of the possible failure processes, which may or may not lead to flooding. In RMPM, the possible failure processes are explicitly modelled within a Monte-Carlo framework, i.e. equation 4.17 is evaluated.

In other evaluation methods, it can be easier to split the failure processes into a sequence of separate failure mechanisms, where each failure mechanism causes significant damage to the dyke. The probability of each separate failure mechanism can then be approximated and combined to compute the probability of flooding. This approximation may even be performed with small deformation models or empirical guidelines developed based on results from large deformation models (such as RMPM).

To evaluate the sequence of separate failure mechanisms an event tree approach may be used. Figure 4.1 describes the event tree for the j th failure mechanism in the failure process, i.e. failure mechanism S_j. The event tree for failure mechanism S_j starts when a previous failure mechanism S_{j-1} occurred which did not trigger flooding (event $\bar{F}_{j-1}$). From this state the probability of flooding directly after failure mechanism S_j given $\bar{F}_{j-1}$ can be computed as

$$P(F_j|\bar{F}_{j-1}) = P(F_j|S_j)P(S_j|\bar{F}_{j-1}) \tag{4.18}$$

where $P(F_j|S_j)$ is the probability of flooding directly after S_j given the occurrence of S_j, and $P(S_j|\bar{F}_{j-1})$ is the probability of failure mechanism S_j given the starting state. This approach assumes a Markov process, i.e. the next event in the event tree is only (directly) dependent on the most recent event in the sequence. $P(F_j|\bar{F}_{j-1})$ only includes the probability of flooding caused by S_j directly, and not the probability of flooding caused by subsequent failure mechanisms after S_j. $P(F_j|S_j)$ may be evaluated by comparing the height of the dyke H after S_j with the external water level h:

$$P(F_j|S_j) = P(H - h < 0|S_j) \tag{4.19}$$

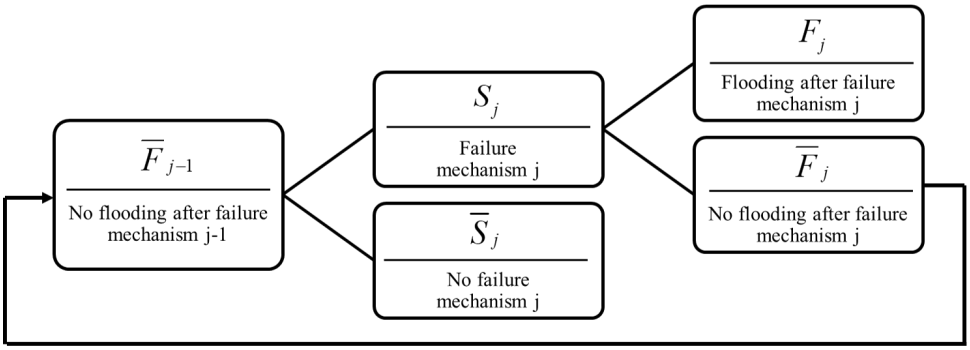

Figure 4.1: Event tree for failure mechanism S_j in the sequence of failure mechanisms potentially leading to flooding

The event tree (Figure 4.1) may also be used to compute the probability of the next state, i.e. the probability that flooding does not occur after mechanism S_j:

$$\mathrm{P}(\bar{F}_j|\bar{F}_{j-1}) = (1-\mathrm{P}(F_j|S_j))\mathrm{P}(S_j|\bar{F}_{j-1}) \tag{4.20}$$

$\bar{F}_j$ can then be used as the initial state of the next event tree, as indicated in Figure 4.1. The probability of flooding for a failure process which leads to flooding directly after S_j can be evaluated by repeatedly using the event tree in Figure 4.1:

$$\mathrm{P}(F_j|\bar{F}_0) = \mathrm{P}(F_j|S_j)\mathrm{P}(S_j|\bar{F}_{j-1})\prod_{k=1}^{j-1}\mathrm{P}(\bar{F}_k|\bar{F}_{k-1}) \tag{4.21}$$

where $\mathrm{P}(\bar{F}_k|\bar{F}_{k-1})$ can be evaluated using Eq. (4.20), and $\mathrm{P}(\bar{F}_0)$ is the probability that flooding did not occur with an intact dyke, i.e.

$$\mathrm{P}(\bar{F}_0) = 1-\mathrm{P}(H_0-h<0|h) \tag{4.22}$$

In this work it is assumed that the water level is below the initial height of the dyke, i.e. $\mathrm{P}(\bar{F}_0)=1$.

Finally, to compute the total probability of flooding due to all possible processes, the probability of flooding after any number of separate failure mechanisms must be combined, i.e.

$$\mathrm{P}(F_i|h) = \mathrm{P}(F|\bar{F}_0) = \sum_{j=1}^{\infty}\mathrm{P}(F_j|S_j)\mathrm{P}(S_j|\bar{F}_{j-1})\prod_{k=1}^{j-1}\mathrm{P}(\bar{F}_k|\bar{F}_{k-1}) \tag{4.23}$$

Even though the summation in Eq. (4.23) is infinite, in practice the probability of occurrence $\mathrm{P}(S_j|\bar{F}_{j-1})$ reduces quickly as j increases, and a conservative estimate can be found by defining a maximum number of failure mechanisms l and assuming the associated probability of flooding $\mathrm{P}(F_l|S_l)=1$, which limits the summation to

$$\mathrm{P}(F_i|h) = \mathrm{P}(F|\bar{F}_0) = \sum_{j=1}^{l}\mathrm{P}(F_j|S_j)\mathrm{P}(S_j|\bar{F}_{j-1})\prod_{k=1}^{j-1}\mathrm{P}(\bar{F}_k|\bar{F}_{k-1}) \tag{4.24}$$

where $P(F_l|S_l)$ is assumed to be 1.

In recent research (van der Krogt et al., 2019), Eq. (4.23) has been evaluated assuming that the probability of flooding can be computed by following the most critical failure process S^c, i.e. only evaluating the critical failure mechanisms S^c_k. This procedure starts by computing the probability of the critical primary failure mechanism $P(S^c_1)$ using LEM. The damaged dyke geometry is approximated based on the critical primary failure mechanism S^c_1 and assumptions on the post failure behaviour (e.g. that only rotational sliding occurs and that the slide is stationary after a vertical deformation of $0.5H$), without considering the effect of uncertainty on the geometry of the damaged dyke.

If the damaged dyke geometry prevents flooding, i.e. $H > h$, the probability of flooding after the primary mechanism $P(F_1|S_1|h)$ is assumed to be 0. The probability of $P(S^c_2)$ is then computed (using LEM) according to an assumed damaged dyke geometry, i.e. $P(S^c_2) = P(S^c_2|S^c_1)P(S^c_1)$, after which the approximated damaged dyke geometry is again compared to the water level. This procedure, of computing the probability of S^c_k and comparing the approximated damaged dyke geometry after S^c_k with the water level, is repeated until the approximated damaged dyke geometry after S^c_j causes flooding. Under these assumptions, Eq. (4.23) simplifies to

$$P(F_i|h) = P(F_j|S^c_j) \prod_{k=1}^{j} P(S^c_k|S^c_{k-1}) = \prod_{k=1}^{j} P(S^c_k|S^c_{k-1}) \tag{4.25}$$

which inherently assumes that flooding always occurs at S_j, i.e. $P(F_j|S_j,h) = 1$, and flooding does not occur before S_j, i.e. $PF_k|S_k,h) = 0$ for all $k \neq j$, and that the sequence of critical failure mechanisms is a good representation of all possible failure mechanisms and thereby the probability of flooding. However, sub-critical failure mechanisms might have a larger probability of flooding, as the failure mechanisms may be larger, reducing residual dyke resistance (van der Krogt et al., 2019). In some cases, a sub-critical primary failure mechanism might even lead to flooding directly.

4.5. CONCLUSIONS

A risk framework for dyke failure including secondary failure mechanisms has been presented. The framework extends the standard Dutch risk framework, such that the entire failure process until a dyke breach may be included. The framework can include the inherent uncertainty in hydraulic loads using fragility curves, and evaluates the possible failure processes which may lead to flooding. The Random Material Point Method (RMPM) evaluates these failure processes within a Monte-Carlo framework.

It is shown how the failure processes may also be split into separate mechanisms, such that the probability of the mechanism may be evaluated separately. The probability of all potential subsequent mechanisms, until the dyke height drops below the water level, are determined. Combining the probability of the subsequent mechanisms results in the probability of the failure process. RMPM can be used to determine the probability of the separate mechanisms, which can be helpful in assessing methods based on small deformations which use the framework with separated mechanisms. While the framework can be used for all primary failure mechanisms, only macro-instability (dyke slope instability) has been presented here, as it is the basis of the dyke assessment using

the Random Material Point Method (RMPM) used in the remainder of this thesis. It is shown how the framework may also be further simplified, such that only critical failure processes are accounted for.

REFERENCES

Blinde, J., Bisschop, C., de Visser, M., Jongejan, R., & Tigchelaar, J. (2018). *Afweging ter bepaling glijvlak voor faalmechanisme macrostabiliteit binnenwaarts (translated in English: Consideration for determining failure surface for failure mechanism macro-instability)* (Factsheet). Kennisplatform Risicobenadering.

Calle, E. O. F. (2002). *Dijkdoorbraakprocessen (translated in English: Dijk breach processes)* (tech. rep. CO-720201/39). GeoDelft.

ENW. (2009). *Actuele sterkte van dijken (translated in English: Actual strength of dykes)* (tech. rep.). Expertisenetwerk Water Veiligheid.

Jonkman, S. N., Voortman, H. G., Klerk, W. J., & van Vuren, S. (2018). Developments in the management of flood defences and hydraulic infrastructure in the Netherlands. *Structure and Infrastructure Engineering*, *14*(7), 895–910. https://doi.org/10.1080/15732479.2018.1441317

Kind, J. (2014). Economically efficient flood protection standards for the Netherlands. *Journal of Flood Risk Management*, *7*(2), 103–117. https://doi.org/10.1111/jfr3.12026

Klerk, W. J. (2022). *Decisions on life-cycle reliability of flood defence systems* (Doctoral dissertation). Technische Universiteit Delft, Delft. https://doi.org/10.4233/uuid:877bed45-d775-40bb-bde2-d2322cb334f0

Knoeff, H., Bossenbroek, J.-K., Jongejan, R., Bisschop, C., & de Visser, M. (2021). *Werkwijze falen door macrostabiliteit (translated in English: Workflow failure by macro-instability)* (Factsheet). Adviesteam dijkontwerp.

MIM. (2016). *Schematiseringshandleiding macrostabiliteit (translated in English: Guidelines for schematization of macro-instability)* (tech. rep.). Ministerie van Infrastructuur en Milieu.

MIM. (2017a). Regeling veiligheid primaire waterkeringen - Bijlage III Sterkte en veiligheid (translated in English: Regulation primary flood defences - Attachment III Strength and safety).

MIM. (2017b). Regeling veiligheid primaire waterkeringen 2017 - Bijlage I Procedure (translated in English: Regulation primary flood defences - Attachment I Procedure).

Rozing, A. P. C., Zwanenburg, C., van Duinen, T. A., & Calle, E. O. F. (2013). *Technisch rapport macrostabiliteit (translated in English: Technical report macro-stability)* (tech. rep. 1204203-007-GEO-0003). Deltares.

Schneider, J. (2006). *Introduction to Safety and Reliability of Structures* (2nd ed.). International Association for Bridge; Structural Engineerin.

Simm, J., Gouldby, B., Sayers, P., Flikweert, J. J., Wersching, S., & Bramley, M. (2009). Representing fragility of flood and coastal defences: Getting into the detail. In P. Samuels, S. Huntington, W. Allsop, & J. Harrop (Eds.), *Proceedings of the European Conference on Flood Risk Management Research into Practice (FLOODRISK 2008)* (pp. 621–631). Taylor & Francis Group.

van der Krogt, M. G., Schweckendiek, T., & Kok, M. (2019). Do all dike instabilities cause flooding? *13th International Conference on Applications of Statistics and Probability in Civil Engineering, ICASP 2019*. https://doi.org/10.22725/ICASP13.461

van der Meer, A. (2021). *Het kwantificeren van binnenwaarste stabiliteit inclusief vervolgmechanismen (translated in English: Quantification of inner slope stability including secondary failure mechanisms)* (tech. rep. 11205740-002-GEO-0004). Deltares.

van Alphen, J. (2016). The Delta Programme and updated flood risk management policies in the Netherlands. *Journal of Flood Risk Management*, *9*(4), 310–319. https://doi.org/10.1111/jfr3.12183

van Duinen, A. (2010). *SBW Werkelijke sterkte van dijken - validatie WS15 (translated in English: SBW True strength of dykes - validation WS15)* (tech. rep. 1202121-003-GEO-0022). Deltares.

van Duinen, T. A., van Esch, J., Martinelli, M., Teixeira, A., & Wojciechowska, K. (2022). *Vervolgprocessen na macro-instabiliteit - Urgente onderzoeksonderwerpen (translated in English: Secondary processes after macro-instability - Urgent research subjects)* (tech. rep. 11206817-018-GEO-0002). Deltares.

van Gelder, P. H. A. J. M. (2022). *Statistical methods for the risk-based design of civil structures* (Doctoral dissertation). Technische Universiteit Delft, Delft.

van Hemert, H., Igigabel, M., Pohl, R., Sharp, M., Simm, J., Tourment, R., & Wallis, M. (Eds.). (2013). *The International Levee Handbook*. CIRIA.

Varkey, D., Hicks, M. A., & Vardon, P. J. (2022). Effect of uncertainties in geometry, interlayer boundary and shear strength properties on the probabilistic stability of a 3D embankment slope. *Georisk: Assessment and Management of Risk for Engineered Systems and Geohazards (published online)*, 1–15. https://doi.org/10.1080/17499518.2022.2101066

Waterwet. (2009). Waterlaw: BWBR0025458. http://wetten.overheid.nl/BWBR0025458/2018-01-01#

5

EVALUATING RESIDUAL DYKE RESISTANCE IN TWO DIMENSIONS

The Random Material Point Method (RMPM) is used in this chapter to investigate residual dyke resistance in two dimensions. An idealised dyke is assessed for slope instability and the subsequent failure process. An external hydrostatic pressure on the dyke's outer slope has been applied on the exact material surface using the Proximity Field Method (PFM). The residual resistance of an idealised dyke (computed using RMPM) is shown to reduce the probability of flooding by 25% with respect to the initial failure for a material with layered spatial variability. A lower degree of anisotropy of the spatial variability (a material with less layering) increases the residual dyke resistance and causes a reduction in the probability of flooding of more then 80%. RMPM simulates, as expected, a lower residual dyke resistance for larger initial failures and/or a higher water level. A 'safe' remaining geometry has not been found, since even small initial failures can result in an unacceptable probability of flooding when the failure process is not modelled. This highlights the importance of modelling the entire failure process.

This chapter is based on the following paper: Remmerswaal, G., Vardon, P. J., & Hicks, M. A. (2021). Evaluating residual dyke resistance using the Random Material Point Method. *Computers and Geotechnics, 133*, 104034. https://doi.org/10.1016/j.compgeo.2021.104034.

5.1. INTRODUCTION

This chapter estimates the difference between the probability of initial failure and flooding, accounting for the effect of soil heterogeneity. The analyses include an external water load, which is applied using the Proximity Field Method (PFM) described in Chapter 3. Note that the analyses in this chapter were performed before the completion of the further algorithmic developments reported in Chapter 3. However, Chapter 3 shows that the differences between using PFM and the consistent load application on GIMP domains are small, especially when slope angles of 45° and deviatoric stress dependent constitutive models are used, as is the case in this chapter. Therefore, the expected difference between using PFM and a consistent load on GIMP domains would be small, and the analyses reported in this chapter have not been repeated to include more recently developed application of loads on GIMP domains.

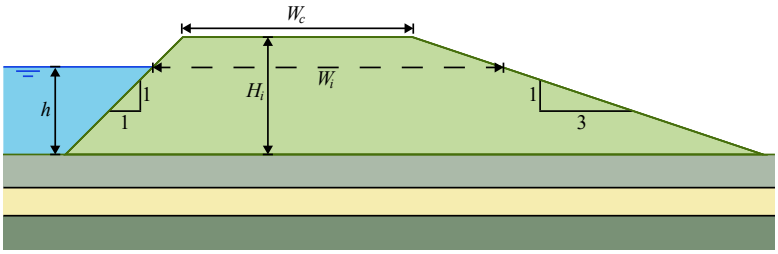

Figure 5.1: Dyke geometry, with water level h, original dyke height H_i, crest width W_c, dyke width at water level W_i, outer slope of 1:1 and inner slope of 1:3.

An idealised dyke cross-section, with a simple geometry compared to dykes typically seen in practice, is used throughout this chapter, to demonstrate the capabilities of RMPM. The dyke, shown in Figure 5.1, has an initial height H_i = 5 m, an inner (right-hand-side) slope of 1 in 3 and an outer (left-hand-side) slope of 1 in 1. The outer slope angle is steeper than that of a usual dyke, in order to increase the necessity of an external water load on the outer slope for maintaining stability and thereby test the veracity of the external loading implementation. The water level is assumed to be constant. In addition, the width of the crest, W_c = 10 m, is relatively large in order to more fully explore the effect of residual dyke resistance. The water level h is varied and the dyke is underlain by additional soil layers.

Figure 5.2 shows potential failure mechanisms related to macro-instability. A deep rotational slide is shown in Figure 5.2a, where flooding occurs immediately. Deep slides usually result in limited residual dyke resistance, due to the size of the failure. Conversely, residual dyke resistance is usually seen when the dyke is founded on a stiff layer (as shown in Figures 5.2b - 5.2e). In this case, a shallow rotational slide (as shown in Figure 5.2b) causes a reduction of the width of the dyke W (defined at the water level), while the maximum height of the dyke H remains unchanged. A rotational slide can be followed by a retrogressive failure, i.e. a secondary rotational failure which is caused by a strength reduction due to the first failure (Figure 5.2c), which may or may not result in flooding. Multiple successive retrogressive failures can also lead to flooding.

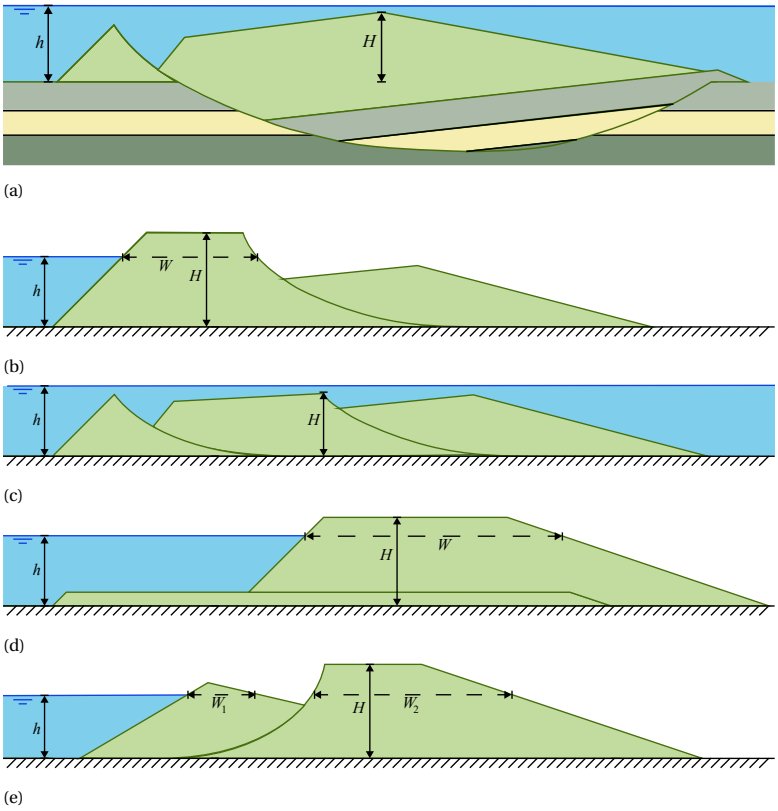

Figure 5.2: Dyke failure process for macro-instability: a) deep rotational slide, which causes flooding ($H < h, W = 0$); b) rotational initial failure ($H \approx H_i, W < W_i$); c) retrogressive failure, which causes flooding ($H < h, W = 0$); d) horizontal sliding failure ($H \approx H_i, W \approx W_i$); e) outward rotational failure ($H \approx H_i, W = W_1 + W_2 < W_i$ or $W = W_1 + W_2 > W_i$); based on Calle (2002) and 't Hart et al. (2016).

The external water loading can also push the entire dyke section sideways to cause a horizontal sliding mechanism (Figure 5.2d). The height of the dyke tends to slowly decrease during such a slide, while the width stays more or less constant. In the longitudinal direction of the dyke, a horizontal slide may only occur along a small stretch, so that water may flow through a gap created by the slide. However, since the simulations performed here are 2 dimensional, this 3-dimensional effect is neglected. Finally, especially for lower water levels, failure of the outer slope may occur, see Figure 5.2e, after which retrogressive failure in the opposite direction is possible. Combinations of the previously mentioned failure mechanisms may also occur; for example, a horizontal sliding mechanism after inner or outer slope instability.

This chapter continues with the implementation of the framework presented in Chapter 4 using RMPM (Section 5.2). Sections 5.3 and 5.4 present a parametric investigation into the probability of initial failure and subsequent flooding.

5.2. MODELLING METHOD (RMPM)

The entire failure process is here modelled using the Material Point Method (MPM). Spatial variability of the material properties is considered by way of random fields, and an ensemble approach is utilised such that uncertainties are included via use of the Monte Carlo Method, resulting in the so-called Random MPM (RMPM). In this chapter, a total stress, i.e. single phase, plane strain MPM is used. The undrained shear strength softening model described by Wang et al. (2016) is used to represent strength reduction due to pore pressure build up during failure.

The degradation of the undrained shear strength is governed by the plastic deviatoric strains according to the shear strain softening Von Mises constitutive model (Wang et al., 2016). In this constitutive model, there is a linear relationship between the undrained shear strength (c) and the plastic deviatoric shear strain invariant ($\bar{\varepsilon}_p$) until a minimum is reached, as shown in Figure 5.3. The undrained shear strength decreases linearly from the initial undrained shear strength (c_i) to the residual undrained shear strength (c_r). The residual strength is reached when $\bar{\varepsilon}_p = \bar{\varepsilon}_{pr}$. The softening modulus H_s determines the softening rate, and is used to compute $\bar{\varepsilon}_{pr}$. See Wang et al. (2016) for further details on the constitutive model.

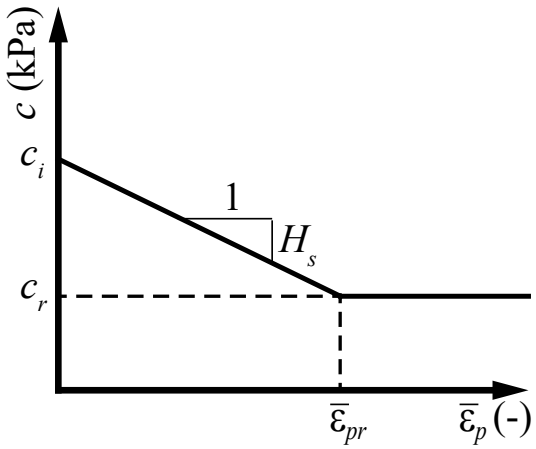

Figure 5.3: Sketch of the plastic deviatoric shear strain softening Von Mises constitutive model (after Wang et al., 2016).

Implicit MPM is used, so that larger time steps can be used to reduce the computation time (Wang et al., 2016). In the standard MPM formulation, stress oscillations occur as MPs move through the mesh and especially when they cross element boundaries. In order to limit such oscillations, the DM-G technique has been used in this chapter (González Acosta et al., 2020). This method uses extended GIMP shape functions (and shape function gradients) to reduce the cell crossing error, as well as FEM Gauss point stiffness integration to reduce the error due to movement within the background grid cells. The Gauss point properties are acquired by the mapping of material point properties via the background grid nodes.

5.2.1. RANDOM FIELDS

Random fields are used to model the spatial variability of soil properties, and have herein been generated using Local Average Subdivision (Fenton and Vanmarcke, 1990). The random field values are mapped onto the MPs in their initial positions at the start of the analysis, and the material properties of each MP remain constant throughout a single realisation, unless strength degradation occurs. Spatial variability has only been considered for the shear strength properties of the material, with all other material properties being assumed deterministic. Specifically, the initial and residual undrained shear strengths, c_i and c_r, respectively, are considered to be spatially variable. They are assumed to be fully correlated, so that the spatial variability of both properties can be constructed from a single random field. Partially correlated random fields for different properties are also possible (e.g. Vardon et al. (2016)), but are not considered here for reasons of simplicity.

The spatial variability is defined by the point statistics, i.e. the mean μ and standard deviation σ, and by the spatial statistics, i.e. the horizontal and vertical scales of fluctuation, θ_h and θ_v, respectively. The point statistics of the initial and residual undrained shear strengths, μ_{ci}, σ_{ci} and μ_{cr}, σ_{cr} respectively, are different, whereas the same scales of fluctuation have been assumed for both properties.

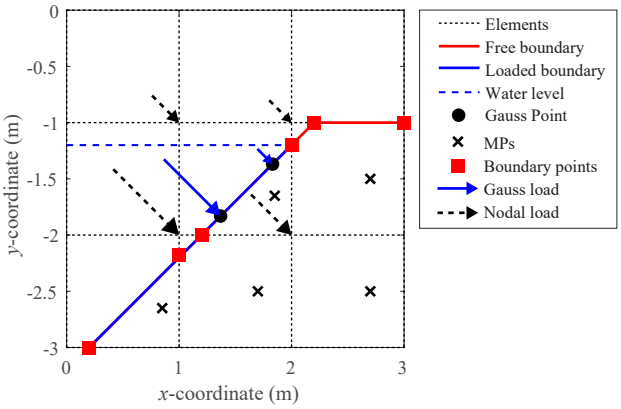

Figure 5.4: 2D example of the detected boundary with PFM, and the application of hydrostatic pressure to one boundary segment via Gauss integration and the corresponding conversion to nodal loads.

5.2.2. EXTERNAL WATER LOAD

The boundary is detected using the Proximity Field Method (PFM) (see Chapter 3). Hydrostatic pressure is applied on the boundary segments from left to right, i.e. from the outer side towards the inner side of the dyke, until one segment is above (or partially above) the water level (Figure 5.4). Gauss integration is used along the segments to integrate the hydrostatic pressure (Bing et al., 2019; Remmerswaal, 2017), as illustrated in Figure 5.4 for one segment (which extends from y = -2 m to y = -1.2 m). The hydrostatic pressure and the direction of the applied pressure at the Gauss point are computed using the depth below the water level and the direction normal to the boundary, respectively.

Gauss integration along the boundary allows the pressure to be converted to external nodal loads.

5.2.3. DETECTION OF INITIAL FAILURE AND FLOODING FROM RESIDUAL DYKE GEOMETRY

In each time step, the external geometry is determined using the boundary detection method. Two values are extracted; namely, the width W and height H, as shown in Figure 5.2. H is the maximum height of the dyke, whereas W is the width of the dyke at the water level h. $H(t)$ and $W(t)$ are used to detect the moments when the initial failure mechanism S_1 and flooding F occur. After an initial slide, W will be smaller than the original width of the dyke, i.e. $W < W_i$ as shown in Figures 5.2a and 5.2b. Moreover, W decreases to 0 and $H < h$ when flooding occurs (Figure 5.2b). The residual width W_r and residual height H_r are the width and height at the end of the simulation. The probability of S_1 with a time of failure (t_{S_1}) before a time t can be computed from the realisations in a Monte Carlo simulation, i.e.

$$\mathrm{P}(S_1|h, t_{S_1} < t) \approx \frac{N_{S_1}(t)}{N} = \frac{N_{W(t)<W_i}}{N} \tag{5.1}$$

where $N_{S_1}(t) = N_{W(t)<W_i}$ is the number of realisations where an initial failure mechanism has occurred before time t and N is the total number of realisations. Similarly, the probability of flooding with a time of flooding (t_F) before t is computed as

$$\mathrm{P}(F|h, t_F < t) \approx \frac{N_F(t)}{N} = \frac{N_{H(t)<h}}{N} \tag{5.2}$$

where $N_F(t) = N_{H(t)<h}$ is the number of realisations in which flooding occurred before t. The total probability of initial failure and flooding within a simulation are then given by

$$\mathrm{P}(S_1) = \mathrm{P}(S_1, t_{S_1} < t_{max}) \tag{5.3}$$

and

$$\mathrm{P}(F) = \mathrm{P}(F, t_F < t_{max}) \tag{5.4}$$

respectively. The relative difference between the probability of flooding and the probability of initial failure is the metric considered for residual dyke strength, and is given by

$$\mathrm{P}(F|S_1) = \frac{\mathrm{P}(F)}{\mathrm{P}(S_1)} \tag{5.5}$$

5.3. ANALYSES

The dyke presented in Section 5.1 has been simulated. A weak strain softening clay, with a mean initial undrained shear strength μ_{ci} of 13 kPa and a sensitivity $S_c = c_i/c_r = 2.6$, is used as the dyke material. c_i and c_r are therefore fully correlated. These material properties were chosen to represent a dyke with a relatively high probability of failure, in order to enable reasonably quantitative results within a manageable number of realisations for investigating the deformation processes during dyke failure. For the efficient computation of smaller, more realistic, probabilities of initial failure and flooding, RMPM can be

Table 5.1: Model details.

Geometry	Discretisation	Material Properties	
H_i = 5 m	Δt = 0.01 s	γ_w = 15 kN/m^3	c_i = N(μ_{ci} = 13 kPa, COV = 0.2)
W_i = 10 m	t_{max} = 40 s	E = 1000 kPa	$c_r = c_i / S_c$, S_c = 2.6
Inner slope 1:3	$\Delta x = \Delta y$ = 0.25 m	ν = 0.45	θ_v = 0.5 m
Outer slope 1:1	N_{MPs} = 6400	H_S = -50 kPa	0.5 m < θ_h < 48.0 m

Table 5.2: Summary of analyses.

Analysis 1: Base Case	
θ_h = 24.0 m	$H_i - h$ = 0.25 m
Analysis set 2: Horizontal scale of fluctuation	
θ_h = 0.5, 1.0, 2.0, 4.0, 6.0, 8.0, 12.0, 24.0, 48.0 m	$H_i - h$ = 0.25 m
Analysis set 3: Water level	
θ_h = 24.0 m	$H_i - h$ = 0.25, 0.5, 1.0, 1.5, 2.0 m

combined with subset simulation, as has already been done successfully with RFEM (van den Eijnden and Hicks, 2017).

The random fields of c_i and c_r are assumed to be normally distributed with a coefficient of variation of $COV = \sigma/\mu = 0.2$. The distributions have been cut off to prevent negative strength properties. This cutoff has limited impact because of the chosen (relatively small) coefficient of variation. The vertical scale of fluctuation is θ_v = 0.5 m and is similar to the range of values reported in de Gast et al. (2017), whereas a horizontal scale of fluctuation of θ_h = 24.0 m has been assumed for the Base Case (Analysis 1). Due to the uncertainty that is generally associated with determining horizontal scales of fluctuation, the influence of θ_h is investigated in Analysis set 2, with θ_h being varied from 0.5 m (the isotropic case) to 48 m, the latter representing a layered system with a θ_h larger than the width of the dyke.

The unit weight of the dyke clay γ_w is 15 kN/m^3 and the elastic properties have been chosen in order to increase the efficiency of the MPM calculations, i.e. E = 1000 kPa and ν = 0.45, since MPM simulations converge more slowly with less compressible materials. The softening modulus of the undrained shear strength is H_S = -50 kPa. For Analysis 1 and Analysis set 2, the water level is constant at h = 4.75 m (i.e. 0.25 m below the dyke crest), whereas the effect of lower water levels is investigated in Analysis set 3, for water levels varying from 0.25 m to 2 m below the crest. A summary of the model details and the performed analyses are provided in Table 5.1 and Table 5.2, respectively.

A mesh of 4 noded square elements and an element size $\Delta x = \Delta y$ of 0.25 m is used, together with 4 equally spaced MPs per element (giving N_{MPs} = 6400 MPs in total). Along the sloping faces of the dyke, the number of MPs per element is adjusted and the MPs redistributed, in order to match the geometry. The nodes along the bottom boundary are completely fixed, so as to model a dyke resting on a firm foundation (as illustrated

in Figures 5.2b to 5.2e). The random field is generated with a cell size corresponding to the material point domain, i.e. $\Delta x/2$ by $\Delta y/2$, such that the properties of a single cell correspond to one material point. Hence, as the random field cell size is 4 times smaller than the smallest scale of fluctuation (i.e. θ_v), the spatial variability is adequately captured (see, for example, Huang and Griffiths (2015)).

The time step Δt is 0.01 s, which is significantly larger than would have been required using explicit MPM (González Acosta et al., 2020). The maximum simulation time t_{max} is 40 s. The in-situ stresses are generated quasi-statically using gravity loading, assuming an elastic material, whereas plasticity and dynamics are considered during the simulation itself. At the start of the simulation, the plasticity generates unbalanced forces at the nodes, which may lead to an initial failure. To reduce the vibrations caused by suddenly switching on plasticity at the start of the simulation, damping is used. The unbalanced forces are artificially reduced (damped) by 100% at the start and then gradually increased until they have been fully applied after 1 s; thereafter, no damping is used. The realisation is terminated if (a) flooding occurs, (b) the dyke does not fail at all, or (c) the dyke, having experienced slope failure, no longer moves and no longer develops plastic strains (for at least 1 s).

Each RMPM simulation comprises 10 000 realisations, i.e. 10 000 computations with MPM, which have been performed in parallel on a new grid computing system called Spider, at SURFsara, a national computing centre in the Netherlands. This number is higher than for typical RFEM simulations, due to the greater range of possible failure mechanisms arising from the evolving failure process being modelled in the simulations.

5.4. RESULTS

5.4.1. ANALYSIS 1: BASE CASE

The final dyke geometries for 6 realisations of Analysis 1 are presented in Figure 5.5. Realisations without any failure are by far the most common type, as illustrated by the example in Figure 5.5a. In contrast, Figure 5.5b shows an initial failure mechanism, initiating through a weak layer approximately 1.5 m above the base. Due to the weak layer, a slip circle is formed, along which the soil reduces in strength due to strain softening as the failure progresses, as indicated by the dark slip surface. Moreover, due to the large deformations, the sliding mass breaks up into 2 distinct blocks separated by a secondary failure surface inclined at approximately 45° to the slip circle. Since the depth through which the failure surface forms is limited, the initial failure does not develop further and reaches the stable configuration shown in the figure.

Figure 5.5c presents the most likely initial failure mechanism, which occurs along a weaker layer close to the base of the dyke and resembles failure in a homogeneous material. Again, the sliding mass breaks into 2 blocks separated by a secondary failure surface at approximately 45°. The figure shows some softening in the weak layers directly behind the slip circle, but enough resistance remains to prevent a second (retrogressive) failure and the possibility of flooding.

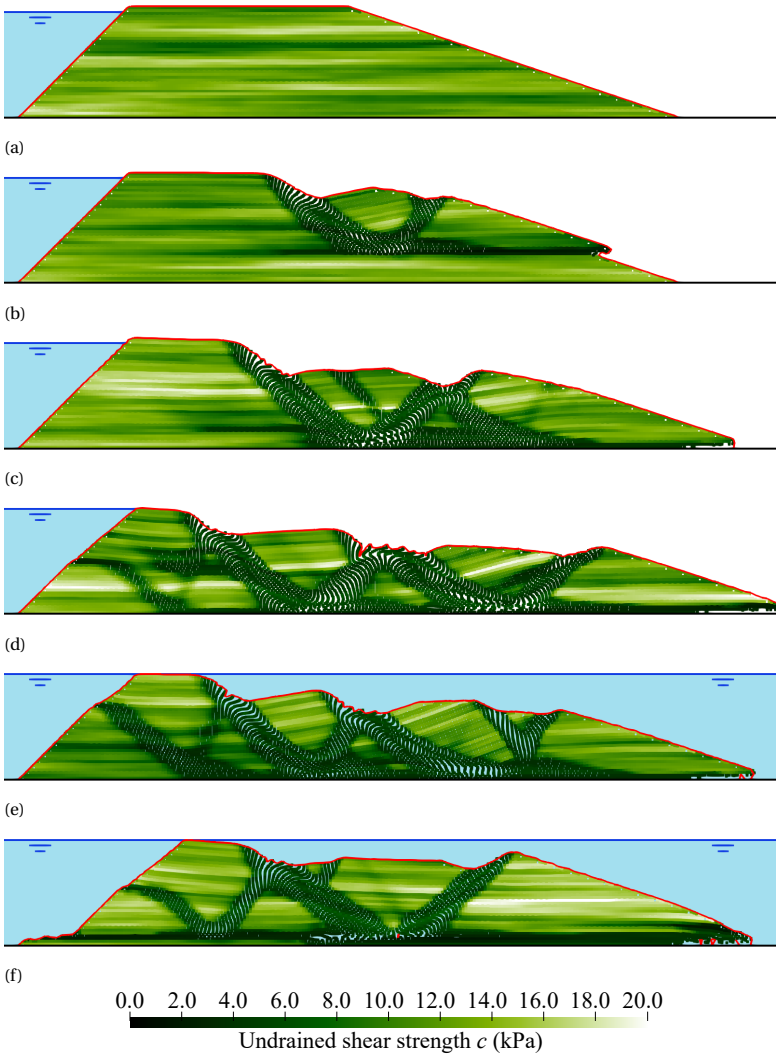

Figure 5.5: RMPM realisations from Analysis 1 showing the final deformed position, with material points coloured according to the undrained shear strength (c): a) no initial failure; b) initial failure through weak zone above the foundation; c) initial failure along foundation layer; d) retrogressive failure without flooding; e) retrogressive failure with flooding; f) initial (circular) failure mechanism followed by horizontal slide triggering flooding. The red line is the detected boundary and the black line is the fixed boundary. The water level is indicatively shown.

Retrogressive failure does occur in Figures 5.5d and 5.5e. After an initial slide, a second slide fully develops in both figures; in addition, a third slide partially develops in Figure 5.5d and fully develops in Figure 5.5e. Once again, breaking up of the sliding masses can be observed. While the height of the dyke is almost unaffected in Figures 5.5b and 5.5c, the height of the dyke reduces in both Figures 5.5d and 5.5e. The final height of the dyke in Figure 5.5d is slightly higher than the water level and, in reality, the dyke may flood due to wave-overtopping. However, under the current modelling assumptions, the dyke remains stable and flooding was prevented. In contrast, a flood is triggered in Figure 5.5e. In reality, a breach would then occur due to erosion, causing further (catastrophic) damage to the remainder of the dyke; but, since the model immediately stops after flooding, the geometry in Figure 5.5e is the final configuration.

A different type of mechanism is shown in Figure 5.5f, where an initial rotational slide triggers a horizontal secondary slide along a very weak layer near the base of the dyke, eventually resulting in flooding. This highlights that RMPM is capable of approximating both rotational and horizontal sliding mechanisms.

It is seen that the leading tip of the primary slip surface in Figures 5.5b-5.5f is suspended above the remaining slope or foundation, most likely due to the element discretisation adopted in MPM, i.e. the leading tip flows at the top of the first row of elements above the foundation layer instead of on top of the foundation layer itself. This error may be removed by including a contact algorithm between the flowing material and the foundation layer (González Acosta et al., 2021). However, in these analyses this effect only occurs at the tip of the slip surface, where the strength is limited, and it therefore has limited impact on the results.

The probability of failure, i.e. the probability of initial failure $P(S_1)$ and flooding $P(F)$, of Analysis 1 over time and the probability of failure before a given time are shown in Figure 5.6. The probability of flooding is lower than the probability of initial failure (i.e. $\sim$ 9% compared to $\sim$ 12%), indicating that residual dyke resistance is present in this analysis. The metric used to quantify the residual dyke resistance ($P(F|S_1)$) is 0.75 for this analysis, i.e. a relative reduction in the probability of flooding of 25%. The residual dyke resistance is small due to the high probability of secondary failures due to the weak layers which trigger initial failure. Failure occurs faster than would normally be expected (realistic failures may take minutes or hours), due to the low residual undrained shear strength, the absence of damping and the instantaneous triggering of failure due to the loading conditions.

A deterministic MPM simulation based on the mean strength properties (μ_{ci} = 13 kPa and μ_{cr} = 5 kPa) did not lead to initial failure, and gave a factor of safety (FoS) $\approx$ 1.3 (computed using the strength reduction method). In a deterministic homogeneous MPM simulation with a reduced strength, such that FoS is just below 1 ($c_i \approx 10$ kPa and $c_r \approx 3.85$ kPa), failure occurs after 4 s, and flooding occurs 3.5 s later due to retrogressive failure. By integrating the probability distribution of c_i until 10 kPa, the probability of FoS < 1.0 has been determined as 0.13, i.e. $P(FoS < 1.0) = P(N(\mu_{ci}, COV) < 10) = 0.13$. Therefore, the estimated probability of initial failure based only on the point statistics (13%) is similar to the probability of initial failure found with RMPM for this problem (12%). However, the difference becomes much larger with smaller values of θ_h, as will be demonstrated by Analysis set 2.

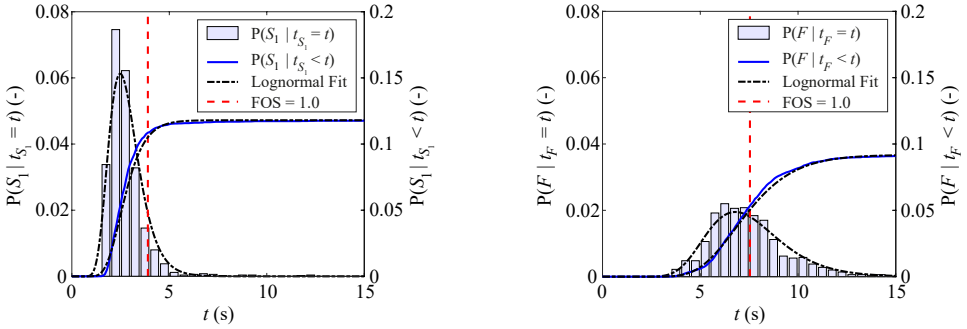

(a) (b)

Figure 5.6: Probability of failure over time and before a given time for Analysis 1: a) initial failure mechanism; b) flooding.

Indeed, with realistic soil properties, when the probability of failure of the dyke is much lower than the one computed here, RFEM (or RMPM) generally computes a much lower probability of initial failure compared to the estimation based only on the point statistics (Hicks et al., 2019). Moreover, in this case, a reduction in the probability of flooding compared to the probability of initial failure is not observed in the homogeneous MPM simulation, since flooding occurred at the same strength as initial failure. A further reduction in the probability of flooding is observed using RMPM. Therefore, RFEM can be used to reduce the conservatism regarding initial dyke failure by accounting for spatial variability, while RMPM can further reduce this conservatism by also accounting for residual dyke resistance.

5.4.2. ANALYSIS SET 2: EFFECT OF HORIZONTAL SCALE OF FLUCTUATION

PROBABILITY OF FAILURE

Figure 5.7 presents the probability of an initial failure mechanism and the probability of flooding for various horizontal scales of fluctuation, i.e. the results of Analysis set 2. Figure 5.7a shows that, if it occurs, the initial failure mechanism triggers 2 to 5 s after the start of the simulation. As for the Base Case, flooding occurs later if the residual resistance is overcome, see Figure 5.7b. The times over which flooding may occur are more widely spread than the times of initial failure.

Figure 5.7 clearly shows that, as expected, the probability of flooding is lower than the probability of initial failure for all horizontal scales of fluctuation. Moreover, according to Figure 5.8a, the largest absolute decrease in the probability of flooding compared to the probability of initial failure occurs at an intermediate value of θ_h. However, more importantly, Figure 5.8b shows that the residual resistance ($P(F|S_1)$) is highest at small horizontal scales of fluctuation, since the probability of flooding given the occurrence of an initial failure is the smallest. For large horizontal scales of fluctuation, the probability of an initial failure increases, see Figure 5.8. Failures are more likely to occur in weak layers in the presence of larger horizontal scales of fluctuations and retrogressive failure has a greater tendency to occur through these same weak layers, thereby reducing

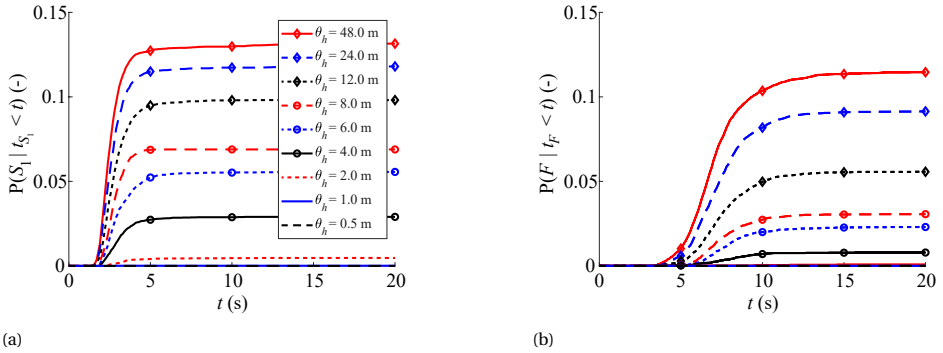

(a) (b)

Figure 5.7: Probability of failure as a function of time for various horizontal scales of fluctuation (θ_h): a) initial failure mechanism; b) flooding.

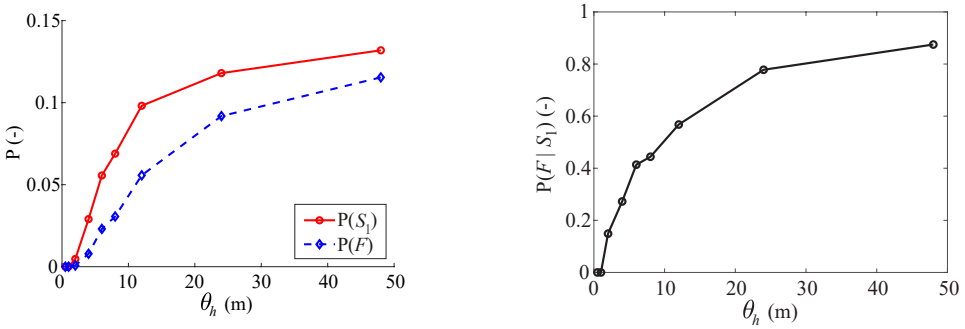

(a) (b)

Figure 5.8: a) Probabilities of initial failure and flooding and b) probability of flooding given initial failure, i.e. residual dyke resistance, for various horizontal scales of fluctuation (θ_h).

the residual resistance. $P(F|S_1)$ ranges from 0.9 at large horizontal scales of fluctuation to below 0.2 at small horizontal scales of fluctuation, i.e. a <10% reduction for layered materials and a >80% reduction for materials with limited layering.

Finally, at small horizontal scales of fluctuation (smaller than 4 m) the probability of initial failure and flooding are low and additional realisations may be required to improve the accuracy of the predicted probabilities. Subset simulation could alternatively be used to further investigate residual dyke resistance at lower probabilities of initial failure (van den Eijnden and Hicks, 2017).

RESIDUAL DYKE GEOMETRY

Figure 5.9 shows histograms of the residual geometry, $H_r - h$ and W_r, for Analysis set 2. The histograms in Figures 5.9a and 5.9b exclude completely stable dykes, which all have $W_r \approx 10.5$ m and $H_r - h = 0.25$ m, and flooded dykes, which all have $W_r = H_r - h = 0$, see Figure 5.9c. The histograms in Figures 5.9a and 5.9b have been normalised with respect to the total number of included dykes. Horizontal scales of fluctuation below $\theta_h = 4$ m

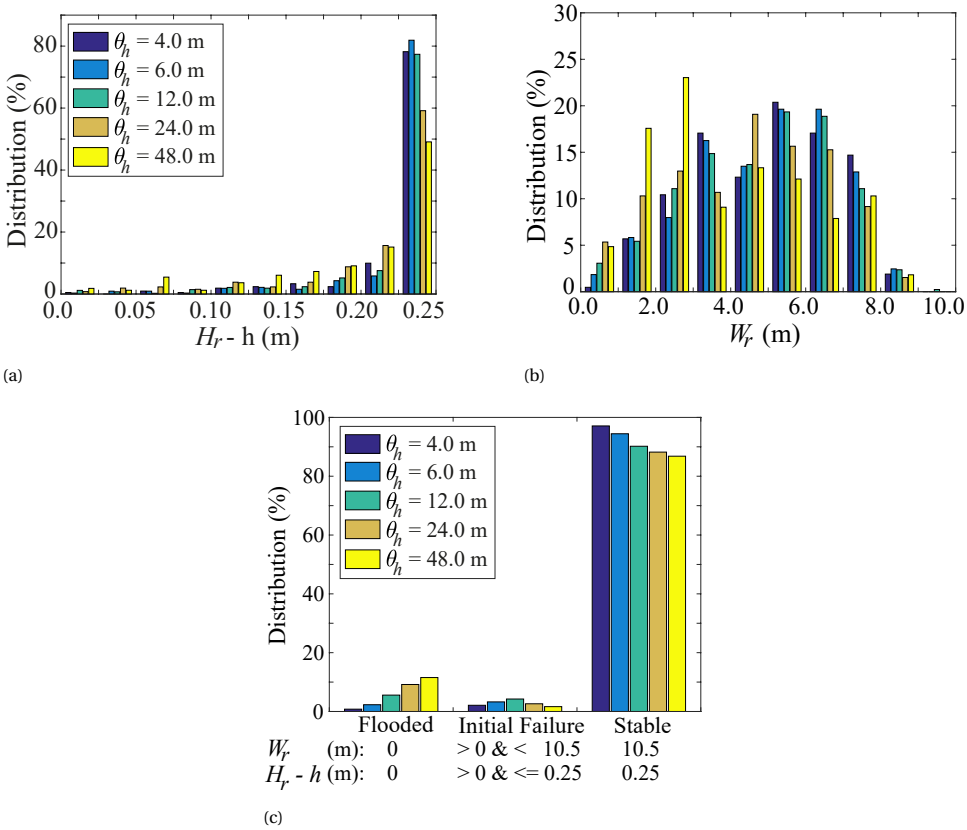

Figure 5.9: a) Histograms of the residual geometry for several horizontal scales of fluctuation, expressed as a) height above the water level ($H_r - h$), b) dyke width at the water level W_r, and c) indication of excluded and included realisations.

are not presented, because the number of included dykes becomes very small due to the low number of initial failures.

Due to the limited height above the water level of the dyke, most failures with residual dyke resistance, i.e. do not flood, do not affect the height of the dyke ($H_r - h \approx 0.25$ m). Therefore, a peak is visible at $H_r - h \approx 0.25$ m (Figure 5.9a). The average height above the water table $H_r - h$ is slightly higher for smaller θ_h, i.e. 0.22 m for $\theta_h = 4$ m against 0.20 m for $\theta_h = 48$ m. The residual width tends to be smaller with larger θ_h (Figure 5.9b). The approximately bi-model nature of the histograms of residual width are the result of the expected size of the initial and retrogressive failures. Since rotational failures are most likely and significantly influenced by depth (due to the depth-independent statistics) the initial failure mechanism is most likely to result in W_r between 4 and 8 m. Secondary (i.e. retrogressive) failures further reduce W_r to roughly 2–3 m. Secondary failures are more likely for larger horizontal scales of fluctuation, i.e. the peaks for larger horizontal scales of fluctuation are located slightly more to the left in Figure 5.9b.

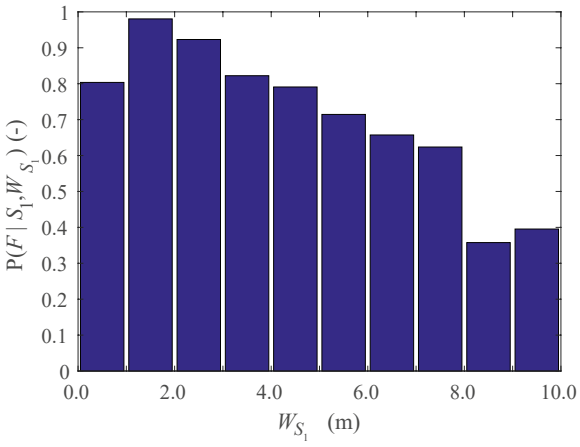

Figure 5.10: Histogram of the probability of flooding given initial failure, i.e. residual dyke resistance, as a function of the width of the initial failure.

Guidelines (e.g. Blinde et al., 2018; ENW, 2009; MIM, 2016) sometimes positively correlate the dyke width after initial failure (W_{S_1}) with residual dyke resistance, i.e. the probability of flooding is reduced (compared to the probability of initial failure) or nullified for large W_{S_1}. The results of all simulations with sufficient results ($\theta_h \geq 4$ m) have been combined in Figure 5.10 (again, stable dykes have been excluded from this figure), which shows the distribution of probability of flooding for a given W_{S_1}, i.e. $P(F|S_1, W_{S_1})$. A negative correlation between the remaining width after initial failure and the probability of flooding is present, suggesting that the reduction in the probability of flooding (compared to the probability of initial failure) based on W_{S_1} according to the guidelines makes sense. However, even though the positive correlation between W_{S_1} and residual dyke resistance is clear, flooding can still be possible after initial failure even at high W_{S_1}. Therefore, guidelines which specify a 'safe' remaining geometry, i.e. $P(F|S_1, W_{S_1}) = 0$ for W_{S_1} larger than a specified minimum, seem risky, especially when the mechanisms after initial failure are not yet fully understood. However, note that the likelihood of flooding after initial failure is heavily influenced by the adopted strength and softening properties, and by larger horizontal scales of fluctuation (which are more prominent in Figure 5.10), as well as by the geometry of the dyke, and it is probably much lower in practice. 'Safe' remaining dyke geometries cannot be justified with simple guidelines, i.e. without modelling the entire failure process the probability of flooding cannot be reduced to 0. Smaller $P(F|S_1, W_{S_1})$ than computed herein are expected in reality, especially for small horizontal scales of fluctuation. Further research is needed to develop guidelines for user practice.

5.4.3. ANALYSIS SET 3: EFFECT OF WATER LEVEL

The effect of different external water levels, i.e. Analysis set 3, is presented in Figures 5.11 - 5.13. At first, the probability of initial failure reduces as the pressure on the dyke de-

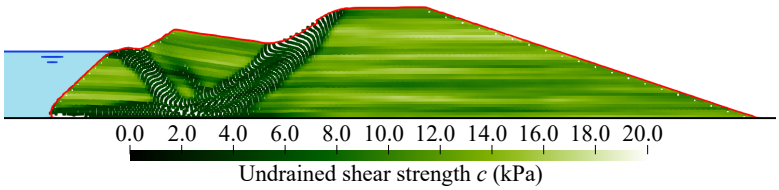

Figure 5.11: Realisation from Analysis set 3 showing the final deformed position, with material points coloured according to the undrained shear strength (c), with an outer slope failure due to a lower water level ($H_i - h$ = 2 m). The red line is the detected boundary and the black line is the fixed boundary. The water level is indicatively shown.

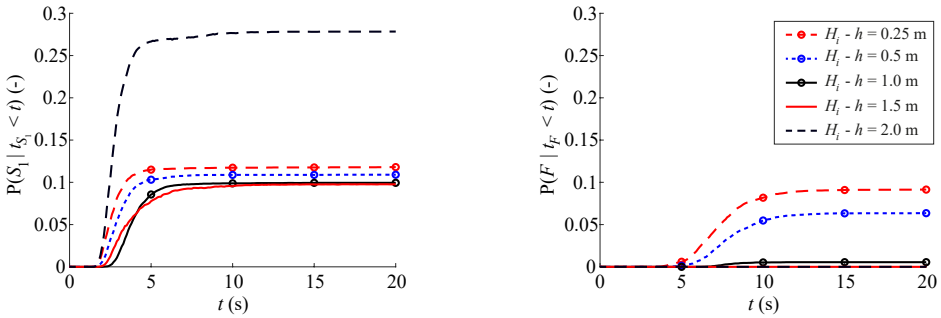

(a) (b)

Figure 5.12: Probability of failure before a given time for various water levels ($H_i - h$); a) initial failure mechanism; b) flooding.

creases ($0.25 \leq H_i - h \leq 1.0$ m, Figure 5.12a). However, once the water level reduces further, outward slope failure, as shown in Figure 5.11, becomes more likely and the probability of initial failure increases. Of course, outward slope failure can be prevented by using a more gentle slope. The initiation time of the outward slope failure in this study seems to be faster in most cases than for inward slope failure, probably due to a smaller failed volume.

The initial width of the dyke W_i is larger for lower water levels and, therefore, for a larger width, more or larger (retrogressive) failures are necessary to trigger flooding. Moreover, the crest of the dyke needs to settle further to trigger flooding for lower water levels. Consequently, the probability of flooding is comparatively lower for lower water levels (Figures 5.12b and 5.13). Fragility curves would therefore be useful for the macro-instability failure category, as this would inherently take into account the lower probability of flooding at lower water levels, thereby reducing the over-conservatism.

Analysis set 3 assumes a constant water level for each set of realisations, thereby ignoring that an outward slope failure due to a period of low water, followed by a period of high water, can still be dangerous if the required repair works have not yet been performed.

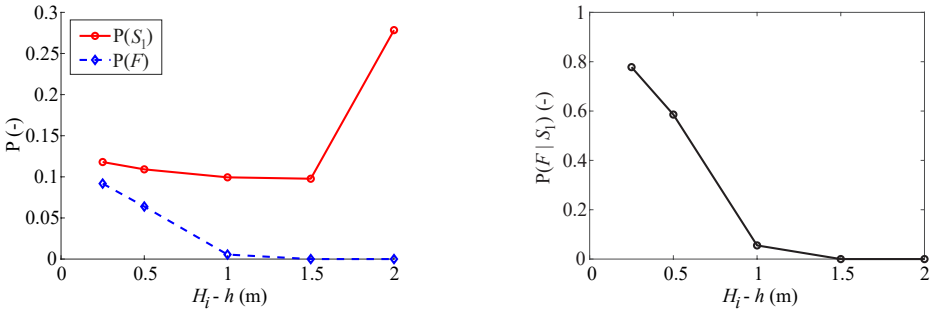

(a) (b)

Figure 5.13: a) Probability of initial failure and flooding and b) probability of flooding given the probability of initial failure for various water levels ($H_i - h$).

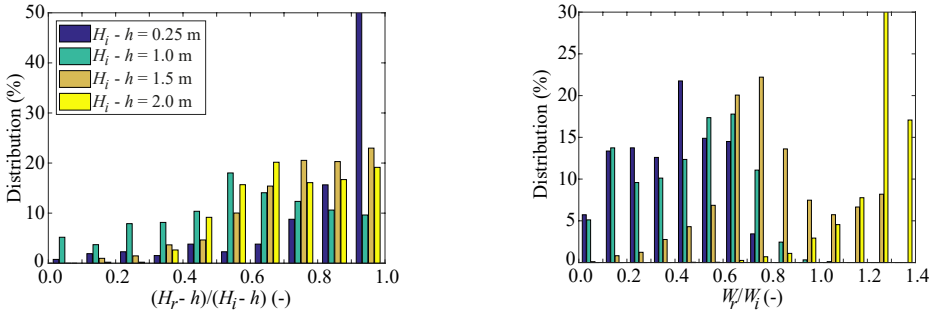

(a) (b)

Figure 5.14: a) Histograms of the residual geometry for various outer water levels in terms of a) height above the water level ($H_r - h$) and b) dyke width at the water level (W_r).

RESIDUAL DYKE GEOMETRY

Figure 5.14 shows the distributions of the residual geometry for the various water levels; once again, the histograms exclude completely stable dykes and flooded dykes, and have been normalised. The horizontal axes show the residual geometry normalised with respect to the initial geometry. In general, an $H_i - h$ of 1.5 m or more offers less initial resistance than an $H_i - h$ of 1.0 m or lower, due to a switch in the dominant failure mechanism from inner to outer slope failure. However, Figure 5.14 shows that a decrease in water level increases the residual resistance, due to the fact that the crest can settle more without triggering flooding (Figure 5.14a), and the remaining width at the water level is larger (Figure 5.14b). Moreover, Figure 5.14b shows that the width of the dyke at the water level may actually increase, due to outward slope failure, causing a further increase in the residual resistance.

5.5. CONCLUSIONS

The probabilistic framework for ultimate limit state (ULS) dyke failure, i.e. flooding, has been implemented and an example analysis presented. The Random Material Point Method (RMPM), a numerical method capable of simulating the full failure mechanism and the effect of spatial variability of the material properties, has been used to investigate the residual resistance of an idealised dyke cross-section. This method accounts for the influence of weaker zones on dyke stability, and it therefore leads to an increased probability of initial failure, and consequently to an increased probability of flooding, compared to standard MPM based on mean strengths.

The residual dyke resistance is relatively small in the illustrated example, i.e. $P(F|S_1)$ = 0.75 or a reduction in the probability of flooding of 25%, due in part to the chosen softening parameters. This is especially so for materials with layered spatial variability, where a weak layer which triggers a primary mechanism is also likely to trigger secondary mechanisms, i.e. retrogressive failure. For materials with limited layering of the spatial variability ($\theta_h \leq 2$ m), the residual dyke resistance increases significantly, resulting in $P(F|S_1) < 0.2$ (the probability of flooding decreases by more than 80%).

RMPM agrees with existing guidelines which increase residual dyke resistance for smaller initial failures. However, the RMPM analyses do not present a 'safe' remaining geometry, i.e. without modelling the failure process it is impossible to predict that flooding will not occur for a given remaining geometry. If guidelines predict the probability of flooding only on the size of the remaining geometry after initial failure, they cannot reduce the probability of flooding to 0. Flooding may still occur due to secondary mechanisms, even if the remaining geometry is large, in part due to the spatial correlation of material properties. Finally, the analyses (Analysis set 3) demonstrate that the water level plays a central role in the dyke assessment, especially for the probability of flooding.

REFERENCES

Bing, Y., Cortis, M., Charlton, T. J., Coombs, W. M., & Augarde, C. E. (2019). B-spline based boundary conditions in the material point method. *Computers and Structures, 212*, 257–274. https://doi.org/10.1016/j.compstruc.2018.11.003

Blinde, J., Bisschop, C., de Visser, M., Jongejan, R., & Tigchelaar, J. (2018). *Afweging ter bepaling glijvlak voor faalmechanisme macrostabiliteit binnenwaarts (translated in English: Consideration for determining failure surface for failure mechanism macro-instability)* (Factsheet). Kennisplatform Risicobenadering.

Calle, E. O. F. (2002). *Dijkdoorbraakprocessen (translated in English: Dijk breach processes)* (tech. rep. CO-720201/39). GeoDelft.

de Gast, T., Vardon, P. J., & Hicks, M. A. (2017). Estimating spatial correlations under man-made structures on soft soils. *Geo-Risk 2017* (pp. 382–389). https://doi.org/10.1061/9780784480717.036

ENW. (2009). *Actuele sterkte van dijken (translated in English: Actual strength of dykes)* (tech. rep.). Expertisenetwerk Water Veiligheid.

Fenton, G. A., & Vanmarcke, E. H. (1990). Simulation of random fields via local average subdivision. *Journal of Engineering Mechanics, 116*(8), 1733–1749. https://doi.org/10.1061/(ASCE)0733-9399(1990)116:8(1733)

González Acosta, J. L., Vardon, P. J., & Hicks, M. A. (2021). Development of an implicit contact technique for the material point method. *Computers and Geotechnics*, *130*, 103859. https://doi.org/10.1016/j.compgeo.2020.103859

González Acosta, J. L., Vardon, P. J., Remmerswaal, G., & Hicks, M. A. (2020). An investigation of stress inaccuracies and proposed solution in the material point method. *Computational Mechanics*, *65*, 555–581. https://doi.org/10.1007/s00466-019-01783-3

Hicks, M. A., Varkey, D., van den Eijnden, A. P., de Gast, T., & Vardon, P. J. (2019). On characteristic values and the reliability-based assessment of dykes. *Georisk: Assessment and Management of Risk for Engineered Systems and Geohazards*, *13*(4), 313–319. https://doi.org/10.1080/17499518.2019.1652918

Huang, J., & Griffiths, D. V. (2015). Determining an appropriate finite element size for modelling the strength of undrained random soils. *Computers and Geotechnics*, *69*, 506–513. https://doi.org/10.1016/j.compgeo.2015.06.020

MIM. (2016). *Schematiseringshandleiding macrostabiliteit (translated in English: Guidelines for schematization of macro-instability)* (tech. rep.). Ministerie van Infrastructuur en Milieu.

Remmerswaal, G. (2017). *Development and implementation of moving boundary conditions in the material point method* (Master's thesis). Delft University of Technology.

't Hart, R., de Bruijn, H., & de Vries, G. (2016). Fenomenologische beschrijving - Faalmechanismen WTI (translated in English: Phenomenological description: Failure mechanisms WTI).

van den Eijnden, A. P., & Hicks, M. A. (2017). Efficient subset simulation for evaluating the modes of improbable slope failure. *Computers and Geotechnics*, *88*, 267–280. https://doi.org/10.1016/j.compgeo.2017.03.010

Vardon, P. J., Liu, K., & Hicks, M. A. (2016). Reduction of slope stability uncertainty based on hydraulic measurement via inverse analysis. *Georisk: Assessment and Management of Risk for Engineered Systems and Geohazards*, *10*(3), 223–240. https://doi.org/10.1080/17499518.2016.1180400

Wang, B., Hicks, M. A., & Vardon, P. J. (2016). Slope failure analysis using the random material point method. *Géotechnique Letters*, *6*(2), 113–118. https://doi.org/10.1680/jgele.16.00019

6

THREE DIMENSIONAL SLOPE FAILURE PROCESSES

Three dimensional effects on the slope failure processes are investigated. A 45 degree slope is brought to failure by either its own weight or by a combination of its own weight and an additional surface load. The ultimate failure load and potential failure processes are studied for various (heterogeneous) material strength properties. In 3D, failures tend to spread sideways and backwards. The resistance against initial and secondary failures in 3D simulations tends to be higher than in 2D simulations, probably due to the additional resistance of the ends of the failure surfaces. The failure behaviour changes when a depth-trend is introduced in the material strength. A depth trend in the material strength triggers a flow-like failure process, instead of (roughly) circular failure surfaces which are encountered in a material without a depth trend in its strength. The flow-like behaviour slowly expands the failure zone in all directions while avoiding (where possible) local strong zones.

6.1. INTRODUCTION

Conventional slope stability assessments are generally performed on 2-dimensional cross-sections. However, it is widely accepted that 2D analyses under predict the safety of the slope due to the resistance at the ends of the failure surface, the so-called '3D-effect', being ignored. Hence, the results of a 3-dimensional assessment of initial slope instability with, for example, the 3D Finite Element Method (FEM), may significantly differ from a 2-dimensional assessment.

3-dimensional models are often too computationally intensive for general practice. Therefore, various analytical procedures which adjust the results of 2D assessments and require little additional computational cost have been proposed. These methods involve an assumed failure surface geometry in the out-of-plane direction to account for the 3D-effect (Chakraborty and Goswami, 2021; Michalowski, 2010; Vanmarcke, 1980; Vanmarcke, 1977). These approaches have, for example, been successful in the back-calculation of the factor of safety of a full-scale dyke failure test (Lengkeek, 2022). The method proposed by Vanmarcke (1977) has recently been compared against the Random Finite Element Method (RFEM) (Hicks and Li, 2018; Li et al., 2015; Varkey et al., 2017). Compared to RFEM, Vanmarcke's method overestimates the end resistance and does not account for the effect of weak zones. Varkey et al. (2019) modified Vanmarcke's method to improve its performance relative to RFEM.

Similar to an initial slope instability, the results of an assessment of the complete failure process may change if a 3-dimensional model is used. The analytical procedures for the 3D-effect of the initial failure process are likely to be not valid for the complete failure process. Therefore, 3-dimensional failure processes are here investigated with the 3D Random Material Point Method (RMPM). Failure processes in 3D are generally more complex than those in 2D. For example, 3D failures may be able to avoid local strong zones more easily compared to 2D failures, thereby reducing the resistance against secondary failures. Avoiding these strong zones can make the shape of the failure process more complex. In 3-dimensions, the resistance against secondary failures may also be increased by the ends of the failure surfaces, similar to the 3D-effect for initial failures.

This chapter provides a first insight into 3-dimensional slope failure processes. A range of failure processes for an idealised problem are presented, together with distributions of the resisted failure load and the failure size. The effects of spatial variability of shear strength properties, as well as a depth-trend in the mean shear strength properties, on the failure process are studied.

6.2. DESCRIPTION OF THE EXAMPLE PROBLEM

An idealised 1 m high, 45 degree slope, shown in Figure 6.1, is modelled in 3-dimensions using DM-G, i.e. double-mapping using GIMP shape functions. The effect of volumetric locking is reduced with the B-bar approach, which has also been applied in FEM (Zheng et al., 2022). The occurrence of an inherent instability, i.e. a slope being unstable under its own weight, is studied. When the slope is stable, a foundation load is applied until failure is triggered. This ensures that each slope is brought to failure, and thereby minimises the overhead in computing realisations without failure.

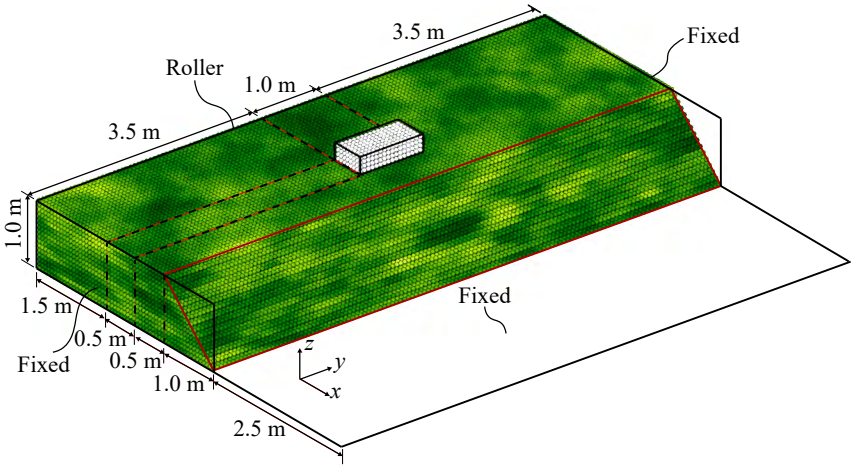

Figure 6.1: Geometry of the problem, indicating the loaded area (with white material points). The material points are coloured according to the undrained shear strength and indicate a random field with θ_v = 0.25 m, θ_h = 1.25 m and COV = 0.25.

The slope is 8 m long (L) and has a crest width of 2.5 m (W_c). Cubic 8-noded finite elements, with a size of 0.125 m in each Cartesian direction, are used as the background grid. The elements are filled with 2 x 2 x 2 material points evenly distributed within each element. Along the slope face, two material points have been removed from the x-z corner of each element, so that the slope surface cuts through the material point support domain in a manner similar to that for the 2D, 45° slope in Chapter 3. In other words, when viewing a cross-section of the slope, material has been removed from the top right of the elements to form the slope geometry. The relatively low number of elements, i.e. 8 elements in the vertical direction, has been used to reduce computational costs to enable Monte-Carlo simulations with a reasonable number of realisations.

A random field is generated with cubic cells of 0.0625 m, such that each cell corresponds to the initial volume occupied by 1 material point. The same random field is applied for the peak and residual undrained shear strengths, i.e. these properties are fully correlated. All other properties are considered to be deterministic. The base and ends of the problem domain are fixed in all directions, while the $y-z$ face at the back of the domain prevents movement in the x-direction, see Figure 6.1. The fixity at the end of the domain does not provide vertical resistance when a failure occurs at or near the boundary, i.e. the estimated strength is conservative. In the x-direction, the computational domain extends 2.5 m beyond the toe of the slope, and no fixity is used on the $y-z$ face at the front of the domain. Material points are removed from the simulation once they exit the domain. Moreover, the $x-z$ faces are free boundaries beyond the toe of the slope. Material points can therefore also leave the domain through the $x-z$ faces beyond the toe. The effect of removing material points is small, since the material loses most of its strength before it reaches these boundaries.

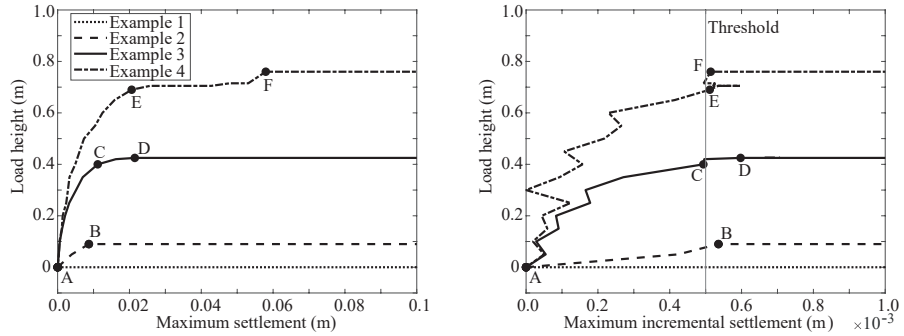

Figure 6.2: The loading scheme of four example realisations. The load height as a function of a) maximum settlement, and b) maximum incremental settlement. Note that the results are plotted every 10 time steps.

The analyses use the same constitutive model as presented in Chapter 5 to represent the clay slope, with a mean peak cohesion (μ_{c_i}) of 3.6 kPa, a mean residual cohesion of 0.36 kPa, i.e. giving a sensistivity S_c = 10, and a softening modulus of 2 kPa. The unit weight of the material is 20 kN/m^3, and the elastic behaviour is governed by a Young's modulus of 1000 kPa and a Poisson's ratio of 0.45.

For the base case, i.e. Analysis 1, the random fields of peak and undrained shear strength are generated with a *COV* of 0.25, together with vertical and horizontal scales of fluctuation of θ_v = 0.25 m and θ_h = 1.25 m, respectively. The probability distributions of undrained shear strength have (similar to Chapter 5) been truncated to prevent negative strengths. One realisation of this base case is illustrated in Figure 6.1. The effects of variations in the *COV* and horizontal scale of fluctuation, studied after the base case, are explained in Section 6.2.2. Each Monte Carlo analysis comprises 300 realisations, and failure is triggered in all realisations, either under the slope's self weight (i.e. the slope is inherently unstable), or due to the application of a foundation load as described below.

6.2.1. LOADING SCHEME

Implicit dynamic MPM is used with 0.01 second time steps. Gravity loading is applied in an elastic implicit quasi-static MPM step to generate 99% of the initial (i.e. in situ) stresses. In this step, movement of the material points and plasticity are prevented. The remaining 1% is applied at the start of the simulation, where movement and plasticity of the material points are allowed, which may trigger an inherent instability. For cases in which the slope is stable under its own weight, an increasing load is applied to the foundation by increasing the weight of the material points representing the foundation. This load represents the build-up of material on top of a 1 m long by 0.5 m wide area, located 0.5 m from the slope crest.

In each time step, an additional load equivalent to 0.005 m depth of soil is applied, unless the incremental settlement in the previous time step exceeded a threshold of 0.0005 m (in which case, no increment of load is applied). The incremental settlement threshold is used to prevent overloading of the slope beyond its actual failure capacity.

The incremental settlement of material points is comparable to the velocity of the material points; hence the load is only increased when the velocity is low. An incremental settlement threshold is used instead of a total settlement threshold, since the total settlement can vary significantly when the failure load is reached (see Figure 6.2a).

The load scheme is further explained by the examples shown in Figure 6.2. The slope in Example 1 is inherently unstable and the maximum incremental settlement exceeds the threshold without the application of a foundation load. During the analysis, the displacement increased far beyond the 0.1 m limit of Figure 6.2a. In Example 2, the load is increased from point A until the failure capacity is reached at point B. From point B the maximum incremental settlement continuously exceeds the threshold.

In Example 3, the load is increased from points A to C. Loading is paused at C because the maximum incremental settlement in the previous step exceeded the threshold. In other words, the velocity of the slope was too high. However, the failure capacity has not yet been reached at point C, i.e. the incremental settlement decreases with time under the same load and, without a further load increase, the slope becomes stable before large deformations can occur. Between C and D, the foundation load is increased whenever the incremental settlement in the previous step is below the threshold. So, whenever the material points slow down enough, additional load is applied, until the failure capacity is reached after which material points continuously accelerate up to large deformations (point D of Example 3).

A similar behaviour is observed in Example 4, where the load is increased continuously until point E. At this load, the incremental settlement increased significantly beyond the threshold. However, the incremental settlement decreased again in later time steps, i.e. the failure capacity was not yet reached at point E. The load is then increased whenever the material points slow down to below the threshold until reaching the failure capacity at point F.

When the sliding mass slows down during the failure process, the incremental settlement decreases again. Figure 6.2b has been cut off once the initial failure has fully developed, and the decrease of incremental settlement is not shown. To prevent further loading after an initial failure has occurred, loading is no longer increased once the maximum total settlement exceeds 0.1 m. Secondary failures can still occur after the initial failure without further loading.

Table 6.1: Model details.

Geometry	**Discretisation**	**Material Properties**	
H = 1 m	Δt = 0.01 s	γ = 20 kN/m^3	$c_i = \mathrm{N}(\mu_{ci}, COV)$
W = 2.5 m	t_{max} = 15 s	E = 1000 kPa	$c_r = c_i / S_c$
L = 8.0 m	Δx = 0.125 m	ν = 0.45	S_c = 10
Slope 1:1	Δy = 0.125 m	H_S = -2 kPa	θ_v = 0.25 m
	Δz = 0.125 m		0.25 m < θ_h < 10.0 m

Table 6.2: Summary of analyses. Note that Analyses 2A, 3B and 4A match Analysis 1: Base case).

Analysis	Comments	μ_{c_i} (kPa)	COV (-)	θ_h (m)	k (kPa/m)
1	Base case	3.6	0.25	1.25	0
2A	Point statistics	3.6	0.25	1.25	0
2B		3.4	0.25	1.25	0
2B		3.6	0.1	1.25	0
3A	Horizontal scale of fluctuation	3.6	0.25	0.25	0
3B		3.6	0.25	1.25	0
3C		3.6	0.25	2.5	0
3D		3.6	0.25	5.0	0
3E		3.6	0.25	10.0	0
4A	Depth trend in mean shear strength	3.6	0.25	1.25	0
4B		3.6	0.25	1.25	1.5
4C		3.6	0.25	1.25	3.0

6.2.2. OVERVIEW OF ANALYSES

The failure process for select realisations are highlighted in Section 6.3 for the base case, for which the properties have been described in the previous sections and are summarised in Table 6.1 and Table 6.2. In Analysis sets 2 to 4, the point statistics, horizontal scale of fluctuation and depth trend of the mean undrained shear strength have been varied, see Table 6.2. The failure processes for the base case are compared against results obtained for the other analysis sets. In addition, for the base case, the failure capacity and size of the failure are compared against a 2D simulation of the cross-section along the centre line using the same random field.

Analysis set 2 compares histograms of failure capacity and failure size between the base case and analyses with a change in the point statistics, i.e. with a) a lower mean undrained shear strength (μ_{c_i}), and b) a lower coefficient of variation (COV). Analysis set 3 describes the failure process for extreme values of the horizontal scale of fluctuation. The histograms of failure capacity and failure size are then used to interpret the results for intermediate values of the horizontal scale of fluctuation, i.e. varying the degree of anisotropy in the range ξ = 1, 5, 10, 20 and 40. Finally, in Analysis set 4, a linear depth-trend k in the mean undrained shear strength is introduced, i.e. in this case the mean undrained shear strength increases linearly with depth. The results of the base case without a depth trend, i.e. k = 0 kPa/m, are compared against k = 1.5 kPa/m and 3.0 kPa/m. The depth average of the undrained shear strength is the same in all analyses as shown in Figure 6.3.

6.2.3. QUANTIFYING THE FAILURE VOLUME

In the post-processing of their RFEM analyses, van den Eijnden and Hicks (2017) separated the stable material from the unstable material using the K-means cluster method (KMCM) to estimate slide volumes. This approach has here been modified for RMPM. In RFEM, two clusters are enough to separate the sliding mass from the stable mass (i.e. the sliding mass is one cluster and the stable mass is the other cluster). However, in MPM, the large difference in deformations between the initial and secondary failures causes

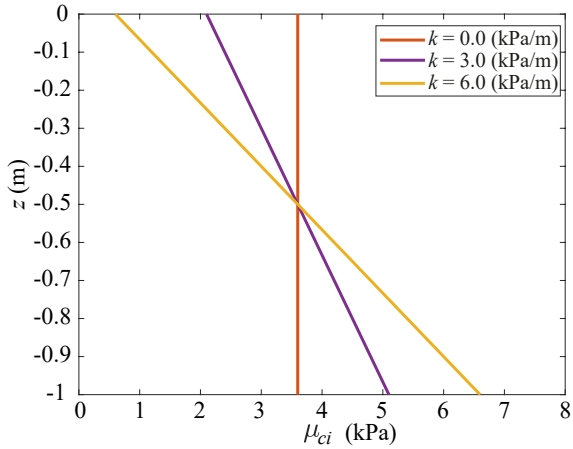

Figure 6.3: Mean undrained shear strength at a given depth as a function of the depth trend k.

the clustering with two clusters to become unstable, as secondary failures may be clustered with the stable material instead of with the sliding mass.

KMCM is, therefore, not used during post processing at the end of the simulation, but instead used during the simulation whenever an initial or subsequent failure occurs. At the start of the simulation one stable cluster exists. When a failure occurs, KMCM separates the failure mass from the stable mass (i.e. the cluster containing the stable mass is split into two new clusters: a new sliding mass and a new stable mass). When KMCM is used again later in the analyses, only the remaining stable mass is split into new clusters. So, during the analyses the size of the stable cluster reduces as more unstable clusters are detected. Meanwhile, the number of unstable clusters gradually increases. The unstable clusters, i.e. clusters with sliding masses, remain unchanged once formed.

To detect if a failure has occurred, i.e. to detect when KMCM should be used to create a new sliding mass, the maximum euclidean displacement of the remaining stable material points ($u_{stable,max}$) is computed. Failure is deemed to have occurred whenever $u_{stable,max}$ exceeds a (user-defined) threshold, here set to be 0.2 m. The threshold $u_{stable,max} > 0.2$ m ensures an accurate division of each failure for this problem, and has been established based on visual inspection of several realisations.

By the end of the simulation, the material may have been divided into any number of clusters. Each cluster contains either the stable mass, the sliding mass of the initial failure, or the sliding mass of a subsequent failure. The clusters are used to estimate 1) the stable volume, 2) the failure volumes, 3) the retrogression distance (in the x-direction), and 4) the damaged crest width (in the y-direction). The retrogression distance is defined as the largest distance from the crest until a stable material point, whereas the damaged crest width is defined as the total width (in the y-direction) of all failed crest material points. The modified KMCM procedure can also be used to compute the failure volumes of individual slides, but these results are not discussed here.

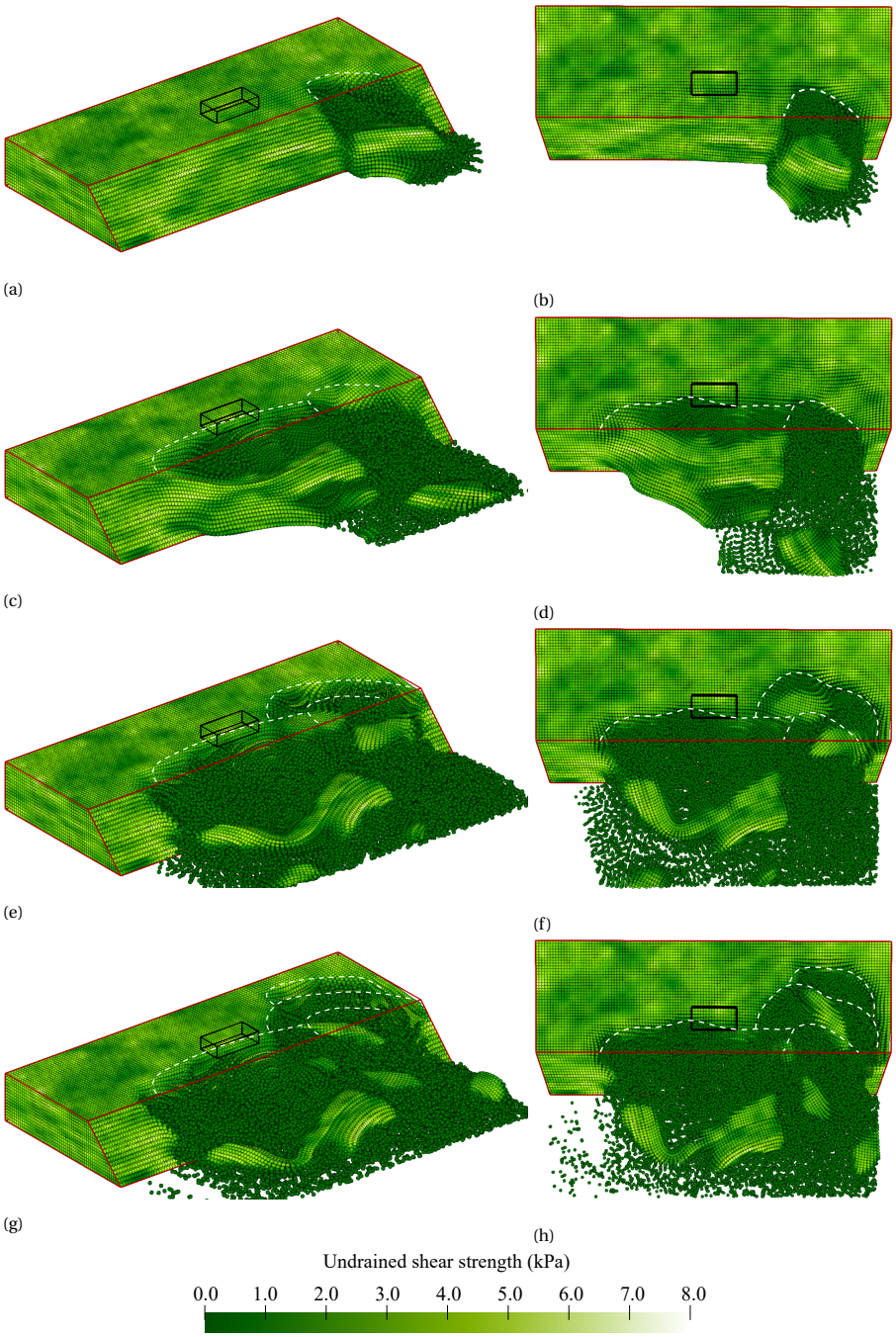

Figure 6.4: An inherently unstable slope failure: a and b) small initial failure; c and d) sidewards spreading of the failure; e and f) large retrogression backwards; g and h) end of the simulation.

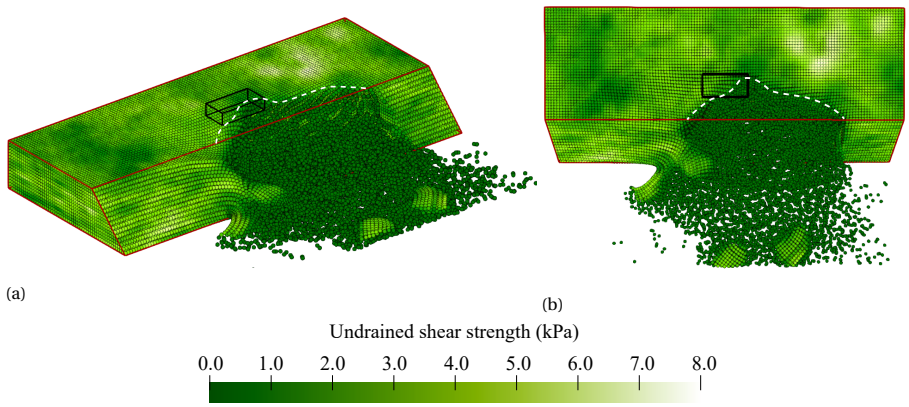

Figure 6.5: A large inherently unstable slope failure without retrogressive failures.

6.3. ANALYSIS 1: BASE CASE

6.3.1. FAILURE PROCESSES OF INHERENTLY UNSTABLE SLOPES

Some of the slopes are inherently unstable due to a weak zone within the slope (10.4% of the slopes in Analysis 1). In these cases, the response of the inherently unstable slope is studied instead of the response to a foundation load. An example of this behaviour is shown in Figure 6.4, where the material points are presented in their displaced positions and are coloured according to the undrained shear strength of the material, i.e. strong zones are lighter and weak zones are darker. The outline of the undeformed slope is highlighted in red and the centrally located surface load at the slope crest, which is not applied in this simulation, is highlighted in black. Ridge lines are indicatively drawn as white dashed lines to highlight the location of each failure surface wth respect to the original slope crest. For each (selected) time step, 3-dimensional and top views are presented.

Figures 6.4a and 6.4b show the same small initial failure of roughly 2 meters in width near the far end of the slope, i.e. the centre line of the failure is located around 6.5 m from the left-hand boundary. In Figure 6.4a a 3D view of the slope and failure is shown, whereas in Figure 6.4b the top view is shown. In Chapter 5, two-dimensional retrogressive behaviour was shown after the initial dyke failure, and a similar behaviour can be observed in 3D. The initial failure triggers a large instability along the remainder of the slope, as seen in Figures 6.4c and 6.4d. This second instability is limited by the presence of a strong zone at the toe of the slope between 1.0 m and 2.0 m from the left-hand boundary. The initial failure also triggers retrogressive behaviour towards the back of the slope. First, a third slide with a size roughly equal to the initial failure occurs, as shown in Figures 6.4e and 6.4f. Then, a smaller fourth slide can be observed in Figures 6.4g and 6.4h. The fixed end point of the simulation after 15 seconds has been reached in Figures 6.4g and 6.4h. By this end point the deformations have slowed down and it is therefore unlikely that additional failures would occur if the simulation was continued beyond 15 seconds.

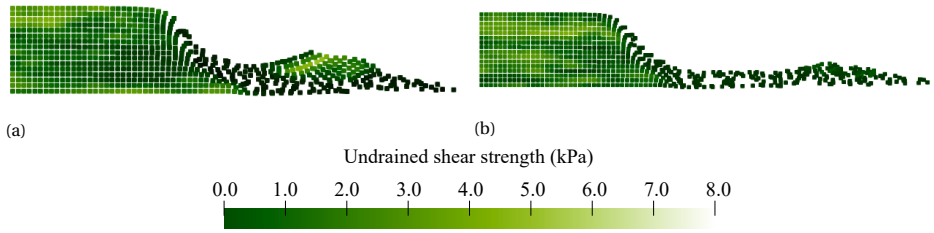

Figure 6.6: a) Cross-section through the centre line of the failure in Figure 6.4 and b) cross-section through the centre line of the failure in Figure 6.5.

Figure 6.4 highlights the importance of modelling the failure process in 3D, in that the failure process is clearly 3-dimensional. The importance of 3D modelling becomes clearer when comparing Figure 6.4 against Figure 6.5. Both figures show a bowl-shaped failure mechanism, but Figure 6.5 shows a wider initial failure (3.5 m in Figure 6.5 against 2.0 m in Figure 6.4). Moreover, the failure occurs at a different location along the slope, such that the centre lines of the slope failures in Figures 6.4 and 6.5 are located at 6.5 and 5.0 m from the left-hand boundary, respectively. The failure in Figure 6.4a may also be influenced by the fixity at the side of the domain reducing the size of the initial failure mechanism. The differences between Figures 6.4 and 6.5 are caused by different locations of weak zones affecting the resistance to slope failure.

Based on the size of the initial failure one would assign the largest consequence to the failure in Figure 6.5. However, due to the fact that secondary failures are triggered in Figure 6.4 and not in Figure 6.5, the consequence of the failure in Figure 6.4 is significantly larger. This highlights the importance of modelling the failure process when the failure consequence is to be determined, i.e. 3-dimensional small deformation models (such as RFEM) may not be sufficient.

For cross-sections at the centre lines of the 3D failures (Figure 6.6), a nearly identical circular failure through the base of the slope is observed, which exits the ground surface at around 0.7 m from the slope crest. This 2D failure surface is expected due to the chosen slope geometry and undrained shear strength statistics being constant with depth, which favour an approximately circular failure mechanism through or near the slope toe. So, a 2D simulation could incorrectly suggest similar behaviour when 3D-effects are ignored, especially when the failure process is modelled.

6.3.2. FAILURE PROCESSES TRIGGERED BY A FOUNDATION LOAD

Most of the slope simulations are stable under their own weight (89.6% of the slopes in Analysis 1). The surface load is then applied to trigger slope failure, with an example illustrated in Figure 6.7. The fixed location of the surface load at the centre of the slope fixes the location of the failure initiation along the slope, i.e. failure must initiate near the load. However, the size of failure may vary. Figures 6.7a and 6.7b show that in this case a 6-meter-wide initial failure occurred, which has a bowl-shape similar to the inherently unstable failures shown in Figures 6.4 and 6.5.

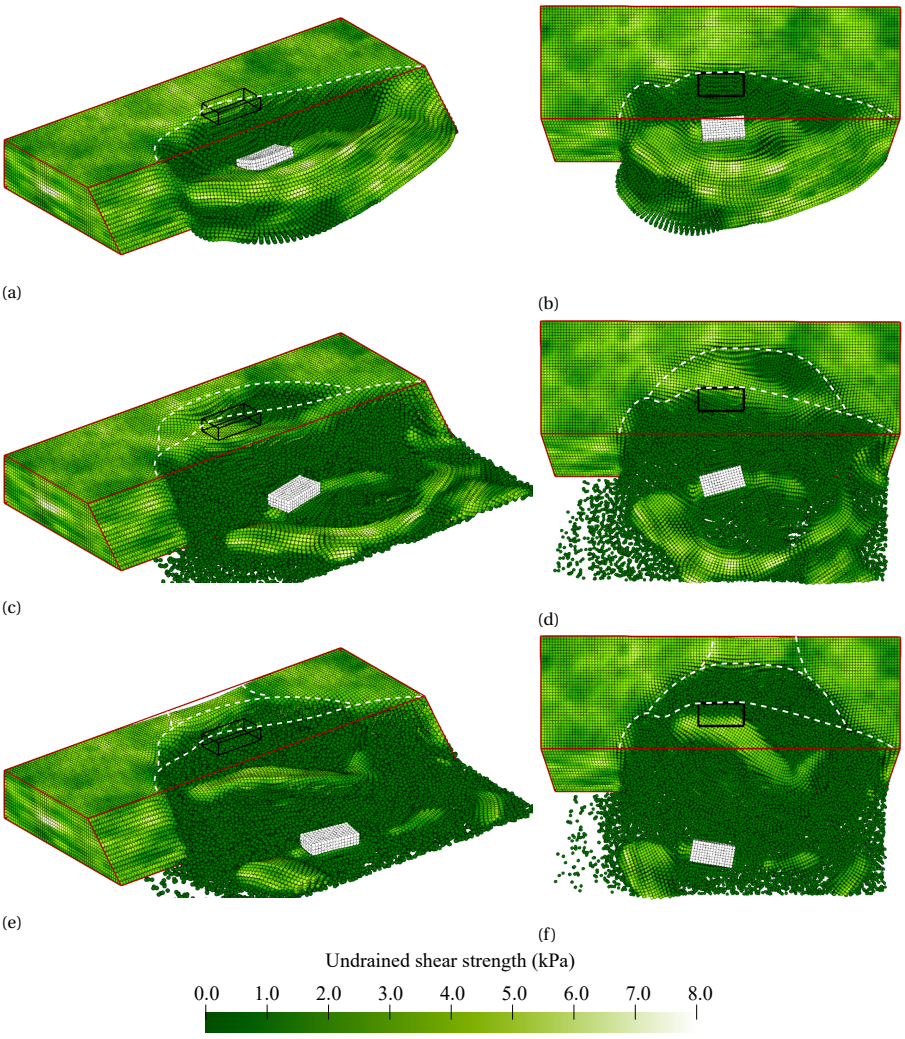

Figure 6.7: A slope failure due to the applied foundation load: a and b) large slightly asymmetric initial failure; c and d) backwards retrogressive failure; e and f) retrogressive failure fully developed and a third deformation zone initiates at the back of the slope before the end of the simulation.

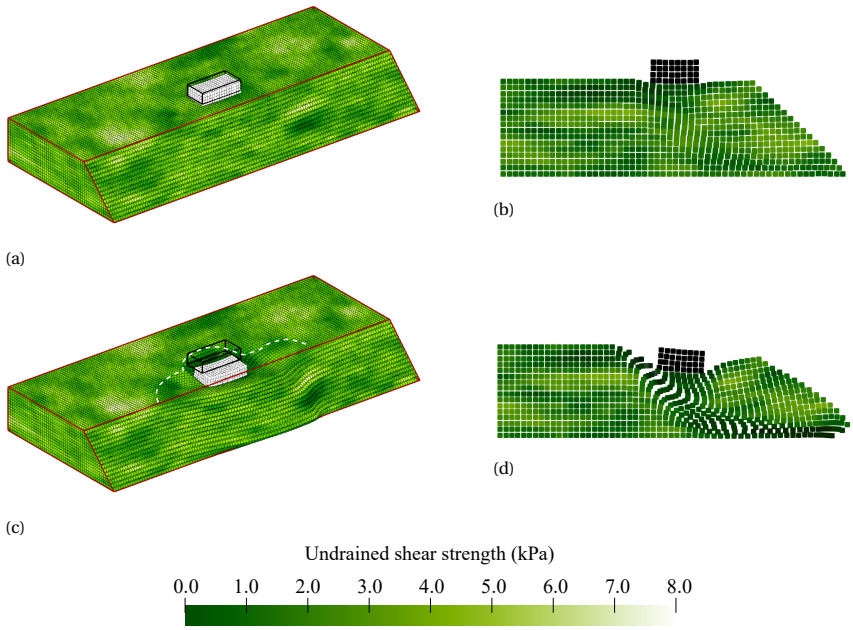

Figure 6.8: Slope failure during bearing capacity failure: a and c) 3D views of the failure process; b and d) cross section along the centre line of the slope; a and b) local deformation under the load while slope failure develops; b and c) bearing capacity and slope failure both further develop.

The initial slide is followed by a slightly smaller secondary slide, see Figures 6.7c and 6.7d. The first slide initiated below the surface load and triggered an asymmetric failure (i.e. a larger failure to the right of the load than to the left). The second slide initiates 1 m to the right of the location of the load, i.e. it follows the asymmetric geometry of the first failure. By the end of the simulation (Figures 6.7e and 6.7f) the second failure has spread to become roughly the same width as the initial failure, and a small third failure has initiated in the remainder of the slope towards the fixed boundary, i.e. the slope height at the fixed boundary has fallen, as is evident in Figure 6.7e.

The use of a surface load as the trigger reduces the variation in the location of failure initiation. However, more variation in the subsequent failure process can be observed. For example, local deformations around the load, similar to bearing capacity failure may occur, see Figures 6.8a and 6.8b. Here, complete slope failure is prevented until a high foundation load is reached, resulting in local deformation under the loaded area. A further increase in load triggers slope failure before a full bearing capacity failure as shown in Figures 6.8c and 6.8d. The cross-section in Figure 6.8d shows that the slope failure surface tends to cut the crest at the edge of the surface load, i.e. approximately 1 m from the slope crest. After Figures 6.8c and 6.8d, the slope failure further develops (not shown in the figure), although no retrogressive behaviour occurs.

A large variation in the failure width is possible even when a surface load is applied, as shown in Figure 6.9. The surface load can trigger failure along the entire width of the slope when the slope is barely stable under its own weight and the strength of the

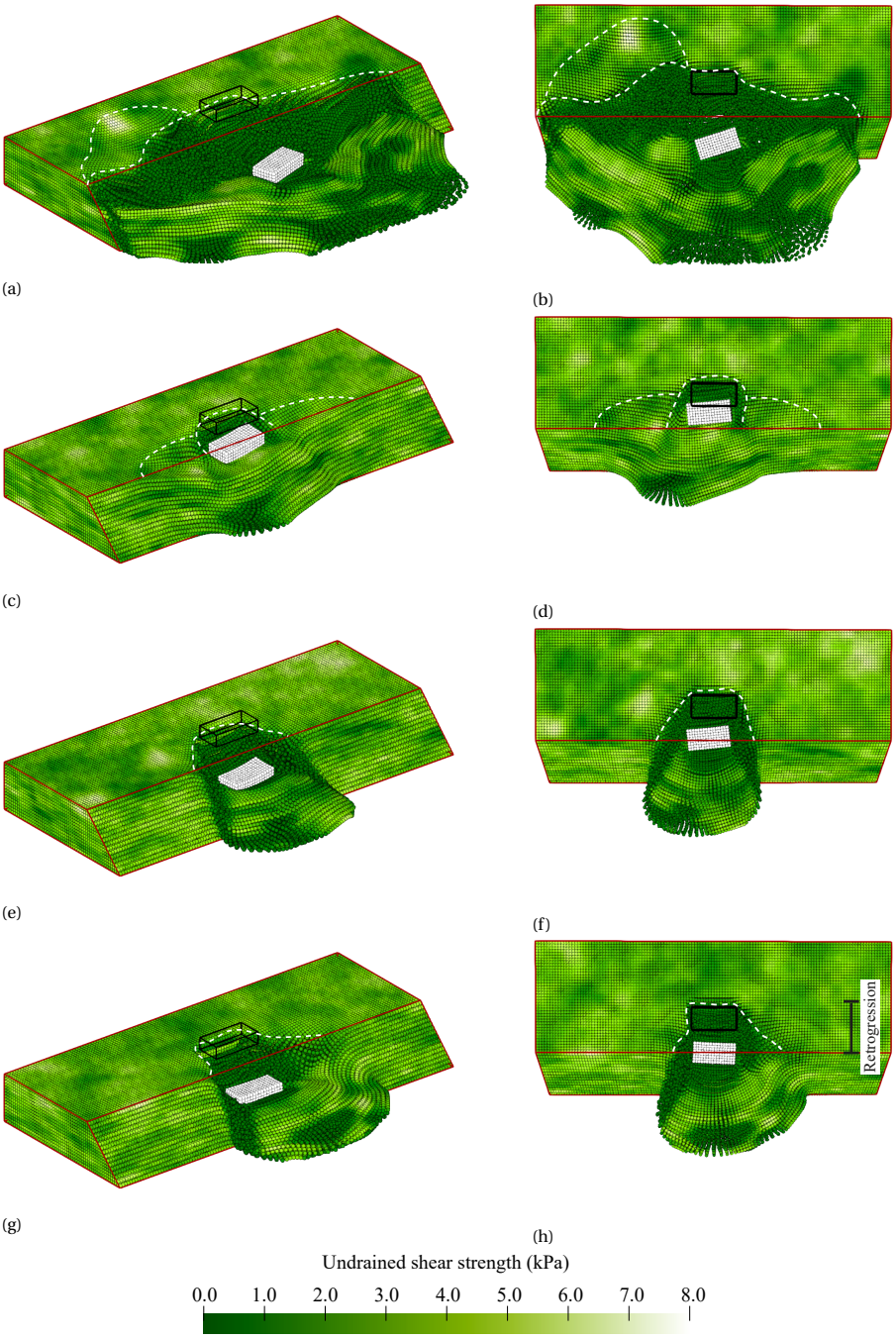

Figure 6.9: Various possible initial failures due to a foundation load: a and b) failure width roughly the slope width; c and d) failure width roughly half the slope width; e and f) failure width roughly equal to surface load width; d and h) asymmetric failure surfaces bounded by strong zone on 1 side of the surface load.

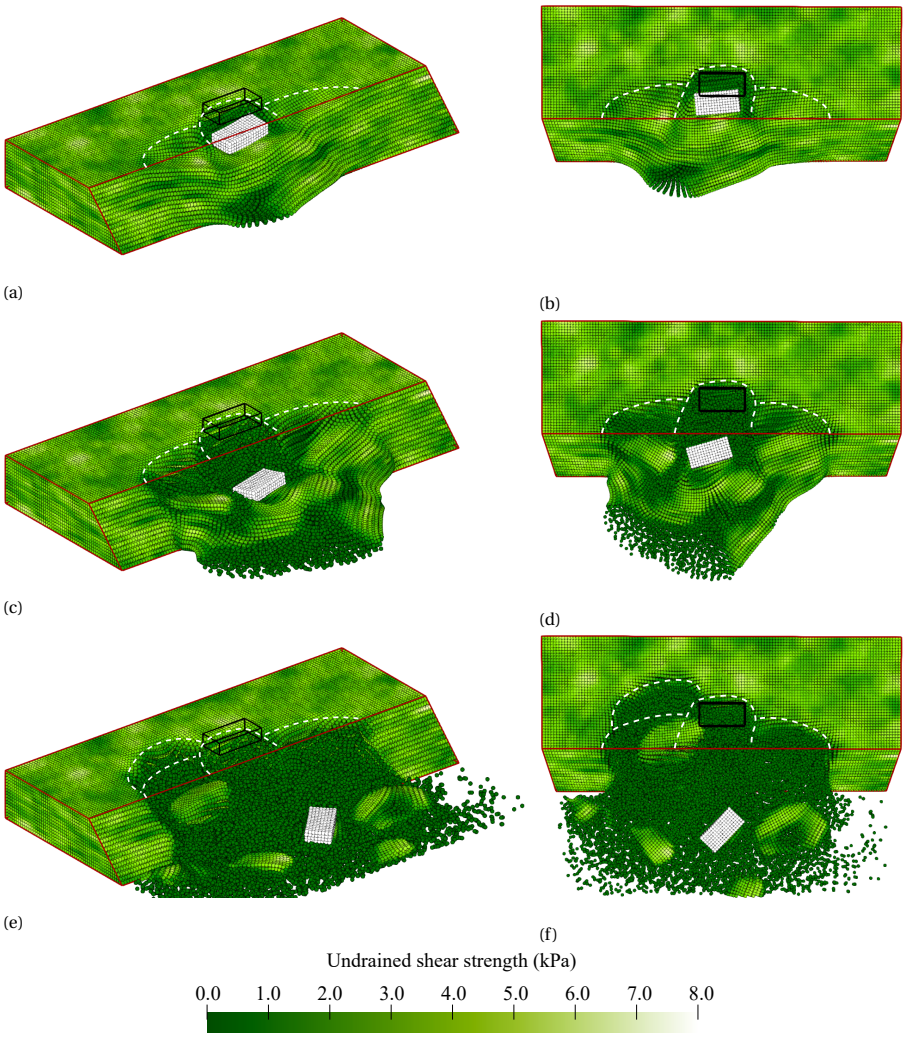

Figure 6.10: A failure process predominantly parallel to the slope after the initial failure shown in Figure 6.9c: a and b) initial failure; c and d) lateral extension of the initial failure; e and f) smaller retrogressive slide can be observed at the end of the simulation.

material is roughly constant along the entire slope (Figures 6.9a and 6.9b). However, stronger zones usually occur along the slope width. The failure surface extent can then be reduced significantly, to, for example, half the width of the slope (Figures 6.9c and 6.9d) or even the width of the surface load (Figures 6.9e and 6.9f). When strong zones are only present on one side of the surface load, an asymmetric failure as shown in Figures 6.9g and 6.9h can be triggered.

Although Figure 6.7 showed retrogressive behaviour mainly towards the back of the domain, retrogressive behaviour can move in many directions in 3D simulations. For example, Figure 6.10 shows the failure process after the initial failure shown in Figures 6.9c and 6.9d. During the initial failure, the sides of the initial failure are pulled with the moving material, thereby widening the failure. The locations where these widening failures cut the crest are usually slightly closer to the slope compared to the initial failure, since these failures are no longer triggered by the surface load. Figure 6.7 shows large retrogressive failures, with a size similar to the original width. However, it is more usual for smaller blocks on the sides or back walls of the failed area to become unstable, as can be seen in Figures 6.10e and 6.10f. They slide into the failure zone, and flow out of the gap created by the initial failure in the case when further deformation occurs. In this specific case, the inertia of the block is not large enough for it to flow out of the domain, and it instead remains in the failure zone. Secondary failures in the corners of the failure zone are often small, while secondary failures in the middle of the failure zone tend to be larger as observed in Figure 6.7.

After an initial failure with a smaller width, such as the asymmetric failure shown in Figure 6.9g, a third and less likely failure process may occur: retrogressive failures may form a small tunnel from the gap created by the initial failure away from the slope face. The tunnel shown in Figure 6.11 tends to get smaller with each subsequent failure. Not all of the material can flow out of the tunnel, as the material still has some undrained shear strength and rests on a horizontal fixed boundary. This remaining material has a stabilising effect, which causes the tunnel to narrow. However, one may expect instabilities in the sides of the tunnel when 1) the material is capable of flowing out, or 2) when the sides of the tunnel have a weak zone. The chance of encountering a weak zone would increase were the tunnel able to progress further beyond the back boundary included in this model.

6.3.3. ULTIMATE FOUNDATION LOAD

While the previous sections give an overview of the range of behaviours observed in Analysis 1, Figure 6.12 shows the distribution of foundation loads for all the realisations of Analysis 1. The load heights are placed into bins of 0.2 m in height, where the label in the figure indicates the average value. The first bin contains load heights from 0.0 to 0.1 m in height, but is centered on 0.0 as it mainly contains the realisations with zero load height, i.e. 10.4% of the 3D slopes are inherently unstable. A wide spread around the deterministic results (i.e. based on mean property values) is observed, where some slopes are unable to resist their own self-weight (foundation load of 0 m) while others can resist a foundation load equivalent to more than the slope height.

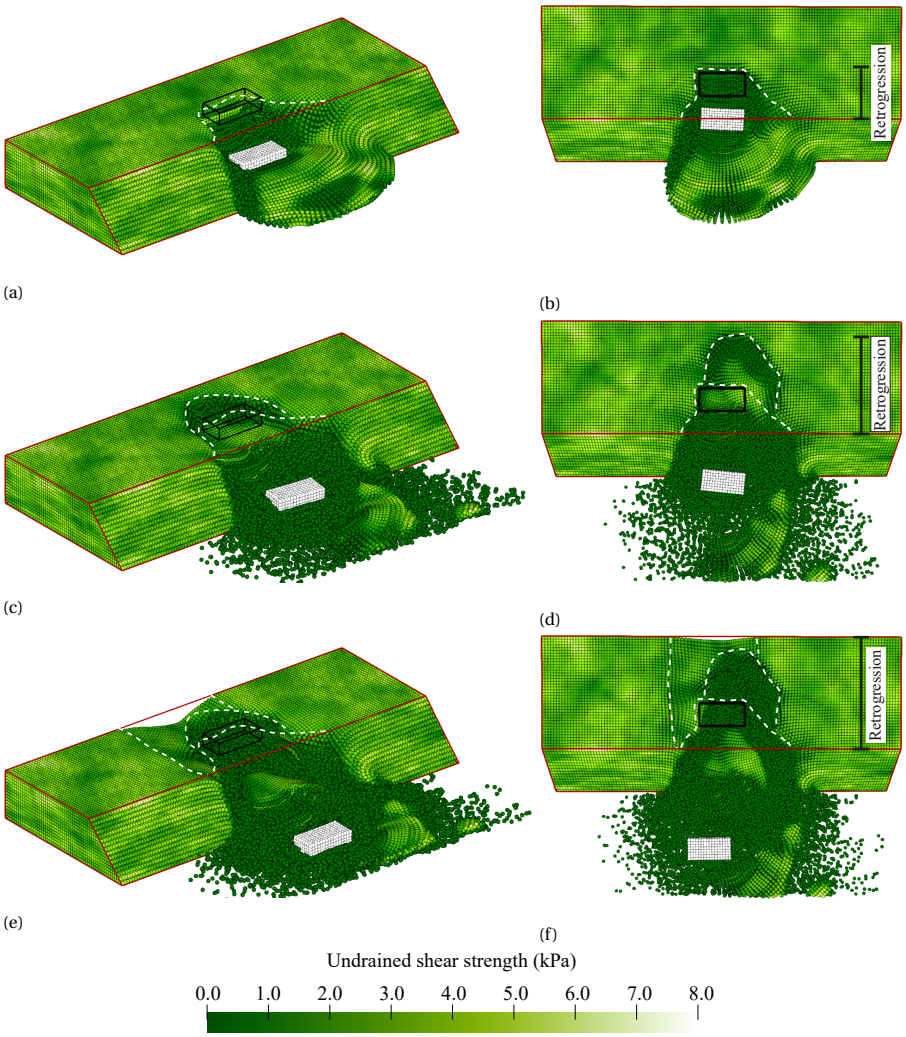

Figure 6.11: Mostly backwards failure process after the initial failure shown in Figure 6.9g: a and b) initial failure; c and d) retrogressive failure in a tunnel like shape; e and f) end of the simulation. The progression of the retrogression distance is indicated.

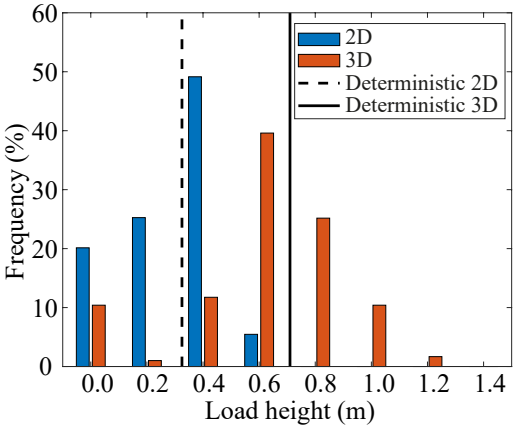

Figure 6.12: Distribution of the ultimate foundation load, represented as the height of soil built up on the foundation for Analysis 1. Comparative 2D simulations using the same statistics are also presented.

For comparison, 2D simulations were performed for the cross-section through the middle of the slope. The 2D simulations use the same random fields, i.e. from each 3D random field the centre cross-section was selected and used to perform the 2D analysis. In 2D, more slopes are inherently unstable (20.1% in 2D compared to 10.4% in 3D) and the resisted load is significantly lower on average. So, the fact that a failure in 3D can occur at more potential weak locations is more than compensated for by the stabilising effect of the sides of a failure surface in 3D for the considered slope geometry and material properties.

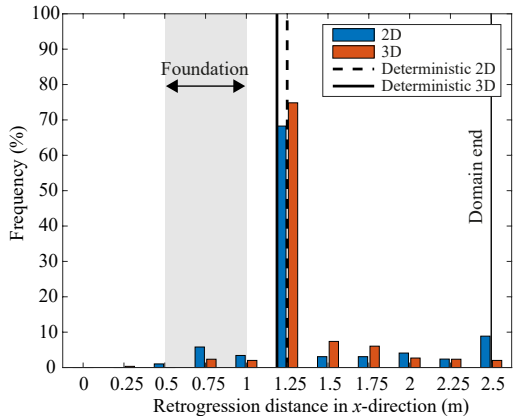

Figure 6.13: Distribution of the retrogression distance, the largest distance from the initial slope crest to the failure surface (measured along the crest) for Analysis 1. Comparative 2D simulations using the same statistics are also presented.

6.3.4. FAILURE PROCESS

Figure 6.13 shows the final retrogressive distance, measured from the crest in the x-direction as indicated in Figure 6.11, in Analysis 1. It shows that retrogressive behaviour in the x-direction, i.e. away from the crest, is unlikely, since in most simulations the retrogressive distance is limited to the location at which the load is applied, i.e. is the result of a single failure. Moreover, in some cases an inherently unstable slope failure does not even reach this distance. This local peak at roughly 0.8 m caused by inherently unstable slopes is especially visible in the 2D simulations, as more inherently unstable slopes are present (see Figure 6.12). Even though retrogressive behaviour is unlikely, when it occurs it can significantly increase the damage to the slope, potentially even reaching the end of the domain at 2.5 m. When retrogressive behaviour occurs in 2D, it is more severe compared to 3D. This indicates that the stabilising 3-dimensional effects also significantly affect retrogressive behaviour. The stabilising effect also compensates for more potential failure paths in 3D. Even though a 2D simulation may miss 3-dimensional processes, it is likely to be a conservative estimate of retrogression distance.

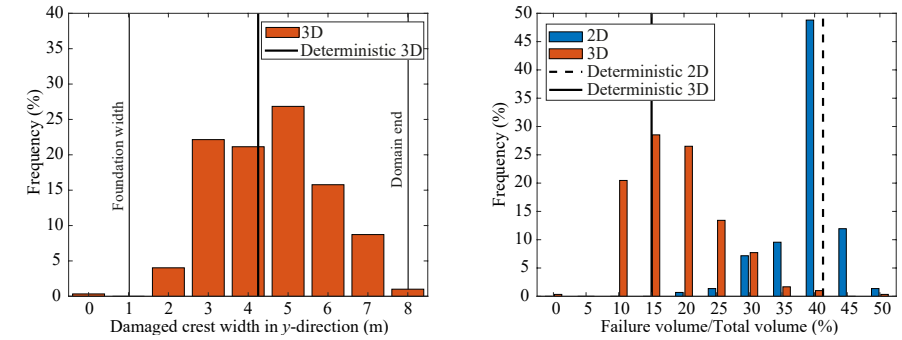

Figure 6.14: a) Damaged crest width for Analysis 1 and b) relative failure volume for Analysis 1.

Figure 6.14a shows that much more variation is present in the failure process in the y-direction (parallel to the slope). A deterministic analysis computes a failure width of roughly 4.2 m, i.e. roughly 4 times the slope height and width of the foundation load. Moreover, the deterministic analysis often under predicts the failure width. As shown in Figure 6.10, slope failures can spread in the direction parallel to the slope, and this can in some cases cause the entire width of the crest to be damaged (see Figure 6.14a). Figure 6.14b shows that a 3D deterministic outcome can incorrectly underestimate the failure volume of a specific realisation by a factor 2 to 3. The failure volume of the 2D simulations has also been computed, where failure is assumed to occur along the entire width of the 3D domain. This is a conservative assumption, given the fact that in reality, the failures modelled in 2D would have a limited width in the 3rd dimension. The 2D analysis significantly over predicts the failure volume under this assumption, with a higher peak at around the deterministic solution. For visibility, the figure is limited to a relative failure volume of 50% (of the domain volume), although 20% of the 2D simulations have a relative failure volume above 50%, with a more or less uniform distribution from 50%

to 100% relative failure volume. This again indicates that retrogressive behaviour is more extensive in 2D analyses.

6.4. ANALYSIS SET 2: VARIATIONS IN POINT STATISTICS

6.4.1. LOWER MEAN UNDRAINED SHEAR STRENGTH

Figures 6.15 and 6.16 present the behaviour of Analysis 2A and Analysis 2B, i.e. the same slope, loaded under the same conditions, with a lower mean undrained shear strength (μ_{c_i} = 3.4 kPa) and the same *COV* of 0.25. The lower strength resists, as expected, a lower load while experiencing increased damage due to the failure process. As for the base case, the average resisted load is lower than the deterministic simulation based upon the mean. The small decrease in mean undrained shear strength has tripled the number of inherent instabilities, which highlights that, due to soil heterogeneity, the slope presented in Section 6.3 is close to inherent failure. In both deterministic solutions retrogressive behaviour does not occur. However, a lower mean undrained shear strength triggers more retrogressive failures when soil heterogeneity is considered, see Figure 6.15b. Additionally, as shown in Figure 6.16 the damaged crest width, and thereby the failure volume, tend to increase significantly for a lower mean strength, resulting in many more simulations where the entire crest width is damaged.

6.4.2. LOWER COEFFICIENT OF VARIATION

A reduction of *COV* from 0.25 to 0.1 (Analysis 2C) reduces the variation around the deterministic outcome for both the onset and process of failure, as shown in Figure 6.17. A lower variation increases the strength of the material in the weak zones, while decreasing the strength in the stronger zones. Since the average strength along the failure surface is mainly governed by the strength of the weaker zones, the average strength along the failure surface increases with a decreasing coefficient of variation. This causes an increase in the expected load height to trigger failure, as indicated in Figure 6.17a. Additionally, as the weaker zones are stronger, the failure volume tends to be smaller (see Figure 6.17b).

6.5. ANALYSIS SET 3: HORIZONTAL SCALE OF FLUCTUATION

Figure 6.18 shows a realisation with a degree of anisotropy equal to 1 (such that θ_h = θ_v = 0.25 m), i.e. a realisation from Analysis 3A. The failure initiation is quite similar to Figure 6.11, where the width of failure at the load is roughly equal to the 1 m width of the loaded area and expands to 2 to 3 meters wide at the base of the slope. The initial failure in Figures 6.18a and 6.18b is slightly asymmetric with the right-hand side failing before the left-hand side. While Figure 6.11 shows an example which occurs infrequently in the base case, failures with a small width such as the one in Figure 6.18 occur with a higher frequency for low degrees of anisotropy, as the outcomes approach the deterministic solution. After the initial failure, due to the high variation within the soil the material breaks into smaller blocks compared to the examples of the base case shown in Section 6.3. This results in a more chaotic remaining profile, see Figures 6.18e and 6.18f, while smoother profiles are observed in the base case.

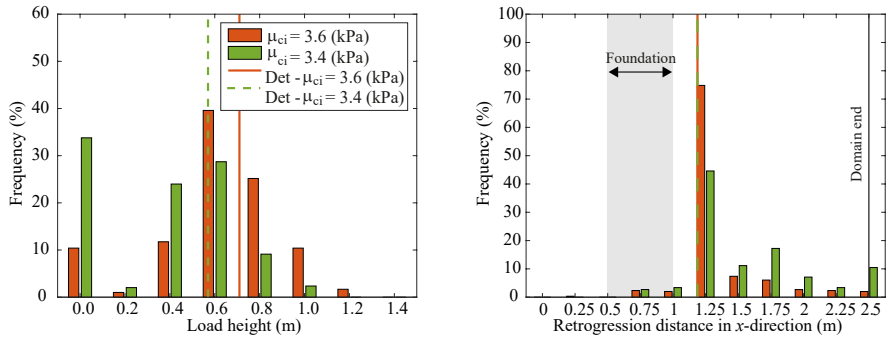

(a) (b)

Figure 6.15: a) Load height and b) retrogression distance for Analysis 2A and 2B: Two cases with different mean undrained shear strengths (μ_{c_i} = 3.6 kPa and 3.4 kPa).

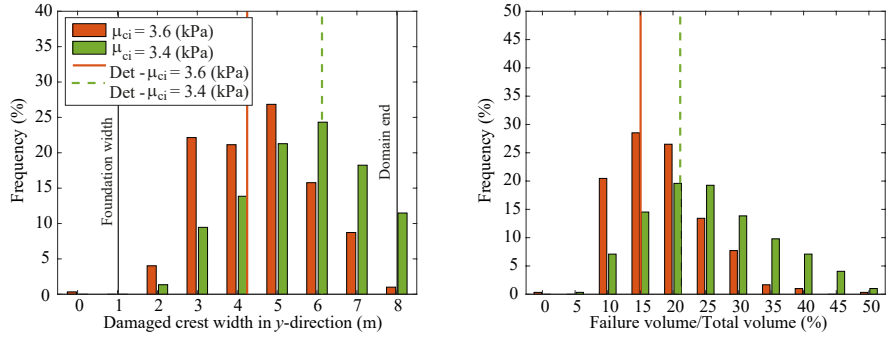

(a) (b)

Figure 6.16: a) Damaged crest width and b) relative failure volume for Analysis 2A and Analysis 2B: Two cases with different mean undrained shear strengths (μ_{c_i} = 3.6 kPa and 3.4 kPa).

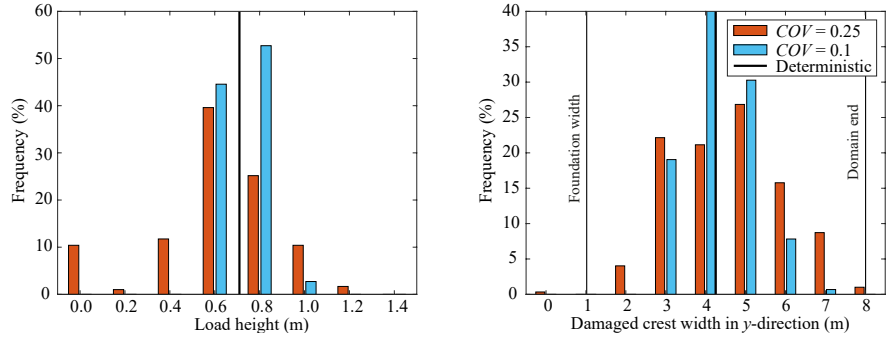

(a) (b)

Figure 6.17: a) The load height and b) the damaged crest width for a reduction in coefficient of variation (Analysis 2A and Analysis 2C). Note that the deterministic damaged crest width is 4.25 m.

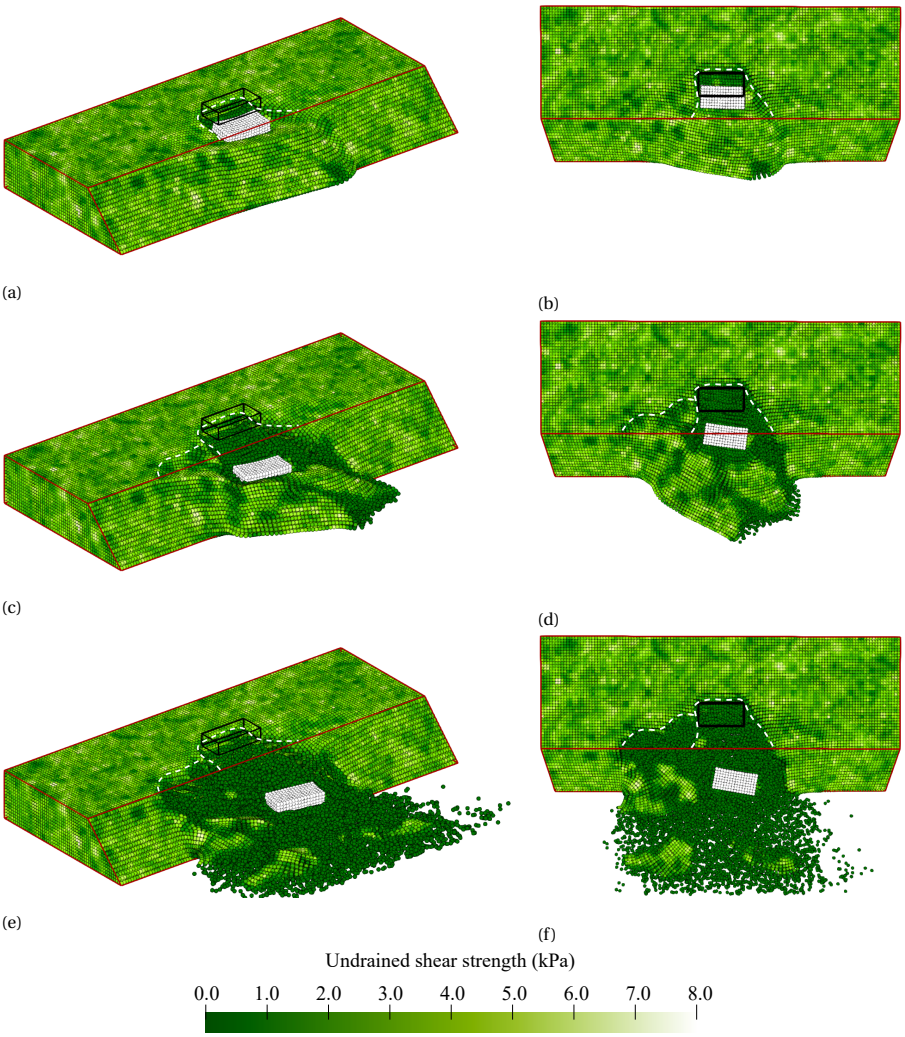

Figure 6.18: Example of a failure with degree of anisotropy (ξ) = 1, i.e. no layering: a and b) small initial failure; c and d) chaotic breaking of the initial failure block; e and f) sidewards secondary failure which breaks into small blocks before the end of the simulation.

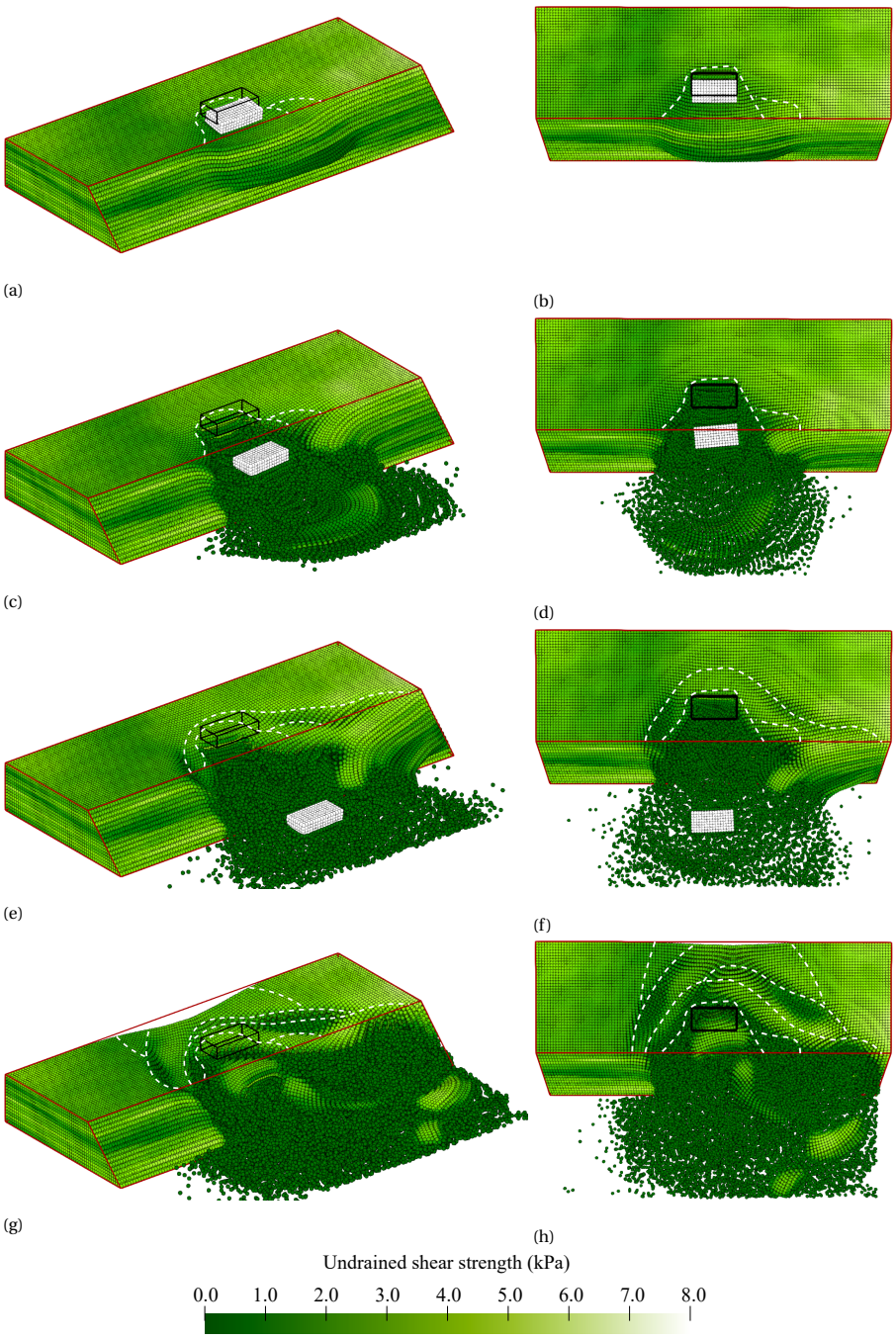

Figure 6.19: Example of a failure with degree of anisotropy (ξ) = 40, i.e. layers more extensive than the length of the slope: a and b) initial failure through a weak layer above the base of the slope; c and d) fully developed initial failure with settlements in a large area around the failure; e and f) lateral and retrogressive secondary failures; g and h) subsequent failures cause an almost complete collapse before the end of the simulation

.

A realisation with a degree of anisotropy of 40 (from Analysis 3E) can trigger failure above the base of the slope as shown in Figure 6.19. Due to a large weak layer, this kind of failure often triggers the almost complete collapse of the slope once failure occurs (as shown in Figures 6.19g and 6.19h). Figures 6.19c and 6.19d show that the initial failure causes settlement in a large area surrounding the foundation, which is quickly followed by a large secondary failure where both the sides and back of the failed area are pulled in with the initial failure. Compared to Figure 6.18, large intact blocks remain in the failure zone, as failure blocks slide down in Figure 6.19. These blocks are usually larger in the y-direction than in the x-directions, as the failure surface perpendicular to the slope still tends to be circular in the x-direction limiting the failure size.

6.5.1. ULTIMATE FOUNDATION LOAD

Figure 6.20 shows the effect of the horizontal scale of fluctuation on the distribution of the ultimate limit load. For a degree of anisotropy of $\xi = 1$, i.e. no layering of the soil heterogeneity, limited variation around the deterministic solution with mean strength properties is observed. The outcome for $\xi = 1$ approaches the results with a lower coefficient of variation shown in Figure 6.17a. This is because significant averaging of the material properties along the failure surface can be expected for this degree of anisotropy for the adopted value of θ_v. Moreover, inherent failures cannot be triggered because the weak zones in the material are too small to promote formation of failure without avoiding the stronger zones.

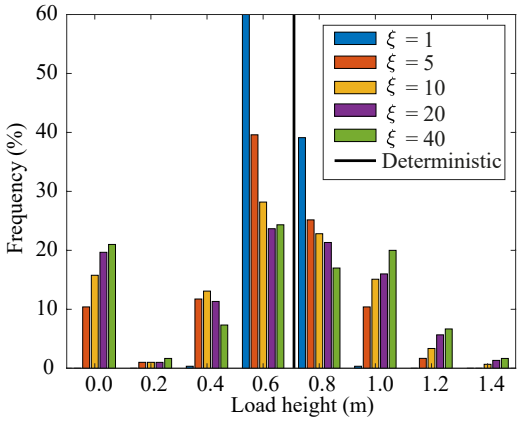

Figure 6.20: Effect of degree of anisotropy (ξ) of the soil heterogeneity on the ultimate foundation load.

At the other end of the spectrum, a degree of anisotropy of $\xi = 40$ shows a large variability in the failure load. In some cases, strong zones are present at the base of the slope where the loads due to gravity loading are the highest, thereby providing the ability to resist a larger failure load. A strong zone can even force failure initiation through a weak layer above the base of the slope, as shown in Figure 6.19. Conversely, a weak zone along the base often triggers an inherent instability.

Intermediate degrees of anisotropy confirm that the influence of strong and weak

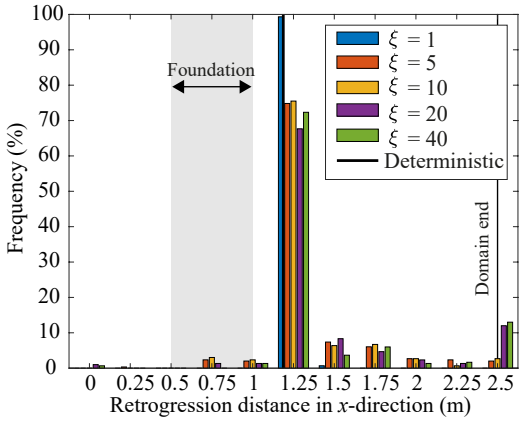

Figure 6.21: Effect of degree of anisotropy (ξ) of the soil heterogeneity on the retrogression distance.

zones increases with an increase in the degree of anisotropy. In other words, larger strong zones can more often increase the resisted load than smaller strong zones, while larger weak zones are more likely to trigger inherent instabilities than smaller weak zones.

6.5.2. FAILURE PROCESS

The variation in the retrogression distance increases with an increase in the degree of anisotropy, as shown in Figure 6.21. As, in many cases, no retrogressive behaviour in the direction away from the slope is observed, the retrogression distance is often governed by the initial failure caused by the surface load. Therefore, a large peak is present between 1 and 1.5 m retrogression distance. A high degree of anisotropy causes more inherent instabilities compared to a low degree of anisotropy. Moreover, retrogressive failure tend to be more likely for higher degrees of anisotropy. Therefore, almost no cases with a retrogression distance below 1 m are observed for large degrees of anisotropy. When retrogressive behaviour occurs with significant layering, the complete slope is likely to collapse, while for lower degrees of anisotropy retrogressive failure often does not reach the back face of the domain.

Finally, Figure 6.22 shows the variation in the damaged crest width and failure volume for the various degrees of anisotropy. Figure 6.22a indicates that strong zones in a layered material can have a limiting effect on the width of the initial failure surface, while retrogressive behaviour through weak zones can trigger full collapse of the slope. The responses for a small amount of layering ($\xi = 5$) and a large amount of layering ($\xi = 40$) are similar, while no layering clearly shows less variation. In the case of no layering ($\xi = 1$), failures tend to have a size much closer to the deterministic solution.

Figure 6.22b shows that the failure volume tends to increase with ξ, since in more cases retrogressive failure occurs and the width of the failures are often larger. Figure 6.22b is limited to 50% relative failure volume, which captures most of the responses. However, for degrees of anisotropy of $\xi = 20$ and $\xi = 40$, approximately 8% and 12% of the results, respectively, lie above 50% relative failure volume.

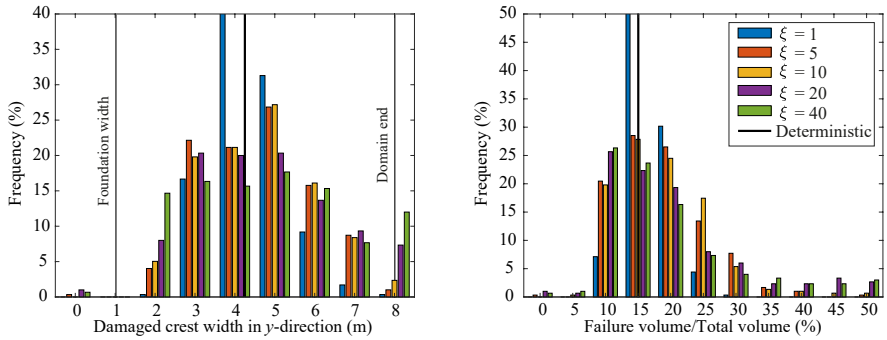

Figure 6.22: a) Damaged crest width for Analysis set 3 and b) relative failure volume for Analysis set 3

6.6. ANALYSIS SET 4: DEPTH TREND IN THE MEAN SHEAR STRENGTH

One example of a failure process with a large depth trend (k = 6.0 (kPa/m)) is shown in Figure 6.23. Figures 6.23a and 6.23b show that the initial failure due to the foundation load occurs through a layer roughly halfway up the slope. Due to the fact that the failure occurs through a higher layer, the size of the failure is small in both the vertical direction and the horizontal direction along the slope (see Figures 6.23c and 6.23e). Compared to a material without a depth trend, retrogressive behaviour does not occur along clear slip planes. Instead, as shown in Figures 6.23e-6.23h, the material appears to flow steadily along a gentle slope into the failure zone. Instabilities at the sides of the initial failure, which tend to occur frequently in materials without a depth trend, are much less frequent in a material with a depth trend, i.e. retrogressive failure occurs more in the direction away from the slope and less along the slope.

Figure 6.24a presents the effect of a depth trend in the mean undrained shear strength on the resisted load. As the strength at the base of the slope, where the loads are the highest, tends to increase with an increase in k to 3.0 kPa/m, the resistance of the slope against inherent instabilities and foundation load increases. However, as k increases further to 6.0 kPa/m, failures along weak zones above the base become increasingly likely, which can reduce the resistance of the slope compared to a smaller k. The likelihood of an inherent instability for a large k can even be higher than the case without a depth trend. In other words, a limited depth trend can raise the resistance, since the higher strengths at greater depths can resist the higher loads, i.e. is beneficial for slope in this step, while a larger depth trend increases the possibility of failures along planes at different depths, thereby reducing the overall resistance.

A similar effect can be observed in the failure process, as shown in Figure 6.24b: a small depth trend reduces retrogressive behaviour, whereas a large depth trend increases retrogressive behaviour.

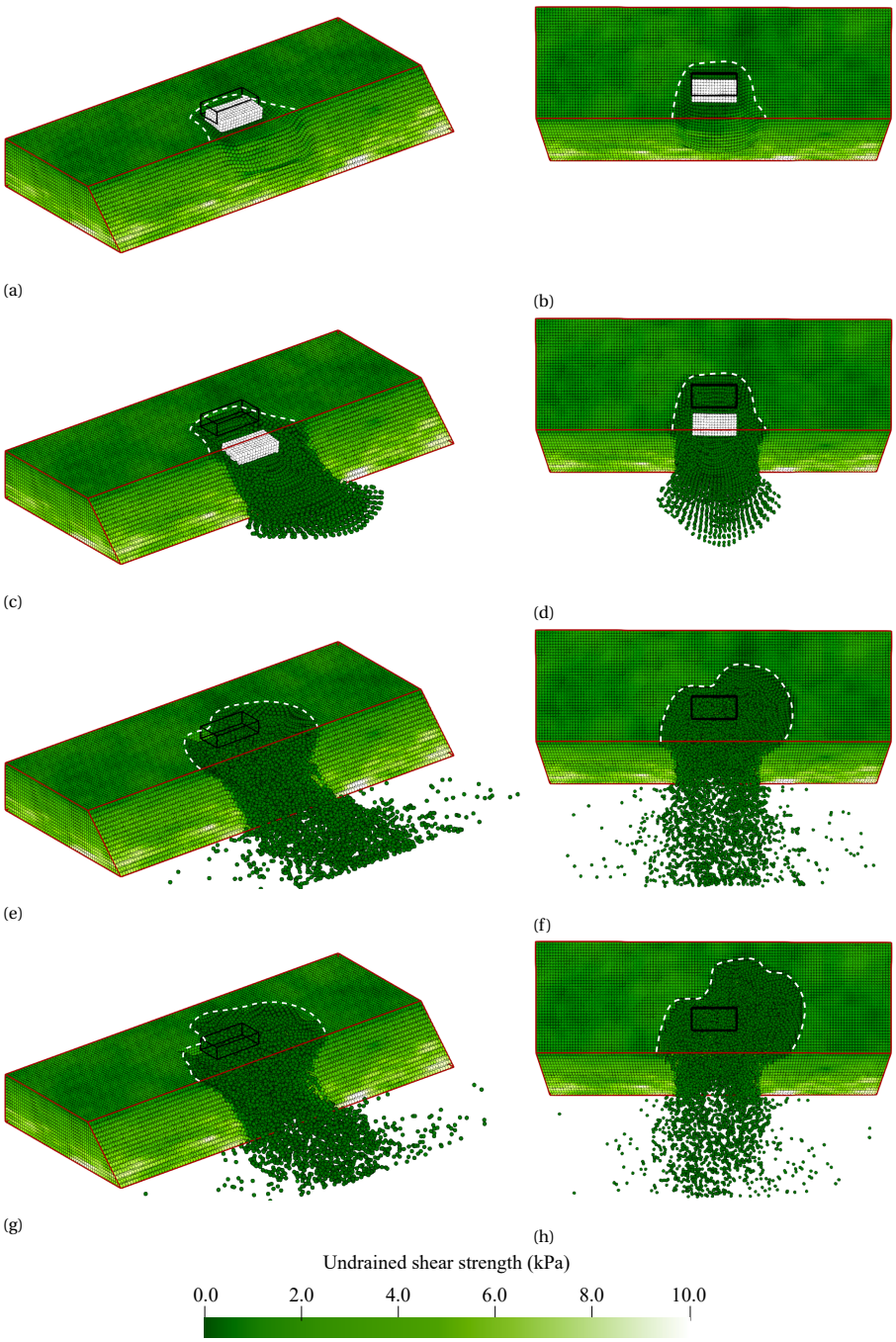

Figure 6.23: Example of a failure with a depth trend k = 6.0 kPa/m in the mean undrained shear strength: a and b) initial failure after loading through a weak zone halfway up the slope; c and d) small fully developed initial failure, where the base of the slope remains stable; e and f) flow like retrogressive behaviour of the weak material at the top of the slope; g and h) end of the simulation after more flow like retrogressive behaviour.

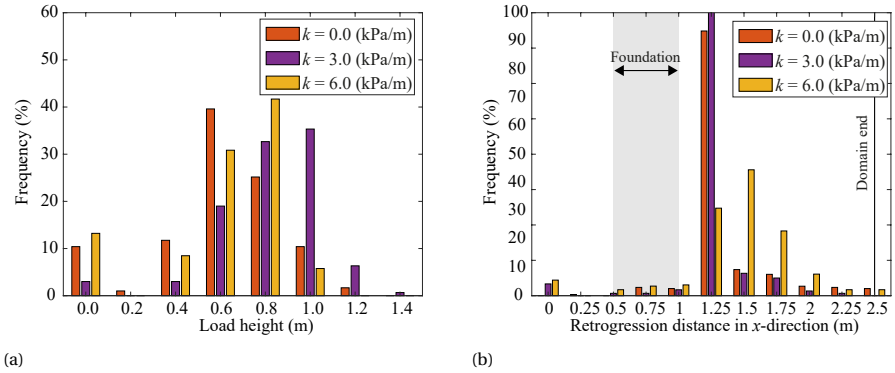

Figure 6.24: a) Load height and b) retrogression distance for Analysis set 4 with and without a depth trend in the mean undrained shear strength.

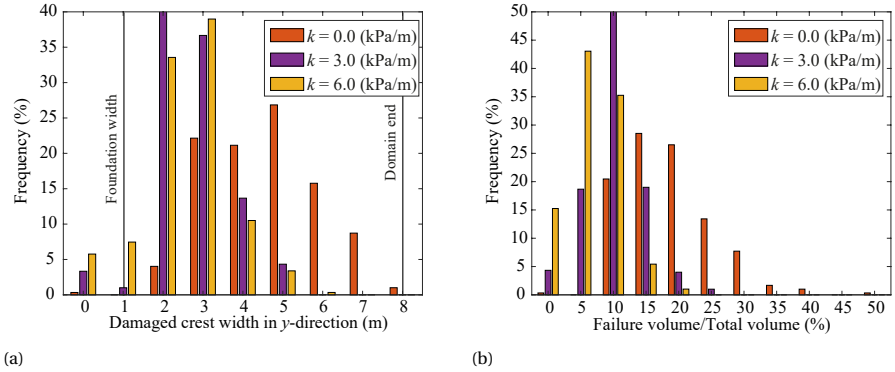

Figure 6.25: a) Damaged crest width and b) relative failure volume for Analysis set 4 with and without a depth trend in the mean undrained shear strength.

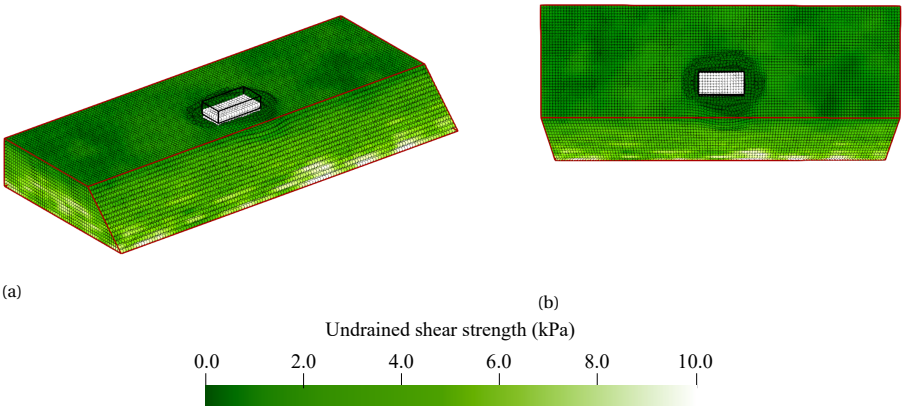

Figure 6.26: Final geometry of a foundation failure on a slope with a depth trend k = 6.0 kPa/m in the mean undrained shear strength.

Figure 6.25 confirms that slides with a depth trend are smaller on average, as the slides can occur through layers above the base and tend to spread less in the direction along the slope. While, in the analyses discussed previously, foundation failure only occurred at the same time as the slope failure, with a significant depth trend a foundation failure can sometimes occur even though the slope remains stable (see Figure 6.26). This can occur due to significantly weaker material at the crest of the slope. Figure 6.25 shows that the crest can remain almost intact with this failure mechanism, with the failure volume then tending to be small in comparison to volumes involved in a slope failure mechanism.

6.7. CONCLUSION

3D RMPM has been shown to be capable of producing an overview of many potential failure processes, and quantifying the failure consequences of these processes. It can provide insight into the effect of spatially varying shear strength properties on the failure onset and consequence.

The so-called 3D-effect increases the safety against the onset of failure and reduces the likelihood and size of secondary failures compared to 2D RMPM analyses. The number of inherent instabilities reduces from 20% to 10% for 2D and 3D, respectively. The loaded height on an inherently stable slope increases from a range of 0-0.6 m for 2D simulations to a range of 0.4 to 1.2 m for 3D simulations. In 2D, a relative failure volume of 30% to 100% has been observed, which decreases to a range of 10% to 35% for 3D. This indicates that 2D plane strain investigations of the failure process are conservative with respect to the probability of initial and retrogressive failure.

For the example problem considered, secondary failures on the sides of the original failure were more likely than retrogressive failure away from the crest. This failure pattern is beneficial for dykes with a large crest width, since lateral spreading of the failure will not (directly) trigger flooding. An increase in the degree of anisotropy increases the likelihood of retrogressive failures and tends to increase the width of the failures, while a smaller degree of anisotropy results in a more chaotic failure process where many small zones can become unstable. For isotropic spatial variability the results approximate to the deterministic outcome. The results for degrees of anisotropy larger than 5 are similar. A small depth trend increases the resistance against initial and retrogressive failure as the strength at the bottom of the slope increases. However, a larger depth trend causes a decrease of the ultimate foundation load and more retrogressive behaviour as failures at multiple depths become more likely. For a large depth trend, secondary failures become less likely; instead, weak material tends to flow into an expanding failure zone.

The chapter presents an initial investigation of 3-dimensional failure processes. Future investigations are required to improve the numerical accuracy of the simulations, mainly by increasing the number of material points, which would be possible once parallel computing is also used for individual realisations. The method can then be used to investigate other (more complex) slope geometries and 3D dyke failures.

REFERENCES

Chakraborty, A. K., & Goswami, D. (2021). Three-dimensional (3D) slope stability analysis using stability charts. *International Journal of Geotechnical Engineering, 15*, 642–649. https://doi.org/10.1080/19386362.2018.1465743

Hicks, M. A., & Li, Y. (2018). Influence of length effect on embankment slope reliability in 3D. *International Journal for Numerical and Analytical Methods in Geomechanics, 42*(7), 891–915. https://doi.org/10.1002/nag.2766

Lengkeek, H. J. (2022). *Testing and modeling of sheet pile reinforced dikes on organic soils - insights from the eemdijk full-scale failure test* (Doctoral dissertation). Technische Universiteit Delft, Delft.

Li, Y. J., Hicks, M. A., & Nuttall, J. D. (2015). Comparative analyses of slope reliability in 3D. *Engineering Geology, 196*, 12–23. https://doi.org/10.1016/j.enggeo.2015.06.012

Michalowski, R. L. (2010). Limit analysis and stability charts for 3D slope failures. *Journal of Geotechnical and Geoenvironmental Engineering, 136*, 583–593. https://doi.org/10.1061/(ASCE)GT.1943-5606.0000251

van den Eijnden, A. P., & Hicks, M. A. (2017). Efficient subset simulation for evaluating the modes of improbable slope failure. *Computers and Geotechnics, 88*, 267–280. https://doi.org/10.1016/j.compgeo.2017.03.010

Vanmarcke, E. H. (1980). Probabilistic stability analysis of earth slopes [Special Issue Mechanics of Landslides and Slope Stability]. *Engineering Geology, 16*(1), 29–50. https://doi.org/10.1016/0013-7952(80)90005-8

Vanmarcke, E. H. (1977). Reliability of earth slopes. *Journal of the Geotechnical Engineering Division, 103*(11), 1247–1265. https://doi.org/10.1061/AJGEB6.0000518

Varkey, D., Hicks, M. A., & Vardon, P. J. (2019). An improved semi-analytical method for 3D slope reliability assessments. *Computers and Geotechnics, 111*, 181–190. https://doi.org/10.1016/j.compgeo.2018.12.020

Varkey, D., Hicks, M. A., & Vardon, P. J. (2017). Influence of spatial variability of shear strength parameters on 3D slope reliability and comparison of analysis methods. *Geo-Risk 2017* (pp. 400–409). https://doi.org/10.1061/9780784480717.038

Zheng, X., Pisanò, F., Vardon, P. J., & Hicks, M. A. (2022). Fully implicit, stabilised mpm simulation of large-deformation problems in two-phase elastoplastic geomaterials. *Computers and Geotechnics, 147*, 104771. https://doi.org/10.1016/j.compgeo.2022.104771

7

CONCLUSIONS AND RECOMMENDATIONS

7.1. INTRODUCTION

The complexity of building and maintaining flood protection structures grows with the continuously increasing risk of flooding. To meet the stringent design criteria for these structures, engineers can take the remaining (i.e. residual) resistance of a dyke after initial slope failure into account. For this purpose, simplified guidelines for the remaining dyke resistance are used. These guidelines are over-conservative since they are based on a limited understanding of the failure process after slope instability. Recent studies suggest using standard, small deformation slope failure models, such as the Limit Equilibrium Method (LEM) or the Finite Element Method (FEM), to model the remaining dyke resistance. However, LEM and FEM cannot model large deformations during the failure process, and therefore require significant assumptions to reconstruct the remaining dyke geometry after the initial failure to assess the probability of secondary failures.

The Material Point Method (MPM) had been shown to successfully model large deformations and been used to model dyke slope failure. In this thesis, MPM was for the first time applied within a risk-based framework for dyke assessments to compute the probability of flooding. Additionally, the effect of spatial variability of soil properties on dyke slope failure processes was for the first time studied, although extensive research using the Random FEM (RFEM) has highlighted the importance of this variability on the initial slope failure. The work presented in this thesis further developed MPM for the assessment of probability of flooding, and accounted for the effect of spatial variability on dyke slope failure processes by using the Random MPM (RMPM), the natural extension of RFEM to MPM. This chapter summarises the main conclusions from the four main chapters of the thesis, and gives an overview of the recommendations for future research regarding (R)MPM and residual dyke resistance.

7.2. NEUMANN BOUNDARY CONDITIONS

To account for the load applied by the external water level on the outer dyke slope, the application of a hydrostatic boundary condition was investigated in Chapter 3. The application of boundary conditions is difficult in MPM, since the conditions must be compatible with the two discretisations used in MPM: i.e. the material points and the FEM background grid. It is especially difficult to apply boundary conditions at moving material boundaries. In dyke slope failure, movement of the external slope is expected and moving boundary conditions are therefore required. Chapter 3 studied the performance of five boundary condition methods in MPM and GIMP:

1. Equivalent point loads applied on surface material points.
2. Boundary moved to the surface nodes.
3. Boundary condition applied exactly.
4. Boundary condition moved proportionally to the volume of material points in the background grid elements (only in MPM).
5. Boundary condition applied on the support domains of GIMP.

Table 7.1: The performance of various boundary condition methods for different cases

Boundary condition method	MPM 1D	GIMP 1D	GIMP 2D	Submerged slope
1 Surface material points	–	–	–	– –
2 Surface nodes	–	– –	– –	N/A
3 Exact material surface	– –	++	+	+
4 Volume of MPs	++	N/A	N/A	N/A
5 Support domain	N/A	++	++	++

Key: – – unacceptable errors; – large errors; + minor errors; ++ exact

The performance of these methods is summarised in Table 7.1 for four test cases. The table indicates that the best performance is achieved by a boundary condition method compatible with the discretisation: i.e. a boundary condition based on the volume of material points in MPM or a boundary condition applied on the edge of the support domain in GIMP. Also, applying a boundary condition on the exact material surface performs well when using GIMP, since the material surface is usually close to the edge of the support domain.

For complex problems the location of the boundary is unknown. Therefore, two algorithms were proposed to construct the location of the boundary condition:

- The Proximity Field Method (PFM) can construct the segments of the exact material surface within each element based on the proximity to all material points.
- A contour algorithm for iso-rectangles can merge the edge of the support domains, and removes the overlap and small gaps between support domains. Where these gaps are not removed, they could lead to a boundary condition being incorrectly applied within the material after small movements of the material points.

The detected boundaries follow the deformations correctly and lead to comparable deformations and stresses. Applying the boundary conditions at the material points instead results in different deformations and stresses, and leads to a simulation crash when the material points originally located at the surface move into the material due to the deformations.

To summarise:

- In MPM, the correct boundary location can be far from the exact material location.
- In GIMP, the correct boundary location coincides with the support domains, which are usually close to the exact material surface.
- Applying loads at material points can lead to incorrect stresses in both MPM and GIMP. The errors grow significantly, potentially leading to a simulation crash, when the list of boundary material points is not updated during movement or a low number of material points per element is used.
- PFM can reconstruct the exact material boundary, while a contour algorithm for iso-rectangles can reconstruct the contour of the GIMP domains.

7.3. RISK FRAMEWORK FOR RESIDUAL DYKE RESISTANCE

RMPM is compatible with commonly used risk frameworks, and can be used to compute the probability of flooding by evaluating the probability of the dyke height (H) being lower than the external water level ($Z = H - h$). This limit state function Z is evaluated for separate water levels h, which can later be combined using fragility curves. The dyke slope failure processes can consist of many subsequent slope failures. Each slope failure may lead to flooding ($H < h$), a subsequent failure, or a stable situation. To compute the probability of flooding, the probability of all possible processes leading to flooding or a stable situation must be evaluated.

To reduce the complexity, previous research evaluated the sequence of most critical, i.e. most likely, failures, i.e. the failures with the highest probability of occurrence. However, this approach ignores the possibility that larger, apparently less critical failures, i.e. larger failures with a lower probability of failure, may lead to a higher probability of flooding. Therefore, RMPM assesses all possible failures processes using Monte Carlo simulation to compute the probability of flooding. In Chapters 5 and 6, RMPM is shown to be capable of evaluating the failure process without prior assumptions on the likelihood, shape and/or size of the individual failures.

7.4. DYKE SLOPE FAILURE PROCESSES

In Chapter 5 RMPM was applied to the slope failure of a simplified clay dike. The analyses show that including residual dyke resistance with RMPM can lead to a significant reduction in the probability of flooding compared to the probability of initial failure, a reduction of over 80% in some cases. To reduce computational costs, the analysed dyke had a high probability of initial failure. Therefore, the resistance of the dyke was unrealistically low, and the computed residual dyke resistance was likely to be conservative, as secondary failures in dykes with a higher (more realistic) mean strength would be less frequent.

The analyses of Chapter 5 indicate that spatial variability has a significant impact on the entire failure process, causing a large variety of failure processes, even for the simple dyke geometry considered. Initial failure did not occur in many simulations. Simulations with an initial failure could lead to a stable situation or flooding after one or more additional failures, and they could be classified as follows:

- Initial failure without secondary failures.
- Initial failure followed by (a) rotational secondary failure(s).
- Initial failure followed by a horizontal secondary failure.

These classes indicate that guidelines for remaining dyke resistance should consider the possibility of rotational and horizontal secondary failures.

A higher degree of anisotropy of the spatial variability increases the probability of initial failure, due to the increased possibility of semi-continuous weaker layers near the slope face. These semi-continuous weaker layers also promote the subsequent propagation of failure, thereby increasing the probability of flooding and reducing the remaining

dyke resistance. The reduction in the probability of flooding is lower than 25% for materials with layered spatial variability. Moreover, a higher degree of anisotropy increases the size of the overall failure, even in cases where flooding does not occur, i.e. the consequence of failure besides flooding is larger. With a lower degree of anisotropy, the residual dyke resistance increases significantly, leading to a reduction in the probability of flooding of 80% for materials with limited layering ($\theta_m \leq 2$ m).

Chapter 5 indicates that a smaller initial failure reduces the probability of flooding, as more remaining resistance is available. Further investigation can provide guidelines for computing the probability of flooding based on the likelihood, size and shape of the initial failure. Chapter 5 also shows that, due to retrogressive failure, flooding can still occur after very small failures, and modelling of the failure process is required to ensure the prevention of flooding. Hence, since flooding can occur even for large remaining geometries, guidelines using a "safe" remaining geometry (without modelling the failure process) seem unconservative.

The probability of flooding decreases with a lower water level, due to the larger dyke width at the lower water level which increases the remaining resistance. Since the probability of flooding significantly reduces with a lower water level, using fragility curves to assess the probability of flooding due to macro-instability can be beneficial compared to an assessment with a single design water level. Note that the external water level is not constant in a real storm, which is something that has not been accounted for in this work. Therefore, flooding may still occur if the water level rises after a slope failure at a lower water level.

To summarise:

- RMPM can lead to a significant reduction in the computed probability of flooding due to dyke slope failure.
- A higher degree of anisotropy increases the probability of initial failure and flooding due to the presence of large semi-continous weak zones, which reduces the remaining dyke resistance.
- A smaller initial failure reduces the probability of flooding.
- The water level has a significant effect on the probability of flooding. Designing a dyke based on a single design water level may be unconservative, especially when the remaining dyke resistance is being accounted for.

Chapter 6 shows the potential of 3D RMPM. It indicates that, while slope failures may be approximated by 2D models when deterministic analyses are performed, with the introduction of spatial variability slope failures become complex 3D processes even for simple problem geometries. Retrogressive failures can occur in multiple directions, increasing the likelihood of a secondary failure occurring. For a material with a mean undrained shear strength constant with depth, the retrogressive failures can be classified into three groups:

- Slope failure on the sides of the original failure triggered by the movement of the initial failure.

- A second failure behind the initial failure (in the direction perpendicular to the slope) centered at the same location along the slope as the initial failure. These failures have a similar size to the initial failure.

- A second failure behind the initial failure (in the direction perpendicular to the slope) not centered at the same location along the slope as the initial failure. These failures are smaller than the initial failure.

Of these three groups, slope failures on the sides of the initial failure are most frequent. This is due to the fact that, in the remaining geometry, the steep original slope face is less stable than the roughly circular face left behind by the slope failure. This slope face can become unstable by pulling forces due to the movement of the initial failure.

In 3D, inherent slope instabilities may occur at any location along the embankment slope. This so-called length effect increases the likelihood of initial failure, and thereby the probability of flooding, compared to the probability of a single 2D segment. Secondary failures generally occur close to the original location of the failure, and are unaffected by the length effect, i.e. the length effect only affects the probability of an initial failure. Chapter 6 shows that the increased resistance of a 3D failure compared to a 2D failure (the "3D-effect") can compensate for the length effect, thereby reducing the probability of an initial failure in 3D compared to 2D (for slopes of moderate length in the third dimension). Moreover, the 3D-effect also reduces the likelihood (and size) of secondary failures. Chapter 6 highlights that a 2D analysis (without correction of the 3D effects) is conservative compared to a 3D analysis, for both the initial failure as well as for the failure process.

A lower coefficient of variation of the soil shear strength, or a lower degree of anisotropy of the heterogeneity, reduces the variation of the stochastic response so that the solution moves towards the deterministic solution based on mean properties. This tends to increase the resistance against secondary failures, and the failure process may tend to consist of many small chaotic failures. A large degree of anisotropy, on the other hand, increases the likelihood and size of retrogressive failures. The failure process for a large degree of anisotropy is more structured, with large failures spreading both along and perpendicular to the slope.

A depth trend in the mean undrained shear strength tends to increase the resistance along the base of the slope, reducing the likelihood of deep failures along the base. However, it also decreases the resistance higher up the slope, thereby increasing the likelihood of shallower failures. For a small depth trend the total probability of deep and shallow failures decreases compared to a slope without a depth trend, whereas for a larger depth trend the total probability of failure increases with respect to a slope without a depth trend. The depth trend has the same effect on potential secondary failures, i.e. the likelihood decreases for a small depth trend, but increases for a larger depth trend. Moreover, for a larger depth trend, the retrogressive failure process changes: weak material constantly flows into the failure zone, gradually extending the failure zone in multiple directions.

To summarise:

- 3D RMPM provides insight into the wide range of 3D slope failure processes.

- The "3D-effect" increases the resistance against initial and retrogressive failures. 2D simulations of dyke failure processes are therefore conservative in comparison to 3D simulations.
- Secondary failures on the sides of the initial failure are more likely than retrogressive failures perpendicular to the slope face.
- A larger degree of anisotropy increases the probability of secondary failures.
- A small or large depth trend may increase or decrease the slope resistance, respectively. A depth trend can change the failure process from discrete failure blocks to a flow-like failure.

7.5. RECOMMENDATIONS FOR FUTURE RESEARCH

The work presented in this thesis contains certain limitations. Recommendation to negate these in future research are as follows:

- Find consistent boundary conditions for non-Neumann boundary conditions and other MPM (stress) improvement techniques. Accurate boundary conditions are vital for the general applicability of MPM in user-practice.
- Random MPM is computationally too intensive for general practice. To reduce computational costs, probabilistic tools such as subset simulation (van den Eijnden and Hicks, 2017) could be combined with RMPM, so that investigations at lower (more realistic) probabilities of initial failure can be considered.
- The size of the domain and the number of material points have been limited in this work. To investigate more complex (3D) geometries and improve the numerical accuracy, reducing the computational cost of MPM is vital. Parallel computations have in this work been used to simultaneously evaluate multiple Monte Carlo realisations. For complex problems, the individual realisations should also be executed in parallel.
- Double-mapping with GIMP shape functions (DM-G) has been used in this thesis to reduce the effect of cell crossing errors and incorrect positions of the integration points. Further research is required to validate this technique, and to highlight its numerical accuracy and convergence when modelling large scale deformations.
- The computational cost may be reduced by combining RMPM with RFEM such that only those realisations with an initial failure are analysed using RMPM.
- Combining MPM and/or FEM with LEM can make both methods more appropriate for industrial use. The fast, and industry standard, LEM can be used to compute the probability of initial failure. FEM and/or MPM can then be used to compute the deformations of slope failure. For example, MPM can be used to construct the remaining geometry after initial failure, which may then be evaluated with LEM (Voorn, 2021).

- Apply RMPM on various dyke geometries to provide conservative estimates of the probability of flooding given the size of the initial failure or the shape and size of the residual dyke geometry. These estimates should consider the effect of spatial variability, since both the initial and secondary failures will be drawn to (potentially the same) weak zones. The guidelines should consider both rotational and horizontal secondary failures. Guidelines for the reconstruction of the remaining dyke geometry after initial failure could also be developed.

- Extend RMPM (and RFEM) to more complex constitutive models to extend the applicability to (inter)national dyke assessments. The work in this thesis focused on clay dikes founded on a stiff bed. It is to be expected that slope failure processes for other dyke geometries, for example a sand dyke covered with a clay layer on soft foundation layers, are significantly different. Other constitutive models are required to extend RMPM to these soil types.

- An investigation into the constitutive model used in (Dutch) dyke assessments is required. The assessments use a so-called 'critical state' strength model to assess the initial failure. This strength tends to be lower than the peak strength, which in this work is used as the initial undrained shear strength, and therefore tends to be closer to the residual undrained shear strength. However, the residual undrained shear strength, i.e. the strength after large deformations, may be lower than the critical state strength. Further investigations are required to understand the material behaviour after large deformations.

- Use (R)MPM to model centrifuge and/or large scale dyke failure tests to confirm our understanding of dyke failure processes. Centrifuge tests can also be used to investigate which properties affect the shape of the remaining profile.

- This work has used a constant external water level, and assumed a fully saturated dyke. To study the effect of (excess) pore-pressures in the failure zone on the failure process, a phreatic surface dependent on the external water level should be used. Moreover, RMPM should be extended from a total stress analysis to an effective stress (two-phase) analysis MPM (e.g. Zheng et al., 2022). The effect of the duration of a storm on the probability of flooding may then also be studied.

- MPM may be combined with erosion models to account for other secondary failure mechanisms after macro-instability, such as wave overtopping or internal erosion (van Bergeijk et al., 2021). It may also be used for investigating the interaction between primary failure mechanisms.

- To improve the applicability of the results of RFEM and/or RMPM, standardised techniques to evaluate and present random slope failure (processes) are required. Analysing and describing the results of RFEM and/or RMPM is a time consuming process, and RFEM/RMPM are therefore not often applicable for user practice. Histograms of the failure load and failure size can give insight into the failure process, but it is difficult to grasp all possibilities based on histograms which only address one variable. Analysing a subset of realisations, by for example plotting the deformations in a realisation, helps to fully understand the failure process in

these realisations, but it can be difficult to extrapolate this information to the complete set of realisations. High-order data processing techniques may be a good candidate for better and faster quantification and/or classification of slope failure processes.

REFERENCES

van den Eijnden, A. P., & Hicks, M. A. (2017). Efficient subset simulation for evaluating the modes of improbable slope failure. *Computers and Geotechnics*, *88*, 267–280. https://doi.org/10.1016/j.compgeo.2017.03.010

van Bergeijk, V. M., Verdonk, V. A., Warmink, J. J., & Hulscher, S. J. M. H. (2021). The cross-dike failure probability by wave overtopping over grass-covered and damaged dikes. *Water*, *13*(5), 690. https://doi.org/10.3390/w13050690

Voorn, P. H. E. (2021). *Connecting deterministic and numerical methods to better estimate the probability of flooding for clay dikes* (Master's thesis). Delft University of Technology.

Zheng, X., Pisanò, F., Vardon, P. J., & Hicks, M. A. (2022). Fully implicit, stabilised mpm simulation of large-deformation problems in two-phase elastoplastic geomaterials. *Computers and Geotechnics*, *147*, 104771. https://doi.org/10.1016/j.compgeo.2022.104771

CURRICULUM VITÆ

Guido REMMERSWAAL

13 September 1992	Born in Pijnacker, The Netherlands.

EDUCATION

2014-2017	MSc. Civil Engineering Specialization: Geo-Engineering Delft University of Technology *Thesis: Development and implementation of moving boundary conditions in the material point method.*
2011–2014	BSc. Civil Engineering Delft University of Technology
2005–2009	Pre-university secondary education (VWO) Christelijk Lyceum Delft, Delft, The Netherlands

EMPLOYMENT

2021–Present	Jr. Advisor/Researcher Energy and Underground Infrastructure Deltares, Delft, The Netherlands
2017–Present	PhD researcher Geo-Engineering Delft University of Technology

LIST OF PUBLICATIONS

PEER-REVIEWED JOURNAL PAPERS

1. **Remmerswaal, G.**, Vardon, P. J., & Hicks, M. A. (2023). Inhomogeneous Neumann boundary conditions for MPM and GIMP (submitted for journal publication)

2. Pol. J. C., Kindermann, P. van der Krogt, M. G., van Bergeijk, V. M., **Remmerswaal, G.**, Kanning, W., Jonkman, S. N., & Kok, M. (2022). The effect of interactions between failure mechanisms on the reliability of flood defenses. *Reliability Engineering & System Safety, 231*, 108987 https://doi.org/10.1016/j.ress.2022.108987.

3. **Remmerswaal, G.**, Vardon, P. J., & Hicks, M. A. (2021). Evaluating residual dyke resistance using the Random Material Point Method. *Computers and Geotechnics, 133*, 104034. https://doi.org/10.1016/j.compgeo.2021.104034.

4. González Acosta, J. L., Vardon, P. J., **Remmerswaal, G.**, & Hicks, M. A. (2020). An investigation of stress inaccuracies and proposed solution in the material point method. *Computational Mechanics, 65*, 555–581. https://doi.org/10.1007/s00466-019-01783-3

CONFERENCE CONTRIBUTIONS

1. **Remmerswaal, G.** & Martinelli, M. (2023). Evaluation of a Gauss integration scheme in MPM for strain dependent soils. In L. Zdravkovic, S. Kontoe, D. M. G. Taborda & A. Tsiampousi (Eds.), *Proceedings of the 10th European Conference on Numerical Methods in Geotechnical Engineering (NUMGE 2023)*, 26-28 June 2023, London, United Kingdom https://doi.org/10.53243/NUMGE2023-151

2. Zheng, X., González Acosta, J. L., **Remmerswaal, G.**, Vardon, P. J., Pisanò, F., & Hicks, M. A. (2021). Development of a Robust Coupled Material Point Method. In M. Barla, A. Di Donna, & D. Sterpi (Eds.), *Challenges and Innovations in Geomechanics - Proceedings of the 16th International Conference of IACMAG - Volume 1* (pp. 819-826). Springer Science+Business Media. https://doi.org/10.1007/978-3-030-64514-4_88

3. **Remmerswaal, G.**, Vardon, P. J., & Hicks, M. A. (2019). Influence of Residual Dyke Strength on Dyke Reliability Using the Random Material Point Method. In J. Ching, D. Li, & J. Zhang (Eds.), *Proceedings of the 7th International Symposium on Geotechnical Safety and Risk (ISGSR 2019)* (pp. 775-780), 11-13 December 2019, Taipei, Taiwan

4. **Remmerswaal, G.**, Bolognin, M., Vardon, P. J., Hicks, M. A. & Rohe, A.(2019). Implementation of non-trivial boundary conditions in MPM for geotechnical applications. In *Proceedings of the Second International Conference on the Material Point Method for Modelling Soil–Water–Structure Interaction (MPM2019)*, 8-10 January 2019, Cambridge, United Kingdom

5. **Remmerswaal, G.**, Vardon, P. J., & Hicks, M. A. (2018). Ultimate limit state assessment of dyke reliability using the random material point method. *Abstract from the 4th International Symposium on Computational Geomechanics (ComGeoIV)*, 2-4 May 2018, Assisi, Italy.